Nevada System of Higher Education

1865

TECHNICAL REPORT

Precarious Rock Methodology for Seismic Hazard: Physical Testing, Numerical Modeling and Coherence Studies

Report Document Identifier:
TR-06-003

Task ORD-FY04-020

REVISION: 0

Authors: Rasool Anooshehpoor

Matthew D. Purvance

for James N. Brune

Leiph A. Preston

John G. Anderson — John G. Anderson

Kenneth D. Smith

PI: for James N. Brune — 9/15/2006
date

QA Manager: Amy Smiecinski — ASmiecinski — 9-21-06
date

1.0 Table of Contents

1.1 Summary

This report covers the following projects: Shake table tests of precarious rock methodology, field tests of precarious rocks at Yucca Mountain and comparison of the results with PSHA predictions, study of the coherence of the wave field in the ESF, and a limited survey of precarious rocks south of the proposed repository footprint.

A series of shake table experiments have been carried out at the University of Nevada, Reno Large Scale Structures Laboratory. The bulk of the experiments involved scaling acceleration time histories (uniaxial forcing) from 0.1g to the point where the objects on the shake table overturned a specified number of times. The results of these experiments have been compared with numerical overturning predictions. Numerical predictions for toppling of large objects with simple contact conditions (*e.g.*, I-beams with sharp basal edges) agree well with shake-table results. The numerical model slightly underpredicts the overturning of small rectangular blocks. It overpredicts the overturning PGA for asymmetric granite boulders with complex basal contact conditions. In general the results confirm the approximate predictions of previous studies.

Field testing of several rocks at Yucca Mountain has approximately confirmed the preliminary results from previous studies, suggesting that the PSHA predictions are too high, possibly because the uncertainty in the mean of the attenuation relations.

Study of the coherence of wavefields in the ESF has provided results which will be very important in design of the canisters distribution, in particular a preliminary estimate of the wavelengths at which the wavefields become incoherent. No evidence was found for extreme focusing by lens-like inhomogeneities.

A limited survey for precarious rocks confirmed that they extend south of the repository, and one of these has been field tested.

1.2 Acronyms

ESF	Exploratory Studies Facility
FL	Fluffy (rock nickname)
LBNL	Lawrence Berkeley National Laboratory
NSHE	Nevada System of Higher Education
NTS	Nevada Test Site
PBR	Precariously Balanced Rock
PGA	Peak Ground Acceleration
PGV	Peak Ground Velocity
PSHA	Probabilistic Seismic Hazard Analyses
RE	Red Eye (rock nickname)
TR	Tripod (rock nickname)
UCCSN	University and Community College System of Nevada
WLW	Walks a Long Way (rock nickname)

1.3 Acknowledgment

Funding for this project was provided by the U. S. Department of Energy through a cooperative agreement with the University and Community College System of Nevada (DE-FC28-04RW12232). The authors thank David Von Seggern for the technical review of the scientific notebook and the report. We are grateful to the Quality Assurance Group, Amy Smiecinski, Terry Muller, Raymond Keeler, Barbara Roosa, Julie Bertoia, Barbara Roosa, Aishia Henderson, and Morrie Roosa for the QA reviews, and for their helpful advice on QA issues. We also thank Patrick Laplace, Paul Lucas, and Ian Buckle at the UNR Civil Engineering Department for facilitating use of the shake table. Finally, we would like to thank Dan Neubauer and Mike Taylor of Bechtel/Sandia for providing logistics and safety guidance during field work.

1.4 List of Tables

Table 1: The physical characteristics of a subset of the objects used in shake-table experiments are listed here. Figure 2-a show most of these object on the shake table, before an experiment (DID 020RA.001, table-1).

Table 2: Locations of the precarious rocks on Yucca Mountain crest and Solitario Canyon tested in this study. These points are chosen for seismic hazard analyses (DID 020RA.001, table-1).

Table 3: The approximate dates for each layout and phase. This table is non-Q and included or information only (UCCSN- UNR-085-v1).

Table 4: Seismicity rates (earthquakes per 100,000 years) for the sources illustrated on Fig. 21. This table is non-Q and included or information only (DID 020RA.004, table-4).

Table 5: Relationship of the ten models to the median model. This table is non-Q and included or information only (DID 020RA.004, table-5).

Table 6: Reweighted models to test an asymmetrical distribution weighted towards smaller values. This table is non-Q and included or information only (DID 020RA.004, table-6).

1.5 List of Figures

Figure 1: An asymmetric rock with weight W resting on a pedestal is free to rotate about rocking axes through rocking points RP_1 and RP_2. R_1 and R_2 measure the distances from the center of mass to RP_1 and RP_2, respectively. α_1 and α_2 are the angles between the vertical and R_1 and R_2, respectively.

Figure 2: Test objects on a shake table are shown before (a) and after (b) an experiment. Notice that the objects are either resting on grip tape or a roughened concrete slab to inhibit sliding. The objects were shaken by the scaled N51E component of the 2002 Denali earthquake recorded at PS10 with PGA ~ 0.3g. Objects AL2, W2, IB1, IB2, IB4, and L overturned. The shake table motions were recorded on a Kinemetrics K2 accelerometer, located behind object K.

Figure 3: Comparison of input (blue) (source: Cosmos Virtual Data Center website http://db.cosmos-eq.org) and measured (red) accelerograms corresponding to the N51E component of the 2002 Denali earthquake recorded at pump station 10. The input seismogram has been scaled with PGA ~ 0.41g. This example demonstrates the level of agreement between the input and measured accelerograms. In our analyses only the measured accelerograms on the shake table are used. In this plot the blue curve is non-Q and included for corroboration only (DID 020RA.003, fig-3).

Figure 4: Dynamic toppling accelerations (shake-table experiment) versus quasi-static toppling accelerations for the objects listed in Table 1 are plotted here. These objects were subjected to acceleration time histories with the waveforms similar to 10 different earthquakes and synthetic seismograms. We have used two different symbols to distinguish between seismograms for which PGV/PGA values are above or below the *arbitrary* threshold of 0.15. High-frequency seismograms have generally lower PGV/PGA values than low-frequency seismograms. As this plot suggests, there is a lot more scatter in the dynamic toppling acceleration (blue open circles) when high-frequency seismograms were used in the experiment (DID 020RA.001, fig-4).

Figure 5: Histogram of probabilities corresponding to the first overturning occurrence from the numerical experiment. The modal value (*e.g.*, 16% overturning probability (red line)) is used for comparative purposes. This plot is non-Q and included for corroboration only (DID 020RA.003, fig-5).

Figure 6: Comparison of shake-table data (black symbols, wood; red symbols, aluminum) and the numerical predictions [9] (black lines) along with the 95% prediction intervals (blue curves) for blocks AL1 and W1 (left) and AL1 and W1 (right). Pictures of the objects are inset for reference. In these plots the curves are non-Q and included for corroboration only (DID 020RA.003, fig-6).

Figure 7: Shake table data (red symbols) (Source DTN: 020RA.001) are compared with the formulation of Purvance [9] (black lines) along with the 95% prediction intervals (blue lines) for rectangular blocks AL1, AL2, G, W1, W2 and W3. Blocks W1, W2 and W3 are the exact replicas of AL1, AL2, and G, respectively. In these plots the curves are non-Q and included for corroboration only (DID 020RA.003, fig-7).

Figure 8: Shake table data (red symbols) (Source DTN: 020RA.001) and the formulation of Purvance [9] (black lines) along with the 95% prediction intervals (blue lines) for I-beams IB0, IB1, IB2, and IB4. IB0 and IB4 have identical α and R, but different moment of inertia about the rocking points. IB1 is asymmetric. In these plots the curves are non-Q and included for corroboration only (DID 020RA.003, fig-8).

Figure 9: Shake table data (black symbols) (Source DTN: 020RA.001) and the formulation of Purvance [9] (black lines) along with the 95% prediction intervals (blue lines) for boulders L, K, and E. Pictures of the objects are inset for reference. In these plots the curves are non-Q and included for corroboration only (DID 020RA.003, fig-9).

Figure 10: **(**a) Simple rocking model assumed in the numerical formulation of Purvance [9]. (b) Schematic of the restoring force versus angle of inclination.

Figure 11: (a) Complex rocking model with multiple rocking points. (b) Schematic of the restoring force versus angle of inclination. The arctangent of the peak normalized force is utilized subsequently.

Figure 12: Tilt test of one of the stone boulders shaken experimentally.

Figure 13: Force versus inclination measurements for boulders L, K, and E. The percentages on these figures represent the percent reduction in peak normalized force compared to a rock with a perfectly sharp edge (DID 020RA.001, fig-13).

Figure 14: Refined overturning predictions based on force versus inclinations measurements and the formulation of Purvance [9] for the boulders L, K, and E. The red dots are from shake-table experiments. The green curves, identical to the black curves in Fig. 9, are plotted for comparison when the basal roughness is not taken into account. In these plots the curves are non-Q and included for corroboration only (DID 020RA.003, fig-14).

Figure 15: Photographs of the five precarious rocks in the Yucca Mountain Area selected for field test. Rocks **a** and **b** are on or near the Yucca Mountain crest. Rocks **c**, **d**, and **e** are on the west side of Yucca Mountain, in Solitario Canyon.

Figure 16: Locations of the five rocks shown in Fig. 15 are marked on the map.

Figure 17: Example vertical component seismograms to show variation along the array. This event occurred on October 18, 2005 at 7:31 AM at 34.0297° lat., -116.6751° lon. and 10 km depth (M_L 4.4, distance 310 km). Geophones are ordered from south (top of each panel) to north (bottom) at 100 m spacing. a) raw (unfiltered), b) band-passed 0.5—1.0 Hz, c) 1—2 Hz, d) 2—4 Hz, e) 4—8 Hz. These plots are non-Q and included for corroboration only (DID 020RA.002, fig-17).

Figure 18: Coherency results as a function of inter-station distance and frequency. The top row is from the 100 m spacing, vertical phase of the study; the middle row is from the 100 m, horizontals; the bottom row from the 60 m, verticals. Left column is for P-wave; right is for S-waves. White areas represent areas with no data. These plots are non-Q and included for corroboration only (DID 020RA.002, fig-18).

Figure 19: Cross-correlation results. The top row is from the 100 m spacing, vertical phase of the study; the middle row is from the 100 m, horizontals; the bottom row from the 60 m, verticals. Left column shows results for all the data in that phase for each receiver pair; right, is the same except divided into four azimuthal bins. These plots are non-Q and included for corroboration only (DID 020RA.002, fig-19).

Figure 20: Annual probability of exceedance of the mean horizontal peak acceleration calculated from YM PSHA. This figure does not appear in the Stepp *et al* article [10], which was truncated at a higher probability. The probabilistic seismic hazard analysis used numerous “expert opinions” about the input, and calculated hazard curves for each. Ground motions exceeded by various percentiles of the resulting hazard curves are tabulated here. The mean gets higher than the 85th percentile because the mean is taken as the average of annual probability rather than the average of the log of the annual probability. This plot is non-Q and included for corroboration only (Source Accession Number: MOL.19980619.0640).

Figure 21: Equivalent of Fig. 20, except for the mean of the horizontal peak ground velocity. This plot is non-Q and included for corroboration only (Source Accession Number: MOL.19980619.0640).

Figure 22: (top) Regional map showing the source model used for these calculations, and (bottom) detailed map showing the source model used for these calculations in the vicinity of the precarious rocks and the PSHA site.

Figure 23: Plot showing values of ε_μ and ε_σ for approximating the effect of the epistemic uncertainty. This plot is non-Q and included for corroboration only (DID 020RA.004, fig-23).

Figure 24: Combination of several hazard curves for peak acceleration. The lightest lines are hazard curves for the ten combinations of ε_μ and ε_σ. The colors of these lines match the marker colors in Fig. 23. The mean curve is the weighted mean of these ten curves, with weights given in Table 5; note that the mean is determined from the occurrence rates, and not the log of the occurrence rates, thus explaining why the mean deviates towards the highest curves. The median curve is the curve computed for $\varepsilon_\mu = 0$ and $\varepsilon_\sigma = 0$. The

YMP median, mean, 5%, and 95% curves are from Fig. 20. This plot is non-Q and included for corroboration only (DID 020RA.004, fig-24).

Figure 25: Equivalent of Fig. 24 for peak velocity. This plot is non-Q and included for corroboration only (DID 020RA.004, fig-25).

Figure 26: Comparison of selected hazard curves for peak acceleration at four sites. The curves are for the four cases, from largest to smallest occurrence rates: case c (defined in Table 5), the median model for the Anderson ground motion prediction equations, a model with $\sigma_A = 0.01$ instead of the value given in the ground-motion model, and case f (defined in Table 5). This plot is non-Q and included for corroboration only (DID 020RA.004, fig-26).

Figure 27: Comparison of selected hazard curves for peak velocity at four sites. See caption for Fig. 26 for description of the hazard curves. This plot is non-Q and included for corroboration only (DID 020RA.004, fig-27).

Figure 28: Peak acceleration results using $\sigma_A = 0.01$ compared with the YMP median and range of values and compared with the median curve for the JGA model. This plot is non-Q and included for corroboration only (DID 020RA.004, fig-28).

Figure 29: Equivalent of Fig. 28 for peak velocity. This plot is non-Q and included for corroboration only (DID 020RA.004, fig-29).

Figure 30: Equivalent to Fig. 28, but now also showing the effects of truncation of the distribution of ground motions at selected multiples of σ_A above the median value on the estimated mean exceedance rate of the peak acceleration. This plot is non-Q and included for corroboration only (DID 020RA.004, fig-30).

Figure 31: Equivalent to Fig. 29, but now also showing the effects of truncation of the distribution of ground motions at selected multiples of σ_A above the median value on the estimated mean exceedance rate of the peak acceleration. This plot is non-Q and included for corroboration only (DID 020RA.004, fig-31).

Figure 32: Examination of the impact of truncation of the distribution of ground motions at selected multiples of σ_A above the median value on the mean exceedance rate of peak acceleration. The mean curve is estimated by taking the mean of the ten hazard curves defined in Table 5. The case with no truncation is the same as the mean shown in Fig. 24. This plot is non-Q and included for corroboration only (DID 020RA.004, fig-32).

Figure 33: Examination of the impact of truncation of the distribution of ground motions at selected multiples of σ_A above the median value on the mean exceedance rate of peak velocity. The mean curve is estimated by taking the mean of the ten hazard curves defined in Table 5. The case with no truncation is the same as the mean shown in Fig. 25. This plot is non-Q and included for corroboration only (DID 020RA.004, fig-33).

Figure 34: Overturning probability of the precarious rocks Fluffy (FL), Red Eye (RE), Walks a Long Way (WLW), and Tripod (TR) exposed to the median ground motion model (*e.g.*, ε_μ and $\varepsilon_\sigma = 0$). The error bars correspond to the 5% and 95% prediction intervals on the overturning probability. These rocks are not consistent with the median ground motion model (*e.g.*, ε_μ and $\varepsilon_\sigma = 0$) as discussed in the text. This plot is non-Q and included for corroboration only (DID 020RA.004, fig-34).

Figure 35: Combined survival probability of the ensemble of 4 precarious rocks (*e.g.*, probability that all 4 rocks simultaneously survive the ground motion model) along with

the combined survival probabilities corresponding to the 5% and 95% prediction intervals of the overturning model. The identifier M corresponds to the median ground motion model (ε_μ and $\varepsilon_\sigma = 0$) and the identifiers a - j correspond to the cases ($\varepsilon_\mu, \varepsilon_\sigma$) equal to (0.7,0), (0.7,1.7), (2.3,1.0), (2.3,-1.0), (0.7,-1.7), (-0.7,-1.7), (-2.3,-1.0), (-2.3,1.0), (-0.7,1.7), and (-0.7,1.0), respectively. This plot is non-Q and included for corroboration only (DID 020RA.004, fig-35).

Figure 36: Peak acceleration, for the case where only non-positive values of ε_μ are considered, as discussed in the text. This plot is non-Q and included for corroboration only (DID 020RA.004, fig-36).

Figure 37: Peak velocity, equivalent of Fig. 36. This plot is non-Q and included for corroboration only (DID 020RA.004, fig-37).

2.0 Purpose

To determine the importance of the following projects relative to seismic hazard at Yucca Mountain: Shake table tests of precarious rock methodology, field tests of precarious rocks at Yucca Mountain and comparison of the results with PSHA predictions, study of the coherence of the wave field in the ESF, and a limited survey of precarious rocks south of the proposed repository footprint.

3.0 Quality Assurance

This report is written in accordance with the NSHE Quality Assurance Program. In addition to the report, the work was conducted in with the NSHE Quality Assurance Program. No final conclusions of this report are based on unqualified data.

4.0 Introduction

Seismic hazards are being carefully investigated at Yucca Mountain, Nevada, the designated national high-level radioactive-waste repository. As a result of the discovery of numerous precariously balanced rocks (PBR) in the vicinity of Yucca Mountain, a methodology was developed to use these rocks as constraints on the probable ground motion to be expected at the designated repository. The precarious rock methodology gives a direct indication of the upper bound on the amplitude of the last significant ground shaking at a site, in contrast to the indirect inference provided by trenching studies, which cannot specify any characteristics of ground motions caused by discrete fault slip.

In many types of terrain in California and Nevada, groups of precariously balanced rocks have evolved naturally through weathering of a buried rock mass into corestones followed by erosion of the overlying surface materials, resulting in stacks of corestones above the soil horizon. Bierman *et al.* [1] indicate that the erosion rates of boulders in similar climates, once exhumed, may be quite slow, suggesting that the precarious rock shapes have not changed significantly over the past 10,000 years. The common presence of rock varnish on such rocks indicates that they have been in their current unstable positions for thousands of years. Therefore, groups of precariously balanced rocks can be used as low-resolution strong-motion seismoscopes that have been operating on solid rock outcrops for thousands of years. As such, they provide important information about seismic risk. We have established the mechanical basis for estimating the horizontal ground motions necessary to overturn PBRs through combined field, laboratory, and numerical modeling initiatives. The distribution of precarious rocks relative to known active faults and intensity zones produced by historical earthquakes confirms their usefulness in outlining areas that have or have not undergone recent strong ground shaking.

A goal of the first stage of Yucca Mountain precarious rock studies [2] was to develop a methodology whereby precariously balanced rocks could be used to estimate both the minimum ground motions necessary to result in overturning and the frequency of such ground motions. The development of the precarious rock methodology has involved three tasks: (1) documentation of the distribution of precarious rocks, both locally in the vicinity of Yucca Mountain and regionally in California and other parts of Nevada, (2) development of computer models, physical models, and field tests to quantitatively estimate the ground motions required to overturn rocks, and (3) development of surface age-dating techniques to estimate the times various precariously balanced rocks have been in their current positions. However, age dating was not carried out because no qualified supplier was available.

The relatively large horizontal ground motions predicted by the recently completed Probabilistic Seismic Hazard Analysis (PSHA) [4] are not consistent with the preliminary results from the precarious rock survey conducted by Brune and Whitney [5], nor the results described in the Technical Report TR-02-001 [2]. The importance of the precarious rock approach is that it gives a direct indication of maximum levels of ground shaking that a given location has experienced over time periods of thousands to tens of thousands of years. This is in sharp contrast to the indirect inferences based on very limited temporal earthquake data drawn from the current PSHA methodology.

Another important issue in predicting hazard at Yucca Mountain is the variability of ground motions within the repository block from earthquake sources. This affects engineering design and models for the uncertainty and coherence of ground motion in the Exploratory Studies Facility (ESF), as well as, by extrapolation, the interpretation of the distribution of precarious rocks at the surface. It is conceivable that heterogeneities beneath the repository might cause focusing and/or de-focusing of energy at certain points in the repository or at the surface. Thus another part of this task was to carry out a pilot study to investigate the coherence of earthquake motions at select sites in the ESF at Yucca Mountain. The pilot study includes recording waveforms and evaluating the signal-to-noise characteristics, recoverable bandwidth, and coherence using existing geophones that were installed in the ESF for controlled source experiment by Lawrence Berkeley National Laboratory (LBNL). We recorded many earthquakes, with associated noise, for both vertical and horizontal motion and different instrument spacing to develop predictive models for ground motions (coherence as a function of spatial wavenumber and frequency).

Field testing of several rocks at Yucca Mountain has approximately confirmed the preliminary results from previous studies [5], suggesting that the PSHA predictions are too high, possibly because of the uncertainty in the mean of the attenuation relations.

In this task we have further quantified the constraints on ground motion provided by the precarious rock methodology and compared the results with the PSHA predictions. This involved the following sub-tasks:

1. Survey for new locations of precarious rocks in the vicinity of Yucca Mountain, especially south of the repository footprint.
2. Rigorous field tests on precarious rocks to obtain parameters necessary for numerical modeling.
3. Carrying out shake-table experiments on rigid objects of various sizes and aspect ratios using a suite of synthetic and earthquake seismograms.
4. Carrying out a large number of numerical rocking tests on located rocks using a suite of input seismograms to provide useful probabilistic constraints on ground motions.
5. Comparison of overturning predictions with ground motion predictions of the existing PSHA study.
6. Sensitivity studies of PSHA to: (1) the "ergodic" assumption, and (2) to truncating attenuations relations at various multiples of one standard deviation.
7. Installation of portable instrumentation and short-length geophone cables to acquire data from sets of high-frequency geophones in the ESF and assessment of instrument response to earthquake ground motions.

5.0 Methods and Materials

5.1 Implementing Procedures

- IPR007: Methodology to Determine the Quasi-Static Toppling Acceleration of Precarious Rocks in the Field
- IPR009: Methodology to Determine the Dynamic Toppling Acceleration of Precarious Rocks Using Shake Table

5.2 Surveys for Precarious Rocks

It was suggested (J. Savino, personal communication) that there might be interest in the possibility of extending the repository south of the current footprint, and that consequently it might be important to know if there were precariously balanced rocks there. Therefore three reconnaissance field surveys were undertaken. It was verified that a number of precariously balanced rocks exist south of the current proposed repository footprint. At some future date these could be studied and tested if there is sufficient interest. Only one of these has been field tested to date (YMSESept02) and will discuss later.

5.3 Quantification of Precarious Rock Constraints on Ground Motion

Most precariously balanced rocks surveyed in the field would rock about two rotational axes when disturbed by strong ground motions during earthquakes. Fig. 1 illustrates a schematic of a balanced rock that is free to oscillate about rocking points RP_1 and RP_2. It is assumed that the rock geometry does not vary in the 3rd dimension normal to the page. The parameters α_i and R_i (the most important parameters in rocking response) are estimated either in the field or by visual inspection of photographs (IPR-007).

The precarious rock methodology [6, 7] utilizes the 2-dimensional rocking response of slender blocks subjected to given base motions to estimate minimum peak ground accelerations (PGA) that could topple a specific rock. To validate the technique, Anooshehpoor and Brune [8] used shake-table tests (IPR-009) to investigate the dynamic rocking response of wooden rectangular blocks of various sizes and aspect ratios exposed to realistic seismograms and compared the results with those of numerical tests (IPR-008). For input motions they used the waveforms of three seismograms: (1) the N-S component of the 17 August 1999 Turkey earthquake, recorded at Izmit, (2) a horizontal component of an M7.9 synthetic earthquake on the Mojave section of the San Andreas fault at a distance of 15 km, and (3) the Chancellor nuclear explosion at the Nevada Test Site scaled to an equivalent 1000 kt at 10 km. However, the small number of seismograms used in these tests was not sufficient to warrant meaningful statistical analyses. Furthermore Purvance [9] found that the overturning probability of a block with specified geometry is not only related to the high-frequency ground motion amplitude (PGA) but also the lower-frequency ground-motion amplitude via numerical simulations. In order to investigate these relationships and enhance our ability to validate such models, we carried out new shake-table experiments using 10 real and synthetic seismograms.

5.3.1 SHAKE-TABLE EXPERIMENTS

A series of new shake-table experiments (Fig. 2) have been carried out at the University of Nevada, Reno Large Scale Structures Laboratory, to study the overturning behavior of symmetric and asymmetric rigid objects with various sizes and aspect ratios. The bulk of the experiments involved scaling acceleration time histories (uniaxial forcing) from 0.1g to the point where all of the objects on the shake table overturned 3 times. More than two dozen objects have been utilized ranging in height from about 20 to 120 cm and height to width ratios from about 2 to 10. The physical characteristics of a subset of the objects studied are listed in Table 1. They consist of six rectangular blocks, four I-beams and three granite rocks. Small wooden blocks W1, W2 and W3 have the exact dimensions of the aluminum blocks AL1, AL2, and the granite block G, respectively. IB0 is a four-foot tall steel I-beam. IB1 is similar to IB0 with a 100 lb weight attached to the top on one side, making it asymmetric. IB2 and IB4 are also similar to IB0 with added weights to change the geometrical attributes. L, E and K are boulders, similar to actual PBRs. The acceleration time histories utilized include strong motion recordings of 1979 Imperial Valley, 1985 Michoacan, 1999 Izmit, 1999 Chi-Chi, and 2002 Denali earthquakes and synthetic acceleration time histories (full sine pulse and random vibration records). The results of these experiments have been compared with numerical overturning predictions of Purvance [9].

In the precarious rock methodology it is assumed that the rocks experience rocking motion without sliding during earthquakes. Therefore, in order to inhibit sliding, smaller objects were placed on grip tape and larger ones on a 3-inch thick concrete pad with roughened surface which was poured on the shake table (Fig. 2a). Fig. 2b documents the overturned objects after a typical experiment.

The test objects were exposed to the following 10 uniaxial acceleration time histories:

- East-West component of the 17 August 1999 Turkey earthquake recorded at Izmit, Turkey, with an aftershock about 30 seconds behind the mainshock.
- The North-South component of the 1985 Michoacan earthquake recorded at Caleta de Campos, Mexico.
- The N51E and N39W components of the 2002 Denali, Alaska, earthquake recorded at Pump Station 10.
- The (IMP_230) component of the 1979 Imperial Valley earthquake recorded at El Centro Array Station 5-2801.
- The (TCU052_1) and (TCU07490) components of the 1999 Chi-Chi earthquake, recorded at Taichung, Taiwan.
- Two random-vibration synthetic accelerograms with high and low PGV to PGA ratios.
- A 1 Hz full-sine wave acceleration time history.

All acceleration time histories were scaled to a range of PGA for the experiments, beginning with a PGA of 0.1g, below the rocking threshold of the most slender objects. For subsequent runs, while preserving the waveform, the PGA was increased by 0.025*g* increments to the point where all of the objects on the shake table overturned. Since the first overturning occurrence of an object does not necessarily mean that it will overturn in subsequent runs (e.g., with higher PGAs), based on our observations, we have adopted the convention of excluding an object from tests at higher amplitudes only after it had overturned three consecutive times.

Experiments are documented by video recording of each experimental run, by still pictures before and after each run (Fig. 2), and by scientific notes (UCCSN-UNR-085 vol. 1). Table motions were recorded both on the table's accelerometer and on a Kinemetrics K2 strong motion recorder that we installed on the table.

To ensure that the shake table generates the desired acceleration time histories, the recorded accelerations on the table were visually checked against the accelerogram that was used to excite the shake table. 3 compares accelerograms produced by the shake table (red traces) and the target waveforms (blue traces) for low- and high-frequency waveforms. The level of agreement is generally quite good. Due to the maximum table displacement of ±30 cm, the agreement deteriorates slightly at large displacements. However, these discrepancies do not affect our analyses since we utilize the acceleration time histories recorded subsequently on the shake table.

Fig. 4 shows a plot of the dynamic toppling accelerations (shake-table experiment) versus quasi-static toppling accelerations for the objects listed in Table 1. These objects were subjected to acceleration time histories with the waveforms similar to 10 different earthquakes and synthetic seismograms. We have used two different symbols to distinguish between seismograms for which PGV/PGA values are above or below the *arbitrary* threshold of 0.15. High-frequency seismograms have generally lower PGV/PGA values than the low-frequency seismograms. This plot indicates that there is a lot more scatter in the dynamic toppling acceleration when high-frequency seismograms were used in the experiment.

5.3.2 COMPARISON METHODOLOGY AND DISCUSSIONS

Purvance [9] provides relations for the high-frequency ground motion amplitude (PGA) associated with overturning at a specified probability as a function of the low-frequency ground motion amplitude (PGV/PGA) and the object's geometrical parameters (*e.g.*, height and slenderness). Both the PGV/PGA and PGA of each overturning occurrence of all objects on the shake table have been catalogued. In order to compare the overturning formulation with the experimental observations, one must first estimate the overturning probability corresponding to an observed proportion of overturning occurrences. In other word, the observed proportion of overturning occurrences of a specified object on the shake table does not correspond directly to an overturning probability. The corresponding overturning probability has been estimated by querying a set of numerically synthesized overturning responses of rectangular blocks exposed to a suite of ground motions. Using the relations in Purvance [8], one can calculate the overturning probability corresponding to an observed proportion of overturning occurrences. For instance, Fig. 5 shows the distribution of predicted overturning probabilities associated with the first overturning occurrence obtained from these numerical simulations. As a result, subsequent analyses utilize a value of 16% for the overturning probability to predict the first overturning occurrence observed in the shake table experiments. In the subsections below we first compare the overturning responses of rectangular blocks that are identical in size, but differ in composition in order to investigate the effects of material type on overturning response. In the following plots, the red symbols indicate the PGV/PGA and PGA corresponding to the first overturning occurrence of the specified object on the shake table, black lines represent the numerical predictions of Purvance [9], and the blue lines are the 5% and 95% prediction intervals.

5.3.2.1 Effects of Material Type on Damping

The precarious rock methodology is based on the assumption that balanced rocks experience only rocking motion during earthquakes. In our analysis, we assume that during impact (transition from one rocking point to the other) there is no bouncing or sliding *(perfectly inelastic* impact). Therefore, the angular momentum before and after the impact, about the point of impact, is conserved. (There is no change in the total external torque on the block because the impact force is applied at the point about which the torque is calculated [7].) However, because of the inelastic impact, the total energy is not conserved (loss due to deformations at the point of impact, including heat, sound, etc.). The energy loss results in a lower angular velocity after the impact. The ratio of the angular velocities before and after the impact is defined as the coefficient of restitution η:

$$\eta \equiv \frac{\dot{\theta}_2}{\dot{\theta}_1},$$

where $\dot{\theta}_1$ and $\dot{\theta}_2$ are the angular velocities before and after the impact, respectively. The value of η is less than unity. Based on the analytical solutions for two-dimensional rocking motion of a rigid block developed, the energy loss is a function of the aspect ratio (width/height). That is, the more slender the blocks are, the less energy they lose after an impact. For a rectangular block the coefficient of restitution takes the simple form

$$\eta = 1 - \frac{3}{2}\sin^2 \alpha,$$

where α is the angle between the vertical and the line through the center of mass and the rocking point (Fig. 1).

Theoretically, damping of a rigid block depends only on geometry. However, in practice the material can affect damping. In order to investigate variations in overturning due to material damping, blocks AL1 and AL2 and their exact wooden replicas W1 and W2, respectively, were tested on the shake table. The waveforms listed in section 5.3.1 were used as input to the shake table. Fig. 6 compares the numerical predictions [9] with the experimentally derived overturning. The wood (black symbols) and aluminum (red symbols) blocks overturned nearly identically. The data spread is somewhat beyond the prediction intervals estimated by Purvance [9]. Note that these blocks are well outside the parameter space investigated in that study, though. It is also possible that such small objects may have been influenced by the basal contact conditions (*e.g.*, grip tape elasticity).

5.3.2.2 Small Rectangular Blocks

In Fig. 7, shake-table results for overturning of six small rectangular blocks are compared with the numerical predictions [9]. These blocks consisted of aluminum blocks, AL1 and AL2, granite block G, and wooden blocks W1, W2 and W3. Blocks W1, W2 and W3 are the exact replicas of AL1, AL2, and G, respectively. These objects were subjected to the waveforms listed in section 5.3.1. The formulation of Purvance [9] predicts the overturning behaviors of blocks G and W3 adequately, but slightly underestimates the responses of blocks AL1, AL2 and their wooden replicas. The discrepancies could be attributed to the basal contact conditions and the frequency content of the input motions.

.

5.3.2.3 Steel I-Beams

Tall, steel I-beams have simple basal contact conditions and shapes. Also, by adding lead weights to I-beams, their geometrical parameters α, *R*, and the moment of inertia may be altered. For instance, certain configurations allow us to model symmetric and asymmetric homogeneous objects that are significantly taller than the steel I-beams by changing the location of the center of mass. Fig. 8 compares the numerical predictions [9] (black lines) with I-beam overturning data from the shake table experiments. The level of agreement is striking for both symmetric and asymmetric I-beams. Most of the data also fall within the prediction intervals, suggesting that the Purvance [9] predicts an appropriate range of realistic behaviors. Again, the waveforms listed in section 5.3.1 were used as input to the shake table.

5.3.2.4 Granite Boulders

Along with the rectangular blocks and I-beams, three granite boulders were selected to represent geometrically complex precariously balanced rocks found in seismically active regions. Fig. 9 compares the numerical predictions [9] (black lines) with the overturning data from the shake table experiments. The numerical model systematically overpredicts the PGA required for overturning. The trend of records with low PGV/PGA requiring larger PGA to overturn persists, though. These findings can be attributed to the fact that the numerical model utilized in [9] is based on objects rocking about two basal contacts corresponding to the geometric extent of the object (Fig. 10a). As the object tilts during rocking, the restoring force decreases nearly linearly with inclination (Fig. 10b). Objects that rock about multiple basal rocking points (Fig. 11a) produce more complex restoring force versus inclination responses (Fig. 11b) wherein the peak restoring force may be significantly reduced when compared to the simple model used in the numerical simulations (Fig. 10). We have developed a methodology to accurately measure the restoring force ($F = mg\tan(\alpha - \theta)$, where m is the mass, g gravitational acceleration, and θ the inclination) as a function of inclination via a winch, load cell, and inclinometer (Fig. 12). The object in question is pulled horizontally until the restoring force decreases approximately linearly with angle of inclination. Such measurements of precariously balanced rocks are feasible in the field provided special care is taken to avoid overturning the rock so that the rock can be returned to its original position. These data are processed via parameterizing the nearly linear decay, allowing one to obtain an estimate of the mass and slenderness associated with the final rocking point. The force is then normalized via the product of the mass and acceleration of gravity, and the arctangent of the peak normalized force is used as the reduced slenderness in the formulation of Purvance [9]. Fig. 13 shows the restoring force versus inclination curves for the three boulders tested in these shake table experiments. The peak normalized forces suggest that the slenderness may be reduced by 20% - 30% due to basal roughness. The resulting overturning predictions are shown in Fig. 14 (black lines) relative to those that do not account for the basal roughness as explained above (green lines). This methodology is both relatively straightforward to implement in the field and effective at parameterizing the overturning responses of objects with complex basal contact conditions.

5.3.3 CONCLUSION FROM NEW SHAKE-TABLE EXPERIMENTS

- A good level of agreement has been obtained between input and measured accelerograms in the experiments.
- Small wooden and aluminum block overturn nearly identically.
- Numerical predictions [9] of overturning of large objects with simple contact conditions (e.g., I-beams with sharp basal edges) agree well with the shake-table results. Thus experimentally observed overturning occurrence depend both on the low- and high-frequency ground motion amplitudes.
- Purvance [9] overpredicts the overturning PGA for boulders with complex basal contact conditions.
- Force versus inclination measurements provide a robust method to adjust the formulation of Purvance [9] to account for complex basal contact.

5.4 Field Test of Precarious Rocks in the Vicinity of Yucca Mountain

We carried out new field test (IPR-007) of five precarious rocks in the Yucca Mountain Area. Figs. 15 and 16 show the rocks and their locations. Two of the rocks are on the Yucca Mountain crest and the other three in Solitario Canyon, west of Yucca Mountain. Field tests to determine the quasi-static toppling acceleration were carried out on four rocks. One rock was spared because it would have toppled if we had tried to tip-test it. Instead, its alphas were measured directly. Table 2 summarizes the field-test results.

The quasi-static toppling accelerations for the tested rocks range between 0.07 g and 0.38 g. In Table 1, the '*' next to the rock 'Doozy' indicates uncertainty in this measurement. In the quasi-static toppling test (IPR-007) the horizontal force applied at the center of mass reaches the peak value just before the rock begins to tilt away. This peak value is defined as the quasi-static toppling force, provided that the force decreases with further tilt of the rock. However, if the contact between the rock and the pedestal is rough, the initial peak would be a *local* maximum and force might increase with tilt after a slight decrease. We normally continue pushing (or pulling on) the rock (while making sure that it does not overturn) to see whether or not there are any additional rocking points. Unfortunately, this rock is situated more than 6-feet above the ground on a steep slope. Due to the safety requirements at the Nevada Test Site (NTS), we were not allowed to monitor the tipping test with one person at the foot of the pedestal. Therefore, the test was stopped after reaching the first peak in the quasi-static force to avoid overturning of the rock.

Estimates of the dynamic toppling accelerations (0.09g to 0.49g) listed in table are 30% higher than the quasi-static toppling accelerations. This rough estimate is based on the results of Anooshehpoor *et al.* [2,7]. These approximate values only provide *upper limits* for ground motion at the location of the rocks. However, because of the small number of the tested rocks, the statistical uncertainties are large.

5.5 ESF Data Acquisition Using Existing High-Frequency Geophones

One important issue for constraining predictive models for potential ground motions at Yucca Mountain is to understand the coherence of earthquake motions throughout the proposed engineered facility. The variability of ground motions within the repository block from earthquake sources places constraints on uncertainties in ground motion predictions that are conducted for engineering design ground motions. Currently, point measurements have been made from local seismic network stations, including velocity response network stations, local accelerometers, ESF Pad downhole accelerometers, and from a number of portable instruments that have been deployed for special studies over the years. The geographic distribution of these stations and the data that has been acquired is limited. Observations from a dense array of instruments will constrain coherence of ground motions and the contribution of incoherence to the uncertainty of ground motion prediction in Yucca Mountain.

In the late 1990s LBNL installed 224 two-component geophones sets along the West-facing wall of the N-S drift of the ESF in a controlled source experiment to determine the 3-dimensional velocity structure of the material between the ESF level and the surface. These instruments were grouted in and left in place following the experiment. Each site consists of 2 component sets of 10 Hz geophones installed in a vertical and horizontal (perpendicular to the tunnel wall) geometry; 448 geophones in all. They were installed at 15 meter intervals for a total distance of 3.3 km.

A RefTek 6-channel recorder was installed in the ESF near Niche 3 to record 6 of the 10 Hz high-frequency geophones. The instruments are being recorded in order to evaluate the coherence of seismic energy at high frequencies along the ESF south ramp from local earthquake sources. This is a scoping study to evaluate the scientific value of the data from these high–frequency phones. Information regarding the geophone installation, type and orientation was provided by LBNL; no technical assessment of the state of the performance of these geophones has been conducted since the LBNL study. These instruments were installed for controlled source experiments in the 1990's and were left in place with contact leads exposed. UNR acquired connector leads in order to connect geophones to a digital portable seismic recorder.

Geophones at 100 m and 60 m intervals (Table 3) have been recorded on 6 channels of the portable seismic recorder. The data is being transmitted via the ESF fiber to an Antelope (BRTT, Inc.) recording system on the ESF pad and transmitted and recorded/archived in real-time in Reno. Data collection began on May 31, 2005 and continues to present. Several local, regional and teleseismic events have been recorded on the backwall sensors.

5.5.1 COHERENCE AND CROSS CORRELATION OF ESF SEISMIC RECORDINGS

To gain an understanding of the ground motion variations within the ESF tunnel at Yucca Mountain, we have conducted two preliminary analyses of waveforms obtained from the NI-3 array located on the west wall (also called backwall) of the ESF tunnel (near Niche 3). In the current recording scheme, six channels of the west wall array are recorded. Two recording layouts were analyzed from June 2005 through June 2006: the first consisted of recording 6 west wall geophones spacing approximately 100 m apart and the other used about 60 m spacing. Each layout has two phases: a vertical-component phase and a horizontal-component recording phase. The approximate dates for each layout and phase are listed in Table 3.

The last entry is not analyzed in this report due to lack of sufficient recordings since it began in late June 2006. Also, only recordings from September 2005 on are used in the present analysis due to a change in event excerpting methodology at that time, which makes events prior to that date less amenable to the particular semi-automatic methodology used in this study. We will be able to incorporate events prior to September 2005 in later analyses after the events have been picked for event start times.

The number of events actually used in the present analysis is also shown in Table 3. Besides two probable teleseismic events, the events ranged in magnitude from -0.2 to 4.9, with a mean of 1.5. Distances ranged from 7 km to 460 km with a mean of 85 km. Azimuthal coverage was biased toward the southeast and northwest, but all azimuths were reasonably well represented with at least 15 events in each 36° bin. For the probable teleseisms, only the surface-wave package was excepted, while all other events included the entire wavefield.

We explore two different methods of investigating variations in ground motion within the ESF tunnel. The coherence measurements primarily indicate how much the wavefield is changing between measurement points as a function of frequency. The cross-correlation measurements we show are done at zero lag and thus indicate directly how the ground motion at point A is related to point B at the same times. This is a different view of ground motion from the coherence measurement. An arrival delay of half a cycle between two perfectly coherent waveforms will result in nearly anticorrelated ground motions between two sites which could lead to collision between nuclear waste storage casks. This difference between the two measurements is primarily coherence that disregards phase information, whereas cross-correlation is dependent on phase.

5.5.2 COHERENCE METHODOLOGY

With the coherence measurement, we are quantifying how much the waveform itself changes as it propagates along the array as a function of frequency. In a perfectly homogeneous material, the waveform would be perfectly coherent along the array although time delays in the arrival of the wavefield at each point would exist due to differences in the travel times. Although coherence is only weakly affected by small differences in wavefield alignment, we independently align the P and S wavefields for each event and each recording pair using cross-correlation to minimize the effects of travel time delays between recorders before computing the coherence.

We use the MATLAB coherence function to compute the coherence as a function of frequency. This function utilizes Welch's periodogram method, which divides the wavefield into equal, overlapping time windows to estimate the cross and individual spectral densities of the signals. The length of the time windows determines the amount of smoothing that is applied to the amplitude spectra. Small windows have little smoothing, so highly precise spectral peaks can be measured, but at the cost of spurious random noise spectral peaks as well. Larger windows mitigate the effect of random noise in the spectral estimates, but smear the signal peaks over broader spectral ranges. Based on tests performed on artificial, noisy signals, we determined the optimal window length to use. Although the window lengths were not identical for all events, they were approximately 2 seconds. This choice gives spectral resolution of about 1.5 Hz for the coherence measurements. Only frequencies with signal-to-noise ratios (as determined by a 9 s window before the P arrival) greater than 10 are used in our analysis. We show coherence results from 0.4 to 16 Hz.

5.5.3 CROSS-CORRELATION METHODOLOGY

The cross-correlation measurements quantify the relationship between ground motions at a given time between two points within several frequency bands. Waveforms are filtered into frequency passbands of 0.5 – 1.0 Hz, 1.0 – 2.0 Hz, 2.0 Hz – 4.0 Hz, 4.0 Hz – 8.0 Hz, and 8.0 Hz – 16 Hz (Fig. 17). Each band for each recorder pair for each event is then cross-correlated at zero lag if the signal-to-noise ratios for both recorders are greater than 10 in that band. Since we are computing cross-correlations at zero lag (*i.e.* no time shifts are applied), the distinction between P and S wavefields is not made in this analysis. Instead, the entire wavefield from both recorders is used to compute the cross-correlations.

Cross-correlations are sensitive to relatively small differences in alignment of waveforms, as opposed to coherencies which are not. Since we do not apply time shifts to the waveforms in the cross-correlation analysis, azimuthal dependence of the cross-correlations may exist depending on the apparent velocity of the incoming wavefield on the array. Wavefronts parallel to the axis of the array will give near infinite apparent velocity across the array, with the wavefield arriving simultaneously at all recorders. Wavefronts perpendicular to the array axis would be expected to give the largest delays between arriving wavefronts at the recorders. Although this expected arrival-delay pattern is observed in the data, the difference is relatively minor since almost all events have wavefronts impinging on the array from below at very nearly vertical incidence. However, since we might expect cross-correlations to be higher for wavefronts arriving parallel to the array than perpendicular to it, we have divided the events into azimuth and distance bins to investigate dependence on these variables in addition to presenting the overall averages for each layout.

.

5.5.4 COHERENCE RESULTS

The results from the coherence study are displayed in Fig. 18. The three phases so far completed are shown individually. Each figure displays coherence as a function of frequency and inter-recorder distance averaged for all events. Inter-recorder distances that are the same, such as from geophone 1 to geophone 2 and from geophone 2 to geophone 3, are also averaged to produce these plots. High coherence is indicated by deep red, whereas low coherence is shown as deep blue. One basic result for both P and S waves for all phases is that higher coherence is found where frequencies are lower and inter-recorder distances are smaller, as expected. Coherencies near unity are found universally for frequencies of 0.4 Hz and distances of less than 100 m. P-waves demonstrate higher coherency values at nearly all frequencies and distances compared to S-waves. It should be noted that P-waves, in general, have a higher frequency content than S-waves and, thus, there are fewer P-wave coherency values in the lower frequency averages for P than for S, and vice-versa. The rapid drop in coherency values with frequency is very evident from the plots. One interesting feature that appears more or less consistent among the figures is the clear coherency minimums at about 2-3 Hz, 5 Hz and perhaps about 12 Hz, separated from each other by relative maxima. The drop from values near unity at 0.4 Hz at nearly all distances to values near zero in the 2-3 Hz range at larger distances is especially conspicuous. Even at 100m distance, there is a minimum in coherence at these frequency values. This pattern may represent some sort of resonance effect within the tunnel itself, especially since they seem to approximately follow an octave relation. The average spectra for the events across the array does indicate a peak amplitude at the lowest frequencies dropping significantly to a minimum in spectral amplitude at about 3 Hz. The minima at about 5 and 12 Hz are weakly mimicked in the average spectra.

Since random seismograms will have a distribution of coherencies centered at about 0.1, we selected a coherency value of 0.3 to indicate minimum significant coherence. Based on this selection, generally P-waves are significantly coherent at all tested frequencies out to 300 m distance on the vertical components, with a general drop-off with increasing frequency and distance. Beyond 300 m, P-waves show significant coherence only in the frequency bands with the coherence maxima discussed in the previous paragraph. Vertical component P-waves are coherent above 0.7 for all distances at frequencies less than 1 Hz. Horizontal component P-waves have much lower coherence in general compared to their vertical counterparts. Besides lacking sufficient signal-to-noise ratios at frequencies lower than 1.5 Hz, there is only significant coherence up to about 6 Hz at 100 m and about 3 Hz at 200 m.

Vertical component S-waves show significant coherence only at the lowest frequencies and smallest distances. S-waves are coherent up to about 9 Hz at 60 m, drop to about 4 Hz at 100m, and are generally confined to frequencies less than 1.5 Hz for farther distances. They exhibit coherencies above 0.7 for all distances only at 0.4 Hz, but are above 0.5 for 0.8 Hz only at distances less than 400 m. Horizontal component S-waves do demonstrate slightly improved coherencies at most frequencies and distances, but the improvement is marginal. It should be noted that it is possible that the azimuths of the horizontal components of the geophones are not identical, which would cause a deterioration of the coherence measurements in the horizontal directions. This possibility will need to be addressed in future research.

5.5.5 CROSS-CORRELATION RESULTS

The cross-correlation results are displayed in Fig. 19. These results plot the average over all events within a given phase as a function of distance and frequency. One point is plotted for every geophone pair. The same general trends are witnessed in the cross-correlations as in the coherencies: decreasing correlation with higher frequencies and larger distances. The 0.5 – 1.0 Hz band clearly shows the highest correlations at all distances, being well above higher frequencies at all but the closest distances. For reference, cross-correlations of random seismograms produce values centered around 0.3 and -0.3, so only cross-correlations with absolute vales greater than about 0.5 are significant.

Only the 0.5 – 1.0 Hz band is significantly correlated at all distances and in all phases. Vertical components at all frequencies are significantly correlated at 60 m, but by about 100 m, only frequencies lower than 2 Hz are significantly correlated, and all but the 0.5 – 1 Hz band is significant beyond about 200 m. Negative cross-correlations exist but never show values less than -0.2 for these averages. The horizontal components show slightly higher correlations at 0.5 – 1 Hz compared to the verticals at all distances, but smaller correlations for frequencies higher than 2 Hz. This may be due to the horizontal components not being consistently aligned in azimuth, as discussed above.

We have divided each completed phase into four receiver-to-event azimuth bins centered on 0°, 90°, 180°, and 270° to investigate any azimuthal dependence in the cross-correlations. During the first phase (100 m spacing, verticals), only the 180° and 270° bins sample all frequencies. There does appear to be a sharper drop in cross-correlations with distance at 180° than at 270° for frequencies lower than 4 Hz, which is not unexpected. The other two azimuth bins are too poorly sampled to give a clear indication of dependence. The horizontal component phase only provided full frequency coverage for the 180° bin, but the 0° bin contained all but the 0.5 – 1 Hz band. The horizontals showed rapid drop-off in correlations with distance for all frequencies like the 180° bin for the first phase except for the lowest frequency, which behaved more akin to the 270° bin in the verticals. There may be some indication of faster fall-off with distance at 180° than at 270° in the horizontals where frequency comparisons are available, but it is not as clear as in the verticals case. Also, the 0° bin may indicate a faster drop in correlations with distance than the 180° bin. The third phase (verticals at 60 m spacing) provided the most number of events and, thus, the best azimuthal coverage, but still only the 90° and 270° bins obtained full-frequency coverage. A clear difference between the 90° and 270° bins is observable with the 90° bin demonstrating much faster correlation drop-off with distance at all frequencies. This cannot be an array-alignment issue, so it must be due to structural differences between east- and west-directed paths such as the generally gently east-dipping stratigraphy and topography of the mountain. Within the frequency bands that the 0° and 180° bins sampled, cross-correlations appear to behave more akin to the 90° bin than the 270° bin.

The cross-correlations were also divided into station-event distance bins of 10-20 km, 20-40 km, 40-100 km, 100-200 km, and 200+ km. Unfortunately, the statistics for the first two phases of the study are so poor that discussion of any trends would be speculative at best. The third phase, however, does have enough correlation samples that some general trends may be ventured, but these are still very preliminary due to the dearth of events that contribute to each sample point. Three of the five distance bins have full frequency coverage. A slight tendency to slower drop-off with distance at farther station-event distance may be indicated, especially in the 0.5-1.0 Hz band; but this may also be due to confounding effects such as azimuth or other factors since there are so few events for each sample point. We have also divided the events into five magnitude bins; but results are very similar to the distance bins, being fairly equivocal with perhaps a slight trend for larger events to show slower correlation drop-off with inter-station distance. Both the distance and magnitude dependence needs to be strengthened by more events before any clear statement can be made.

5.5.6 DISCUSSION

Both the cross-correlations and coherencies indicate the ground motions lose coherence at distances on the order of 100 – 200 m and frequencies higher than 1 Hz within the ESF tunnel. Coherence and cross-correlation values are no different from random seismograms in this distance-frequency region, except that cross-correlations were predominantly positive instead of only 50% positive as would be expected for random events. At distances less than about 200 m, coherency values and correlations are significant to about 10 Hz for both P and S waves, with P waves having higher coherencies and cross-correlations than S-waves. Correlations and coherencies are excellent at frequencies less than 1 Hz for all distances, except for S-waves, which only display moderate values at distances beyond 300 m. These results indicate that the tunnel area exhibits strong scattering, especially of S-wave energy, even over distances as short as 200 m and for frequencies as low as 1-1.5 Hz.

This present scoping study gives preliminary results of coherencies and ground motion correlations at 100 and 60 m inter-station distances for about 300 mostly small (less than magnitude 2) earthquakes. A wide range of correlation distances need to be examined with a sufficient number of events to obtain a reliable estimate of real ground motions within the ESF tunnel. Eventually, 10 m spacing would be desirable for direct empirical estimates of variations in ground motion between nuclear waste storage casks. The lack of events above magnitude 3 or 4 within 100 km of the array in the present study period prevents useful and trust worthy extrapolations to large magnitude events that could occur on local and region faults in the area such as on the Furnace Creek fault system. Time is the only way to increase earthquake azimuthal, distance, and magnitude distribution. Events with magnitudes 4 or larger have occurred in the local area, but their recurrence is such that on the order of a decade of data will be required to get a sufficient distribution for robust statements of coherency to be made.

The two computed quantities in this discussion, coherence and cross-correlation, contribute to an understanding of ground motion in different ways. Coherence is an empirical measure of the variation of the wavefield as it propagates along the array. These variations can be due to structural variations such as scattering in the local environment or to variations along the wavefront that have propagated directly from the source or from structural effects along the path. Azimuthal, distance and magnitude variations in coherence may be useful in separating local from extra-local sources of decoherence in the wavefield. In addition, transfer functions from one array point to another in the tunnel would allow simulations of large magnitude events and their resulting expected ground motions. This, of course, necessitates at least moderate magnitude events to have been recorded for more reliable extrapolation.

Cross-correlations, on the other hand, empirically measure ground motion variations between two points at the same time including phase and arrival delays. A half-cycle delay in perfectly coherent wavefields will result in a potentially disastrous situation of adjacent casks moving in opposite directions. Based on our present results, there are only small anticorrelations of ground motions between points; the cross-correlations display predominately positive cross-correlations. Correctly predicting the ground motions from simulated earthquakes will require careful calibration based on actual earthquake wavefield coherencies and their corresponding cross-correlated ground motions.

None of the observations or analyses, coherence or cross-correlation, have indicated the existence of lens-like inhomogeneities which could lead to extreme lens-like focusing, with consequent extremely high ground motions.

5.6 Simplified Probabilistic Seismic Hazard Analyses for Precarious Rocks near Yucca Mountain, Nevada

The probabilistic seismic hazard analysis for Yucca Mountain, Nevada, is published by Civilian Radioactive Waste Management System Management and Operating Contractor [4], which will be referred to subsequently in this paper as the YM-PSHA. The analysis, also summarized by Stepp *et al.* [10] and with more hazard curves shown in BSC [3], evaluated the hazard for a hard-rock site near the crest of Yucca Mountain (Fig. 16). The location is significant because it is above the underground location for the designated United States repository for high-level nuclear waste. The key feature of the analysis was that teams of scientists independently developed input models, with uncertainties, for the analysis. These individual models were used to obtain multiple estimates of the seismic hazard. The differences among the models are interpreted as a representation of the uncertainty in the hazard.

The hazard curves generated by the YM-PSHA have been extended to annual occurrence rates of 10^{-8} per year (Figs. 20, 21). At that occurrence rate, they predict ground motions that are quite large, when considered in the context of past observations. The mean value of the peak acceleration is about 11g, and the mean value of the peak velocity is 1300 cm/s for annual occurrence rates of 10^{-8} per year. For comparison the largest observed peak acceleration worldwide is about 2-3 g, and the largest observed peak velocity is about 200-300 cm/s.

These large values seem to be contradicted by some of the geological features of Yucca Mountain. Brune and Whitney [5] have observed precariously balanced rocks which would be toppled by accelerations significantly greater than 0.5g, for instance, and a velocity in the range of a few meters per second would be expected to shatter the solid rock of the mountain, since strain is proportional to velocity. This contradiction suggests that the YM-PSHA must have some invalid components in its makeup, resulting in the extremely large ground motions.

A goal of this study is to understand the analytical processes that are taking place that result in the large values for the YM-PSHA. Because of the complexity of the process, in which millions of combinations of models were evaluated, our object is to simplify the problem in order to understand the essence of the contributions resulting in the extreme values. Thus first we develop a simplified input that predicts similar hazard curves. We then carry out various investigations regarding the relationship of the input decisions to the resulting consequences. We test these various decisions against selected precarious rocks near Yucca Mountain and draw summary conclusions.

5.6.1 APPROXIMATE PROBABILISTIC SEISMIC HAZARD ANALYSIS FOR YUCCA MOUNTAIN

Fig.16 shows an aerial photographic image of Yucca Mountain, annotated with the locations of the site used for the YM-PSHA and the locations of five precarious rocks. Table 4 lists the geographic coordinates of each of the six features on Fig. 16. Figs. 20 and 21 show the results of the YM-PSHA for the site PSHA. The first objective is to develop an input to a seismic hazard analysis code that approximately reproduces the features of Figs. 20 and 21.

5.6.1.1 Ground motion prediction equations

There are two main inputs to a probabilistic seismic hazard analysis. The first is a ground motion prediction equation giving the ground motion at a site as a function of magnitude, distance from the fault, and other parameters. YM-PSHA involved six scientists that developed independent ground motion models. These scientists give point estimates of ground motion which were then fit with a common equation. The equation predicts the natural log of the median ground motion (μ) as follows:

For $M<m_1$,

$$\begin{aligned}\mu &= a_1 + a_2(M-m_1) + a_6(8.5-M)^2 + \left[a_3 + a_5(M-m_1)\right]\ln\sqrt{R^2+a_8^2}\\ &\quad + a_7F + a_9W_Hf_1(M,R) + a_{10}W_Ff_1(M,R)\end{aligned} \tag{1a}$$

And for $M>m_1$,

$$\begin{aligned}\mu &= a_1 + a_4(M-m_1) + a_6(8.5-M)^2 + \left[a_3 + a_5(M-m_1)\right]\ln\sqrt{R^2+a_8^2}\\ &\quad + a_7F + a_9W_Hf_1(M,R) + a_{10}W_Ff_1(M,R)\end{aligned} \tag{1b}$$

In Equation 1, M is the magnitude of the earthquake and R is the closest distance from the fault to the station. The variable F is a flag for focal mechanism (0=strike slip, 1=normal), W_H is a hanging wall flag (1=hanging wall, 0=not hanging wall), and W_F is a footwall flag (1=footwall, 0=not footwall). The parameters a_1 ... a_{10} and m_1 are fitting parameters chosen to predict the ground motions estimated by the experts. The parameter m_1 is an earthquake magnitude that allows the shape of the equation to be different for small and large magnitudes. YM PSHA uses $m_1 = 6.25$ for all models. The function $f_1(M,R)$, given by YM-PSHA (page 6-2 of Volume I), takes values between 0 and 1 to characterize the extent that the ground motion is affected by proximity to a hanging wall or footwall of a dipping fault.

In multiple occurrences of earthquakes with the same magnitude and distance, it is expected that differences in details of the source function and propagation path will cause variation in the actual ground motions with some probability distribution. In YM-PSHA, this variability is considered to be irreducible randomness in the process. Such irreducible randomness is defined as *aleatory* variability. The YM PSHA modeled The distribution of the natural logarithm of the ground motion amplitudes relative to the median value, μ, as a normal distribution, and the standard deviation of the distribution, more properly called the aleatory standard deviation (σ_{al}) is given as follows:

For $M < b_4$

$$\sigma_{al} = b_1 + b_2(M - b_4) \tag{2a}$$

and for $M \geq b_4$

$$\sigma_{al} = b_1 \tag{2b}$$

In Equation 2, b_1, b_2, and b_4 are parameters set up to achieve the desired characteristics of the model.

The YM-PSHA also recognizes epistemic uncertainty as an essential part of the model. Epistemic uncertainty is defined as uncertainty due to lack of knowledge. For instance, because there are no strong-motion accelerogram records from sites on the hanging wall of a normal fault during an earthquake with M>7, it is expected that there will be uncertainty in the mean value of such future observations. That uncertainty is the *epistiemic* uncertainty. Once there are hundreds of such observations, the mean value will be well defined, but due to the variability in the process they will not all be identical. That remaining variability is the aleatory variability, but without data the standard deviation of that aleatory uncertainty is also uncertain. Thus, epistemic uncertainty is used to represent the uncertainty in the mean value, μ, and the uncertainty in the aleatory standard deviation, σ_{al}. This is necessary because very little strong-motion data exists for normal faulting earthquakes, recorded on rock, at near-field distances. Thus it is appropriate to recognize that the mean and the standard deviation are uncertain. Epistemic uncertainty is defined using two parameters, σ_μ which gives the standard deviation of a normal distribution for the best estimate of μ, and σ_σ which gives the standard deviation of a normal distribution for the best estimate of σ_μ. The parameters σ_μ and σ_σ are allowed to depend on magnitude and distance. Equations for σ_μ and σ_σ are given by YM-PSHA (page 6-2 to 6-3, Volume I).

Parameters for all models are also given by YM-PSHA (in Volume 3, Appendix I) [4]. For this study, three of the models have been considered; but most of the figures use the model by John Anderson. This model is interesting to explore because it has the largest value of σ_μ, and as a result it predicts the highest overall hazard curves. The median ground motions from this model, and its estimates of σ_{al} and σ_σ, are not substantially different from the estimates in the other models. It should be noted that none of the ground-motion prediction equations yield hazard curves that appear to be consistent with precarious rocks. Thus, conclusions on how, or if, the Anderson model can be modified in order to be reconciled with precarious rocks will be most valuable, and will identify issues that apply to all of the models. The other two models used in this study are the models by Arthur McGarr and Maryann Walck. These are chosen because over certain magnitude and distance ranges these two models tend to give the smallest ground motions.

5.6.1.2 Seismicity Model

The second essential part of the input to the seismic hazard analysis is a model of the seismicity, giving the rates of earthquakes as a function of magnitude and location. For the YM-PSHA, six teams of three scientists each proposed models. In general each team came up with more than one model, and provided uncertainties on the magnitudes and rates. Once again, in order to simplify the problem, we sought to make a single model that can be used as a "typical" example. An additional constraint was that, when used with the Anderson ground-motion model, the mean hazard curve should be close to the mean obtained from the complete hazard analysis.

The model adopted here is similar but not identical to a model proposed by the team of Al Rogers, Jim Yount, and Ernie Anderson (RYA). Our model is illustrated in Fig. 22. RYA models the seismic sources with a diffuse source zone around Yucca Mountain, plus several faults for which they identify magnitudes and occurrence rates (all with uncertainties). Table 4 gives the activity rate for earthquakes on each of the eight faults shown in Fig. 20, with these faults selected from a larger set in the RYA model because they are nearest to the sites. RYA use a circular diffuse source zone, but since the input to the probabilistic seismic hazard analysis code used here is more easily described with rectangular zones we created a rectangular zone that totally encompasses the circle of 100 km radius, and adjusted the earthquake occurrence rate to achieve the same areal density. The RYA model specifies higher density of earthquakes in the southwestern part of their zone, but for our input the entire zone is assigned a spatially uniform rate. Table 4 gives the rates of earthquakes in circular rings around the site, rather than the total rate for the entire zone. The rates in Table 4, while starting with mean rates in the RYA model, were adjusted interactively in order to achieve certain properties of the hazard curves that were computed subsequently.

5.6.1.3 Hazard Curve Computation

For this exploratory analysis, hazard curves were computed with a computer code *EQR2006y* (JGA Program) This code has been used for several previous probabilistic seismic hazard analyses (*e.g.* [11, 12]). The code is sufficiently flexible that only minor changes were required in order to adapt it to the YM-PSHA form of the ground-motion prediction equations. The code did not need to be modified to accommodate the faulting, although for simplicity we assumed that the site was on the hanging wall of a normal fault regardless of the actual fault geometry. This introduces a small bias towards slightly higher hazard curves.

A key part of the calculation of a hazard curve is the calculation of the probability that a ground motion parameter, g, in a particular earthquake of magnitude M and at a distance R from the site will exceed a given ground motion amplitude, g_0. In general, suppose that the probability density has the form $p(g|M,R)$. Then the exceedance probability is given by:

$$p_E = \int_{g_0}^{\infty} p(g|M,R)\,dg\,. \tag{3}$$

For the procedure used in YM PSHA, where $\mu = \ln g$ is taken to obey a normal distribution, let $\mu = \mu(M,R)$ as given by Equation 1. Then for the median model

$$p_E = \frac{1}{\sigma_{al}\sqrt{2\pi}} \int_{\mu_0}^{\infty} \exp\left[-\frac{(y-\mu)^2}{2\sigma_{al}^2}\right] dy\,. \tag{4}$$

For the model that includes the epistemic uncertainty, Equation 4 is replaced by

$$p_E = \frac{1}{\sigma_a \sqrt{2\pi}} \int_{\mu_0}^{\infty} \exp\left[-\frac{(y-\mu_1)^2}{2\sigma_a^2} \right] dy \,. \tag{5}$$

where

$$\mu_1 = \mu + \varepsilon_\mu \sigma_\mu \tag{6}$$

and

$$\sigma_a = \sigma_{al} + \varepsilon_\sigma \sigma_\sigma \tag{7}$$

In order to numerically implement the effects of the epistemic uncertainty described by σ_μ and σ_σ, YM-PSHA developed ten ground-motion prediction equations from the model provided by each of the ground motion experts. Each of these cases is assigned a separate value of ε_μ and ε_σ. The relationship of these ten models to the median model is given in Table 5, and shown graphically in Fig. 23. For instance, case b would have ε_μ=0.74 and ε_σ=1.73. This means that the hazard curve is computed using an aleatory uncertainty that is equal to $\sigma_{al} + 1.73\sigma_\sigma$, instead of σ_{al}. Similarly, the median ground motion is adjusted to $\mu + 0.74\sigma_\mu$. The resulting hazard curve, in this case, is naturally greater than the median curve since both the median and the uncertainty is increased. For programming convenience, as shown in Table 5, some values of ε_μ and ε_σ were rounded off to one place beyond the decimal, with minimal impact on the results. YM-PSHA use a weighted average of these ten curves to find the mean hazard curve that approximates the effect of the epistemic uncertainty on the median and standard deviation of the ground-motion equations. The mean of the hazard curves is taken in linear space, rather than logarithmic. The weights for each of the ten models are given in Table 5.

5.6.1.4 Initial Hazard Curve Results

Fig. 24 shows several features of the probabilistic seismic hazard for peak acceleration, and Fig. 25 shows the same features for peak velocity. First, these figures show four curves from the YM-PSHA model (medium weight lines). These are the median and mean hazard curves of all the expert models, and the hazard curves that exceed 5% and 95% of the multiple models, from Fig. 20 and 21. The ten models used to approximate the effect of the epistemic uncertainty, as given in Table 5, are shown in Figs. 24 and 25 using light lines. The heavy black line, labeled "median", is computed from the ground motion model and seismicity model with $\varepsilon_\mu = 0$ and $\varepsilon_\sigma = 0$. It will be noted that the median hazard curves computed here for both peak acceleration and peak velocity practically overlay the median curve from YM-PSHA. Reproduction of the median YM-PSHA hazard curve was the objective that was achieved through minor adjustments to the seismicity model.

For mean occurrence rates smaller than 10^{-5} per year, the mean from the Anderson model exceeds the mean from YM-PSHA. This is the result of Anderson using a greater value of σ_μ than the other modelers. At the 10^{-5} occurrence rates, there are enough small earthquakes that some of them will have ground motions significantly greater than the median values according to this modeling assumption. Out of more than 100 earthquakes (Table 4), a few of the events would be expected to have ground motions more than two standard deviations above the median. At the 10^{-4} level, perhaps as few as 10 earthquakes occur on average, so that most likely none would be so far above the average. Thus the higher epistemic uncertainty becomes more significant as the annual occurrence rate decreases, driving this mean curve to higher values than the average using the six ground-motion models.

Considering Figs. 24 and 25, we conclude that the models described above are capable of reproducing the main features of the YM-PSHA. We therefore use these curves as a base case for subsequent investigation of the factors affecting the seismic hazard computation.

5.6.2 HAZARD AT THE PRECARIOUS ROCK SITES

Next we computed the probabilistic seismic hazard using this model for the sites of the five precarious rocks shown in Fig. 16. The results were that the differences between the hazard curves at those five sites and the hazard curve at the PSHA site were small, as shown in Fig. 26 for peak acceleration and Fig. 27 for peak velocity. Therefore, we concluded that it is sufficient to continue to investigate the seismic hazard only at the PSHA site, and to apply the results to all of the precarious rock sites as well.

5.6.3 ROLE OF ALEATORY UNCERTAINTY ON THE PROBABILISTIC SEISMIC HAZARD CURVES

Figs. 28 and 29 are presented to show the effect of aleatory variability, σ_A, on the YM-PSHA curves for peak acceleration and peak velocity, respectively. The red lines in these plots show the median models that have been presented previously. To investigate the contribution of the aleatory uncertainty to the hazard, the black lines in these figures show what happens if the aleatory uncertainty in the Anderson model is replaced with $\sigma_A = 0.01$, as a numerical approximation to the case where there is no aleatory uncertainty. The median model and the model for $\sigma_A = 0.01$ are very similar for annual occurrence rates less than 10^{-3}, and start to diverge very rapidly at rates less than about 10^{-5}. These figures show that under these assumptions the peak acceleration rises only to about 0.55 g at the annual rate of 10^{-8}. The peak velocity rises only to about 45 cm/s at the annual rate of 10^{-8}.

These results can be understood by reference to the seismicity model in Table 4. Few of the possible earthquakes in the model have an occurrence rate greater than 10^{-3} per year. Thus, at these probability levels, the occurrence-rate curves in Fig. 23 and 24 are approximately representing the mean ground motion from the earthquakes in the model. Earthquakes that occur at most only a few times per 10^5 years dominate at probabilities in the range from 10^{-5} to 10^{-3}. Thus this is the range where the hazard curve with uncertainty starts to diverge from the curve with no aleatory uncertainty. For probabilities below 10^{-5}, all of the source zones have large numbers of earthquakes. In this range the hazard curves are dominated by the probability that one or a few of these repeated earthquakes will have a rare ground motion that is much greater than the mean value. In this range, when $\sigma_A = 0.01$ the hazard curve does not increase significantly as the annual occurrence rate decreases because repeating earthquakes in an individual source zone all give the same ground motions. For the large values of σ_A, the statistics of the upper tail on the probability distribution of ground motions from repeated individual earthquakes dominate the calculated occurrence rate curves.

Figs. 28 and 29 suggest that in the extreme limit where the aleatory uncertainty goes to zero (referred to as the characteristic ground motion earthquake by Anderson and Brune [13]), the results of the seismic hazard analysis for Yucca Mountain would give unsurprising values for the ground motions even at annual occurrence rates of 10^{-8} per year.

One practice in PSHA is to truncate the uncertainty in the ground-motion prediction equations at some positive multiple of σ_A, for instance at $2\sigma_A$ or $3\sigma_A$. This is achieved at the point where the code determines the probability that a specific earthquake will exceed some selected ground motion. If the selected ground motion is more than the threshold number of standard deviations above the median, then rather than using the small probability from the lognormal distribution, that probability is set to zero. This practice was not used in YM- PSHA. However, since it is used in some other applications, it is interesting to find out what impact this might have on the results of YM-PSHA. Figs. 30 and 31 explore this for the median ground motion model of Anderson, and Figs. 32 and 33 explore the results when this truncation is applied to the suite of the ten models used to implement the epistemic uncertainty.

The effect of the truncations on the hazard computed with the median ground-motion model, shown in Figs. 30 and 31, is to lower the hazard. Truncation at $3\sigma_A$ primarily affects the median curve at rates below about 10^{-7} per year. Truncation at $2\sigma_A$ starts to show strong effects on the median curve at rates on the order of 10^{-6} per year. Truncation at $+1\sigma_A$ starts to show strong effects on the median curve at rates of approximately 10^{-5} per year, but is impacting the hazard curve to a lesser extend at rates as high as 10^{-3} per year. These truncated curves converge towards the curve computed using $\sigma_A = 0.01$. Thus, truncation has an effect on the hazard curve that is similar to the effect of decreasing σ_A.

In contrast, in Figs. 32 and 33, the impact of truncation is relatively small on the mean hazard. The mean hazard is of course reduced, but it remains greater than the median for the baseline model. The cause is that the epistemic uncertainty is dominant source of uncertainty in this model. This, considering that truncation and decreasing σ_A have a similar range of effects on an individual hazard curve as shown in Figs. 30 and 31, suggests that if a decrease in σ_A is accompanied by an increase in σ_E, the net effect on the hazard curve is not necessarily large.

5.6.4 CONSISTENCY WITH PRECARIOUS ROCKS

Considering the dynamics of precarious rocks, we have calculated the probability that a subset of the precarious rocks described in Table 2 would be overturned given the hazard curves based on the $\sigma_A = 0.01$ median ground-motion model (Figs. 28 and 29) and the suite of 10 ground motion models corresponding the various cases of ε_μ and ε_σ given in Table 5. This work is based on the formulation of Purvance [9] that discretized the overturning probability as a function of the rock geometry along with the low- and high-frequency ground motion amplitudes. In order to simplify the analysis at this point, we have assumed that there is a perfect correlation between the PGV and PGA as opposed to implementing a complete vector-valued PSHA as utilized in

Purvance [9]. In the implementation, we determined a multiplier V_a such that when the peak acceleration axis of the acceleration hazard curve is multiplied by V_a, the acceleration hazard curve will match the hazard curve for peak velocity. Then only the acceleration hazard curve and V_a are used to estimate the overturning probability. This gives us a lower bound on the overturning probability, as in general when acceleration and velocity are not perfectly correlated the overturning probability increases. In addition, the 5% and 95% prediction intervals on the overturning probability are provided via the error bars. This formulation has been validated via comparison with shake-table experiments [9]. We have also assumed that these precariously balanced rocks have been in their current positions for 10,000 years based on the ^{36}Cl cosmogenic age dates rock varnish evidence [14]. Note that this is a minimum age.

The overturning probabilities of the precarious rocks Fluffy (FL), Red Eye (RE), Walks a Long Way (WLW), and Tripod (TR) are shown in Fig. 34 when exposed to the median ground motion model (e.g. ε_μ and ε_σ set to 0). The corresponding median overturning probabilities are 0.51, 0.47, 0.80, and 0.62, respectively. Taken individually, it appears as though these rocks may or may not be consistent with the $\sigma_A = 0.01$ median ground-motion model. Assuming that the overturning occurrences are statistically independent, the probability that all four rocks would survive simultaneously is 0.020 (*i.e.*, (1-0.51)*(1-0.47)*(1-0.80)*(1-0.62)). In other words, this ensemble of rocks is inconsistent with even the $\sigma_A = 0.01$ median ground-motion model, requiring even smaller mean value.

A similar analysis for the ensemble of rocks on Yucca Mountain is depicted in Fig. 35 for the median ground motion (case M) along with the suite of 10 ground motion models considered herein (*i.e.*, those given in Table 5). The median and cases a, b, c, d, e, i, and j ground motion models are largely inconsistent with the precarious rocks present on Yucca Mountain. The ground motion models with unchanged or inflated median values (*e.g.*, cases M, a, b, c, d, and e) are the most inconsistent with the actual rocks. In addition, cases i and j with slightly deflated median values but increased aleatory uncertainty are also inconsistent with these rocks. Cases f, g, and h, with both deflated median and aleatory uncertainty, are more consistent with the rock models. These results highlight the tradeoffs between median values and the aleatory uncertainty.

5.6.5 DISCUSSION

It is difficult to know how to estimate the magnitude of the epistemic uncertainties, σ_μ and σ_σ. One approach applied with judgment by the ground motion panel in YM-PSHA deserves some discussion. The ground-motion panel was asked to estimate point values of the ground-motion parameters for a large number of combinations of magnitude and distance. These point values were subsequently fit with Equation 1, as mentioned above. In developing the point values, the modelers considered several “advocacy models”, which were ground-motion prediction equations developed previously (but not necessarily published). These may have been modified for the hard-rock site condition at Yucca Mountain. Some were developed primarily from fitting data but some were developed from synthetic seismograms. Point values can be estimated by taking a weighted average of the median values of the advocacy models. Then one simple way to estimate σ_μ and σ_σ is to look at the standard deviation of the median ground motions and standard deviations of the advocacy models. In developing his estimate of σ_μ, Anderson considered that method likely to underestimate the complete uncertainty, since none of the models were constrained by observations in the near-field of large normal-faulting earthquakes, the type expected in the vicinity of Yucca Mountain. Furthermore, he wanted to be sure that, on the low side, the models would have a non-negligible probability that the median of the distribution would be consistent with the emerging data on precarious rocks. This led to his estimate of σ_μ that was larger than the other models.

One question that has come up is what would be the impact, considering that line of reasoning, if Anderson had provided an asymmetrical distribution for μ instead of a normal distribution. That is easily tested through development of a reweighting scheme that approximates the effect of a different, non-Gaussian distribution of ε_μ and ε_σ. Table 6 presents a reweighting scheme that is strongly skewed to favor non-positive values of ε_μ. For this purpose, the hazard curve at point **a** in Fig. 23 is replaced with the median curve. All of the hazard curves with $\varepsilon_\mu > 0$ are given zero weight. Weights of the rest are renormalized. Figs. 36 and 37 show the results for acceleration and velocity, respectively. Surprisingly, the mean values of these curves are not very much smaller than the median (and the YM-PSHA median) curve. It still gives relatively high ground motions of near 4 g and 450 cm/s at occurrence rates of 10^{-8}. This is because, again, in the averaging process, done on the linear amplitudes, the highest values (*i.e.*, the median in this case) dominate. Comparing with Figs. 24 and 25, the result of this reweighting scheme yields hazard curves higher than case j and just smaller than the median. Thus, considering Fig. 35, this reweighting is not consistent with the precarious rocks.

Anderson and Brune [13] have suggested that the aleatory uncertainty is seriously overestimated in the ground-motion prediction equations used here, in YM-PSHA, and in PSHA in general. They propose that the reason is that, in the development of the ground-motion prediction equations, an ergodic assumption is erroneously made. The ergodic assumption arises because the distribution of uncertainties in the ground-motion prediction equations is a spatial uncertainty, but as discussed in the Sec. 5.6.3, what dominates the hazard curve at low probabilities (10^{-5} or less per year in this study) is the uncertainty in the ground motion from repeated occurrences of earthquakes on the same source, a temporal uncertainty. Because both the physics of the source and the wave-propagation effects from the source to the station are much more similar in repeated earthquakes, Anderson and Brune [13] hypothesize that the correct value of σ_A should be much smaller than what is found by the regression methods to find the parameters for ground-motion prediction equations.

The effect of the ergodic assumption has been illustrated implicitly in this study. The range of its impact on individual hazard curves is illustrated in Figs.28-31. The curves for $\sigma_A = 0.01$ illustrate the maximum reduction to an individual hazard curve that could result from a reevaluation of σ_A by removing the ergodic assumption. Figs. 32 and 33 indicate that if that reduction is not accompanied by a decrease in the epistemic uncertainty, then the net effect on the mean hazard curve may not be substantial enough to lower the mean hazard at low probability levels into a range of peak accelerations and velocities that is expected based on past experiences.

A conclusion from this study is that the median-ground motion model is inconsistent with the existence of the 4 precarious rocks on Yucca Mountain included in this analysis. This may be a result of both inflated median ground motions and inflated aleatory uncertainties. The cases most consistent with the precarious rocks have the lowest medians and aleatory uncertainties. Separating these two parameters may be quite difficult.

Before pursuing that line of experimentation, however, it would be appropriate to explore more thoroughly the input seismicity models and their impact on the precarious rocks. The particular model here has a diffuse seismicity zone that introduces earthquakes with magnitudes 5.0 to 6.5 which contribute to the hazard at Yucca Mountain, at the rates given by Table 4. These rates are based on the mean rate of earthquakes of this size over a much larger area. The rate given by Table 4 for earthquakes within 10 km (62.3 earthquakes per 10^5 years, extrapolated using a b-value of 1.0, predicts 0.6 earthquakes per year with M>2. However, the Yucca Mountain block itself has been much less active, as no earthquakes with M>2 has occurred within 10 km since instrumental monitoring started (D. von Seggern, pers. comm.). If this trend persists, then the rates of local earthquakes would converge to the rates on the individual faults only. Thus an interesting parallel set of calculations would be one in which only the local faults are included.

6.0 Assumptions

Precarious rocks are strong-motion seismoscopes that have been in place for thousands of years, and thus they can provide important information on ground motion and seismic hazard from large earthquakes over long periods of time. Therefore, the level of shaking necessary to topple a precariously balanced rock (through rigid-body rocking motion) can provide constraints on ground motion at that site for seismic shaking in the past. The main assumptions are that the precariously balanced rocks (1) have been in the current position for thousands of years, (2) they undergo rocking motion (Fig. 2) during strong ground shaking, and (3) there is no sliding on the pedestal during earthquakes.

For the coherence study it is assumed that the S-P time can be adequately approximated by earthquake-station distance divided by 8, which assumes that the earth is approximately a Poisson solid (Poisson's ratio =0.25). It is also assumed that the P and S waves can be appropriately aligned using cross-correlation. Spurious, large-time cross-correlation lags have been removed by only allowing lags between receivers that would be expected for those receivers known interstation distance and an assumed velocity of 1000 m/s, which appeared adequate based on review of several record sections.

7.0 Discussions and Conclusions

In summary, the results of the shake-table experiments (Q data) have been compared with numerical overturning predictions (non-Q data). Numerical predictions for toppling of large objects with simple contact conditions (*e.g.*, I-beams with sharp basal edges) agree well with shake-table results. The numerical model slightly underpredicts the PGA which will cause overturning of small rectangular blocks. It overpredicts the overturning PGA for asymmetric granite boulders with complex basal contact conditions. In general the results confirm the approximate predictions of several previous studies by authors.

Field testing of several rocks at Yucca Mountain (Q data) has approximately confirmed the preliminary results from previous studies, suggesting that the YM-PSHA predictions are too high.

Study of the coherence of wavefields in the ESF has provided results which will be very important in design of the canisters distribution, in particular preliminary estimate of the wavelengths at which the wavefields become incoherent. None of the observations or analyses, coherence or cross-correlation, have indicated the existence of lens-like inhomogeneities which could lead to extreme lens-like focusing, with consequent extremely high ground motions.

A conclusion from the PSHA study (non-Q data) is that the median ground-motion model is inconsistent with the existence of the 4 precarious rocks on Yucca Mountain included in this analysis. This may be a result of both inflated median ground motions and inflated aleatory uncertainties. The cases most consistent with the precarious rocks have the lowest medians and aleatory uncertainties. Separating these two parameters may be quite difficult.

7.1 Conclusions Based on Quality Affecting Data

Quasi-static toppling accelerations measured in field tests in conjunction with the shake-table experiment results can provide constraints on the maximum ground accelerations at the location of precarious rocks. The quasi-static toppling accelerations for the tested rocks range between 0.07 g and 0.38 g. In Table 1, the ‘*’ next to the rock ‘Doozy’ indicates uncertainty in this measurement. Estimates of the dynamic toppling accelerations (0.09g to 0.49g) listed in Table 1 are 30% higher than the quasi-static toppling accelerations. This rough estimate is based on the results of Anooshehpoor *et al.* [2, 7]. These approximate values only provide *upper limits* for ground motion at the location of the rocks. However, because of the small number of the tested rocks, the statistical uncertainties are large.

7.2 Corroboration Including Unqualified Data

In this section the data from shake-table experiments and field tests are Q-data. However, Purvance [9] regression curves, which are non-Q, are included for corroborative purposes only.

7.2.1 COMPARISON METHODOLOGY AND DISCUSSIONS (REPEAT OF SECTION 5.3.2)

Purvance [9] provides relations for the high-frequency ground motion amplitude (PGA) associated with overturning at a specified probability as a function of the low-frequency ground motion amplitude (PGV/PGA) and the object’s geometrical parameters (*e.g.*, height and slenderness). Both the PGV/PGA and PGA of each overturning occurrence of all objects on the shake table have been catalogued. In order to compare the overturning formulation with the experimental observations, one must first estimate the overturning probability corresponding to a specified number of overturning occurrences. In other word, the number of overturning occurrences of a specified object on the shake table does not correspond directly to an overturning probability. The corresponding overturning probability has been estimated by querying a set of numerically synthesized overturning responses of rectangular blocks exposed to a suite of ground motions. Using the relations in Purvance [8], one can calculate the overturning probability corresponding to a specified number of overturning occurrences. For instance, Fig. 5 shows the distribution of predicted overturning probabilities associated with the first overturning occurrence obtained from these numerical simulations. As a result, subsequent analyses utilize a value of 16% for the overturning probability to predict the first overturning occurrence observed in the shake table experiments. In the subsections below we first compare the overturning responses of rectangular blocks that are identical in size, but differ in composition in order to investigate the effects of material type on overturning response. In the following plots, the red symbols indicate the PGV/PGA and PGA corresponding to the first overturning occurrence of the specified object on the shake table, black lines represent the numerical predictions of Purvance [9], and the blue lines are the 5% and 95% prediction intervals.

7.2.1.1 Effects of Material Type on Damping

The precarious rock methodology is based on the assumption that balanced rocks experience only rocking motion during earthquakes. In our analysis, we assume that during impact (transition from one rocking point to the other) there is no bouncing or sliding *(perfectly inelastic* impact). Therefore, the angular momentum before and after the impact, about the point of impact is conserved. (There is no change in the total external torque on the block because the impact force is applied at the point about which the torque is calculated [7]) However, because of the inelastic impact, the total energy is not conserved (loss due to deformations at the point of impact, including heat, sound, etc.). The energy loss results in a lower angular velocity after the impact. The ratio of the angular velocities before and after the impact is defined as the coefficient of restitution η:

$$\eta \equiv \frac{\dot{\theta}_2}{\dot{\theta}_1},$$

where $\dot{\theta}_1$ and $\dot{\theta}_2$ are the angular velocities before and after the impact, respectively. The value of η is less than unity. Based on the analytical solutions for two-dimensional rocking motion of a rigid block developed, the energy loss is a function of the aspect ratio (width/height). That is, the more slender the blocks are, the less energy they lose after an impact. For a rectangular block the coefficient of restitution takes the simple form

$$\eta = 1 - \frac{3}{2}\sin^2\alpha,$$

where, α is the angle between the vertical and the line through the center of mass and the rocking point (Fig. 1).

Theoretically, damping of a rigid block depends only on geometry. However, in practice the material can affect damping. In order to investigate variations in overturning due to material damping, blocks AL1 and AL2 and their exact wooden replicas W1 and W2, respectively, were tested on the shake table. The waveforms listed in section 5.3.1 were used as input to the shake table. Fig. 6 compares the numerical predictions [9] with the experimentally derived overturning. The wood (black symbols) and aluminum (red symbols) blocks overturned nearly identically. The data spread is somewhat beyond the prediction intervals estimated by Purvance

[9]. Note that these blocks are well outside the parameter space investigated in that study, though. It is also possible that such small objects may have been influenced by the basal contact conditions (*e.g.*, grip tape elasticity).

7.2.1.2 Small Rectangular Blocks

In Fig. 7, shake-table results for overturning of six small rectangular blocks are compared with the numerical predictions [9]. These blocks consisted of aluminum blocks, AL1 and AL2, granite block G, and wooden blocks W1, W2 and W3. Blocks W1, W2 and W3 are the exact replicas of AL1, AL2, and G, respectively. These objects were subjected to the waveforms listed in section 5.3.1. The formulation of Purvance [9] predicts the overturning behaviors of blocks G and W3 adequately, but slightly underestimates the responses of blocks AL1, AL2 and their wooden replicas. The discrepancies could be attributed to the basal contact conditions and the frequency content of the input motions.

.

7.2.1.3 Steel I-Beams

Tall, steel I-beams have simple basal contact conditions and shapes. Also, by adding lead weights to I-beams, their geometrical parameters α, *R*, and the moment of inertia may be altered. For instance, certain configurations allow us to model symmetric and asymmetric homogeneous objects that are significantly taller than the steel I-beams by changing the location of the center of mass. Fig. 8 compares the numerical predictions [9] (black lines) with I-beam overturning data from the shake table experiments. The level of agreement is striking for both symmetric and asymmetric I-beams. Most of the data also fall within the prediction intervals, suggesting that the Purvance [9] predicts an appropriate range of realistic behaviors. Again, the waveforms listed in section 5.3.1 were used as input to the shake table.

7.2.1.4 Granite Boulders

Along with the rectangular blocks and I-beams, three granite boulders were selected to represent geometrically complex precariously balanced rocks found in seismically active regions. Fig. 9 compares the numerical predictions [9] (black lines) with the overturning data from the shake table experiments. The numerical model systematically overpredicts the PGA required for overturning. The trend of records with low PGV/PGA requiring larger PGA to overturn persists, though. These findings can be attributed to the fact that the numerical model utilized in [9] is based on objects rocking about two basal contacts corresponding to the geometric extent of the object (Fig. 10a). As the object tilts during rocking, the restoring force decreases nearly linearly with inclination (Fig. 10b). Objects that rock about multiple basal rocking points (Fig. 11a) produce more complex restoring force versus inclination responses (Fig. 11b) wherein the peak restoring force may be significantly reduced when compared to the simple model used in the numerical simulations (Fig. 10). We have developed a methodology to accurately measure the restoring force ($F = mg\tan(\alpha - \theta)$, where m is the mass, g gravitational acceleration, and θ the inclination) as a function of inclination via a winch, load cell, and inclinometer (Fig. 12). The object in question is pulled horizontally until the restoring force decreases approximately linearly with angle of inclination. Such measurements of precariously balanced rocks are feasible in the field provided special care is taken to avoid overturning the rock so that the rock can be returned to its original position. These data are processed via parameterizing the nearly linear decay, allowing one to obtain an estimate of the mass and slenderness associated with the final rocking point. The force is then normalized via the product of the mass and acceleration of gravity, and the arctangent of the peak normalized force is used as the reduced slenderness in the formulation of Purvance [9]. Fig. 13 shows the restoring force versus inclination curves for the three boulders tested in these shake table experiments. The peak normalized forces suggest that the slenderness may be reduced by 20% - 30% due to basal roughness. The resulting overturning predictions are shown in Fig. 14 (black lines) relative to those that do not account for the basal roughness as explained above (green lines). This methodology is both relatively straightforward to implement in the field and effective at parameterizing the overturning responses of objects with complex basal contact conditions.

- A good level of agreement has been obtained between input and measured accelerograms in the experiments.
- Small wooden and aluminum block overturn nearly identically.
- Numerical predictions [9] of overturning of large objects with simple contact conditions (e.g., I-beams with sharp basal edges) agree well with the shake-table results. Thus experimentally observed overturning occurrence depend both on the low- and high-frequency ground motion amplitudes.
- Purvance [9] overpredicts the overturning PGA for boulders with complex basal contact conditions.
- Force versus inclination measurements provide a robust method to adjust the formulation of Purvance [9] to account for complex basal contact.

7.2.2 COHERENCE (REPEAT OF SECTION 5.5.6)

Both the cross-correlations and coherencies indicate the ground motions lose coherence at distances on the order of 100 – 200 m and frequencies higher than 1 Hz within the ESF tunnel. Coherence and cross-correlation values are no different from random seismograms in this distance-frequency region, except that cross-correlations were predominantly positive instead of only 50% positive as would be expected for random events. At distances less than about 200 m, coherency values and correlations are significant to about 10 Hz for both P and S waves, with P waves having higher coherencies and cross-correlations than S-waves. Correlations and coherencies are excellent at frequencies less than 1 Hz for all distances, except for S-waves, which only display moderate values at distances beyond 300 m. These results indicate that the tunnel area exhibits strong scattering, especially of S-wave energy, even over distances as short as 200 m and for frequencies as low as 1-1.5 Hz.

This present scoping study gives preliminary results of coherencies and ground motion correlations at 100 and 60 m inter-station distances for about 300 mostly small (less than magnitude 2) earthquakes. A wide range of correlation distances need to be examined with a sufficient number of events to obtain a reliable estimate of real ground motions within the ESF tunnel. Eventually, 10 m spacing would be desirable for direct empirical estimates of variations in ground motion between nuclear waste storage casks. The lack of events above magnitude 3 or 4 within 100 km of the array in the present study period prevents useful and trust worthy extrapolations to large magnitude events that could occur on local and region faults in the area such as on the Furnace Creek fault system. Time is the only way to increase earthquake azimuthal, distance, and magnitude distribution. Events with magnitudes 4 or larger have occurred in the local area, but their recurrence is such that on the order of a decade of data will be required to get a sufficient distribution for robust statements of coherency to be made.

The two computed quantities in this discussion, coherence and cross-correlation, contribute to an understanding of ground motion in different ways. Coherence is an empirical measure of the variation of the wavefield as it propagates along the array. These variations can be due to structural variations such as scattering in the local environment or to variations along the wavefront that have propagated directly from the source or from structural effects along the path. Azimuthal, distance and magnitude variations in coherence may be useful in separating local from extra-local sources of decoherence in the wavefield. In addition, transfer functions from one array point to another in the tunnel would allow simulations of large magnitude events and their resulting expected ground motions. This, of course, necessitates at least moderate magnitude events to have been recorded for more reliable extrapolation.

Cross-correlations, on the other hand, empirically measure ground motion variations between two points at the same time including phase and arrival delays. A half-cycle delay in perfectly coherent wavefields will result in a potentially disastrous situation of adjacent casks moving in opposite directions. Based on our present results, there are only small anticorrelations of ground motions between points; the cross-correlations display predominately positive cross-correlations. Correctly predicting the ground motions from simulated earthquakes will require careful calibration based on actual earthquake wavefield coherencies and their corresponding cross-correlated ground motions.

None of the observations or analyses, coherence or cross-correlation, have indicated the existence of lens-like inhomogeneities which could lead to extreme lens-like focusing, with consequent extremely high ground motions.

7.2.3 PSHA (REPEAT OF SECTION 5.6.5)

It is difficult to know how to estimate the magnitude of the epistemic uncertainties, σ_μ and σ_σ. One approach applied with judgment by the ground motion panel in YM-PSHA deserves some discussion. The ground-motion panel was asked to estimate point values of the ground-motion parameters for a large number of combinations of magnitude and distance. These point values were subsequently fit with Equation 1, as mentioned above. In developing the point values, the modelers considered several “advocacy models”, which were ground-motion prediction equations developed previously (but not necessarily published). These may have been modified for the hard-rock site condition at Yucca Mountain. Some were developed primarily from fitting data but some were developed from synthetic seismograms. Point values can be estimated by taking a weighted average of the median values of the advocacy models. Then one simple way to estimate σ_μ and σ_σ is to look at the standard deviation of the median ground motions and standard deviations of the advocacy models. In developing his estimate of σ_μ, Anderson considered that method likely to underestimate the complete uncertainty, since none of the models were constrained by observations in the near-field of large normal-faulting earthquakes, the type expected in the vicinity of Yucca Mountain. Furthermore, he wanted to be sure that, on the low side, the models would have a non-negligible probability that the median of the distribution would be consistent with the emerging data on precarious rocks. This led to his estimate of σ_μ that was larger than the other models.

One question that has come up is what would be the impact, considering that line of reasoning, if Anderson had provided an asymmetrical distribution for μ instead of a normal distribution. That is easily tested through development of a reweighting scheme that approximates the effect of a different, non-Gaussian distribution of ε_μ and ε_σ. Table 6 presents a reweighting scheme that is strongly skewed to favor non-positive values of ε_μ. For this purpose, the hazard curve at point **a** in Fig. 23 is replaced with the median curve. All of the hazard curves with $\varepsilon_\mu > 0$ are given zero weight. Weights of the rest are renormalized. Figs. 36 and 37 show the results for acceleration and velocity, respectively. Surprisingly, the mean values of these curves are not very much smaller than the median (and the YM-PSHA median) curve. It still gives relatively high ground motions of near 4 g and 450 cm/s at occurrence rates of 10^{-8}. This is because, again, in the averaging process, done on the linear amplitudes, the highest values (*i.e.*, the median in this case) dominate. Comparing with Figs. 24 and 25, the result of this reweighting scheme yields hazard curves higher than case j and just smaller than the median. Thus, considering Fig. 35, this reweighting is not consistent with the precarious rocks.

Anderson and Brune [13] have suggested that the aleatory uncertainty is seriously overestimated in the ground-motion prediction equations used here, in YM-PSHA, and in PSHA in general. They propose that the reason is that, in the development of the ground-motion prediction equations, an ergodic assumption is erroneously made. The ergodic assumption arises because the distribution of uncertainties in the ground-motion prediction equations is a spatial uncertainty, but as discussed in the Sec. 5.6.3, what dominates the hazard curve at low probabilities (10^{-5} per year in this study) is the uncertainty in the ground motion from repeated occurrences of earthquakes on the same source, a temporal uncertainty. Because both the physics of the source and the wave-propagation effects from the source to the station are much more similar in repeated earthquakes, Anderson and Brune [13] hypothesize that the correct value of σ_A should be much smaller than what is found by the regression methods to find the parameters for ground-motion prediction equations.

The effect of the ergodic assumption has been illustrated implicitly in this study. The range of its impact on individual hazard curves is illustrated in Figs.28-31. The curves for $\sigma_A = 0.01$ illustrate the maximum reduction to an individual hazard curve that could result from a reevaluation of σ_A by removing the ergodic assumption. Figs. 32 and 33 indicate that if that reduction is not accompanied by a decrease in the epistemic uncertainty, then the net effect on the mean hazard curve may not be substantial enough to lower the mean hazard at low probability levels into a range of peak accelerations and velocities that is expected based on past experiences.

A conclusion from this study is that the median-ground motion model is inconsistent with the existence of the 4 precarious rocks on Yucca Mountain included in this analysis. This may be a result of both inflated median ground motions and inflated aleatory uncertainties. The cases most consistent with the precarious rocks have the lowest medians and aleatory uncertainties. Separating these two parameters may be quite difficult.

Before pursuing that line of experimentation, however, it would be appropriate to explore more thoroughly the input seismicity models and their impact on the precarious rocks. The particular model here has a diffuse seismicity zone that introduces earthquakes with magnitudes 5.0 to 6.5 which contribute to the hazard at Yucca Mountain, at the rates given by Table 4. These rates are based on the mean rate of earthquakes of this size over a much larger area. The rate given by Table 4 for earthquakes within 10 km (62.3 earthquakes per 10^5 years, extrapolated using a b-value of 1.0, predicts 0.6 earthquakes per year with M>2. However, the Yucca Mountain block itself has been much less active, as no earthquakes with M>2 has occurred within 10 km since instrumental monitoring started. If this trend persists, then the rates of local earthquakes would converge to the rates on the individual faults only. Thus an interesting parallel set of calculations would be one in which only the local faults are included.

8.0 Inputs and References

8.1 Data ID Numbers for Figures and Tables

Data ID for figures and tables are listed in the following table.

Figure	Data ID Number (DID)	File Name
3	020RA.003	Fig-3
4	020RA.001	Fig-4
5	020RA.003	Fig-5
6	020RA.003	Fig-6
7	020RA.003	Fig-7
8	020RA.003	Fig-8
9	020RA.003	Fig-9
13	020RA.001	Fig-13
14	020RA.003	Fig-14
17	020RA.002	Fig-17
18	020RA.002	Fig-18
19	020RA.002	Fig-19
23	020RA.004	Fig-23
24	020RA.004	Fig-24
25	020RA.004	Fig-25
26	020RA.004	Fig-26
27	020RA.004	Fig-27
28	020RA.004	Fig-28
29	020RA.004	Fig-29
30	020RA.004	Fig-30
31	020RA.004	Fig-31
32	020RA.004	Fig-32
33	020RA.004	Fig-33
34	020RA.004	Fig-34
35	020RA.004	Fig-35
36	020RA.004	Fig-36
37	020RA.004	Fig-37
Table		
1	020RA.001	Table-1
2	020RA.001	Table-2
4	020RA.004	Table-4
5	020RA.004	Table-5
6	020RA.004	Table-6

8.2 References

1 Bierman, P.R., C.A. Massey, and A.R. Gillespie (1993). Erosion rate and exposure age of granite landforms estimated with cosmogenic ^{36}Cl, *Geol. Soc. Am.*, **25**, p 141.

2 Anooshehpoor, A., J. N. Brune, and D. H. Von Seggern (2002), Constraints on ground motion at Yucca Mountain provided by precarious rocks, DOE/NSHE Cooperative Agreement Number DE-FC08-98NV12081, Report TR-02-001.

3 BSC (2004). Technical Basis Document No. 14: Low Probability Seismic Events, Revision 1, OCRWM DCN #43222, Bechtel SAIC Company, LLC, Las Vegas, 306 pages.

4 YM PSHA: Civilian Radioactive Waste Management System Management and Operating Contractor (1998). Probabilistic seismic hazard analyses for fault displacement and vibratory ground motion at Yucca Mountain, Nevada, Wong, I. G. and J. C. Stepp, report coordinators, U. S. Department of Energy, Oakland, California.

5 Brune, J. N., and J. W. Whitney (2000). Precarious rocks and seismic shaking at Yucca Mountain, Nevada, *USGS Digital Data Series*, **058,** Chapter M.

6 Shi, B., A. Anooshehpoor, Y. Zeng, and J.N. Brune (1996). Rocking and overturning of precariously balanced rocks by earthquakes, *Bull. Seism. Soc. Amer.*, **86**, 1364-1371.

7 Anooshehpoor, A., J. N. Brune and Y. Zeng (2004). Methodology for obtaining constraints on ground motion from precariously balanced rocks, *Bull. Seism. Soc. Am*., **94**, 285-303.

8 Anooshehpoor, A. and J. N. Brune (2002). Verification of precarious rock methodology using shake table tests of rock models, *Soil Dyn. Earthquake Eng. J*., **22**, 917-922.

9 Purvance, M.D. (2005). Overturning of slender blocks: numerical investigation and application to precariously balanced rocks in southern California, *PhD Dissertation*, University of Nevada, Reno.

10 Stepp, J. C., I. Wong, J. Whitney, R. Quittmeyer, N. Abrahamson, G. Toro, R. Youngs, K. Coppersmith, J. Savy, T. Sullivan, and Yucca Mountain PSHA project Members (2001). Probabilistic seismic hazard analyses for fault displacement and ground motions at Yucca Mountain, Nevada, *Earthquake Spectra*, **17**, 113-152.

11 Anderson, J. G., and J. N. Brune (1999). Methodology for using precarious rocks in Nevada to test seismic hazard models, *Bull. Seism. Soc. Am*., **89**, 456-467.

12 Anderson, J. G. and M. D. Trifunac (1978). Uniform risk functionals for characterization of strong ground motion, *Bull. Seism. Soc. Am.,* **68**, 205-218.

13 Anderson, J. G., and J. N. Brune (1999). Probabilistic seismic hazard analysis without the ergodic assumption, *Seism. Res. Lett*., **70**, 19-28.

14 Bell, J.W., J.N. Brune, T. Liu, M. Zerda, and J.C. Yount (1998). Dating the precariously balanced rocks in seismically active parts of California and Nevada, *Geology*, **26**, 495-498.

9.0 Software

The following computer programs are used in this task and controlled according to QAP-3.2: *Software Management.*

Program Name	STN	Purpose	Computer
SAC	10085-00.46	process and analyze seismograms	Sun O/S 2.8

Table 1: The physical characteristics of a subset of the objects used in shake-table experiments are listed here. Figure 2-a show most of these object on the shake table, before an experiment (DID 020RA.001, table-1).

Object ID	**α_1 (rad)**	**α_2 (rad)**	**R_1 (cm)**	**R_2 (cm)**
AL1	0.31	0.31	7.9	7.9
AL2	0.14	0.14	22.9	22.9
G	0.37	0.37	9.6	9.6
W1	0.31	0.31	7.9	7.9
W2	0.14	0.14	22.9	22.9
W3	0.37	0.37	9.6	9.6
IB0	0.29	0.29	63.7	63.7
IB1	0.19	0.31	73.7	75.6
IB2	0.21	0.21	88.0	88.0
IB4	0.29	0.29	63.7	63.7
D	0.24	0.50	48.3	50.8
E	0.35	0.52	38.1	35.4
K	0.30	0.42	49.5	47.0
CT1	0.27	0.27	35.5	35.5
CT2	0.33	0.33	29.8	29.8

Table 2: Locations of the precarious rocks on Yucca Mountain crest and Solitario Canyon tested in this study. These points are chosen for seismic hazard analyses (DID 020RA.001, table-2).

Site/Rock ID	**Site/Rock Nickname**	**WGS 84 Locations**		**Quasi-Static Toppling Accel. (g)**	**Measured Alpha (rad)**	**Dynamic Toppling Accel. (g)**	**Azimuth (deg)**
		Lat	**Lon**				
	PSHA	36.8444	-116.4622				
92JBNC01	Doozy	36.85278	-116.46678	0.07*		0.09*	225
93JB8T02	Fluffy	36.80524	-116.47682	0.19	0.30	0.25, 0.39	98
92JB8T02	Red Eye	36.81464	-116.48969	0.19		0.25	0
YMSESept02	WALW	36.79925	-116.45851	0.14, 0.38		0.18, 0.49	115, 295
93RCSC59	Tripod	36.83018	-116.47085		0.21, 0.32	0.27, 0.42	65, 245

*Indicates lack of confidence in this value as the rock's true quasi-static toppling acceleration. Due to safety precautions at the NTS, the experiment was terminated after the quasi-static force reached the first maximum value. Normally, to make sure that this not a *local* maximum, the rock is tilted further.

Table 3: The approximate dates for each layout and phase. This table is non-Q and included or information only (UCCSN- UNR-085-v1).

Spacing (m)	Component	Dates	# events
100	Vertical	June 2005 – Nov 2005	75
100	Horizontal	Nov 2005 – Feb 2006	124
60	Vertical	Mar 2006 – June 2006	174
60	Horizontal	June 2006 – present	TBD

Table 4: Seismicity rates (earthquakes per 100,000 years) for the sources illustrated on Fig. 21. This table is non-Q and included or information only (DID 020RA.004, table-4).

Fault Zone	Length (km)	Magnitude					
		5.0	5.5	6.0	6.5	7.0	7.5
Solitario Canyon – Iron Ridge Fault Zone	21	0	0	0.33	0.3	0	0
Stagecoach Road- Paintbrush Canyon	35	0	0	1.08	0.45	0.02	0
Windy Wash – Fatigue Wash	24	0	0	0.66	0.59	0	0
Bare Mountain	40	0	0	0	0.48	0.48	0
Pahrump Valley	54	0	0	0	2.06	11.46	0
Yucca Flat	37	0	0	0	0	0.35	0.09
Rock Valley	63	0	0	0	0	3.23	0.54
Death Valley	311	0	0	0	0	209	100
Diffuse Zone: Distance to Site (km)							
0<R<5		7	7	2.7	0.23	0	0
5<R<10		21	18	6.0	0.38	0	0
10<R<15		35	30	9.1	0.54	0	0
15<R<20		49	41	12.3	0.69	0	0

Table 5: Relationship of the ten models to the median model. This table is non-Q and included or information only (DID 020RA.004, table-5).

Case	ε_μ (units of σ_μ)	ε_σ (units of σ_σ)	ε_μ* (units of σ_μ)	ε_σ* (units of σ_σ)	Weight
a	0.74	0	0.7	0.0	0.3031
b	0.74	1.73	0.7	1.7	0.0758
c	2.33	1.0	2.3	1.0	0.0227
d	2.33	-1.0	2.3	-1.0	0.0227
e	0.74	-1.73	0.7	-1.7	0.0758
f	-0.74	-1.73	-0.7	-1.7	0.0758
g	-2.33	-1.0	-2.3	-1.0	0.0227
h	-2.33	1.0	-2.3	1.0	0.0227
i	-0.74	1.73	-0.7	1.7	0.0758
j	-0.74	0.0	-0.7	0.0	0.3031

* As implemented in JGA program. Includes roundoff.

Table 6: Reweighted models to test an asymmetrical distribution weighted towards smaller values. This table is non-Q and included or information only (DID 020RA.004, table-6).

Case	ε_μ (units of σ_μ)	ε_σ (units of σ_σ)	ε_μ* (units of σ_μ)	ε_σ* (units of σ_σ)	Weight
median	0	0	0	0	0.3774
a	0.74	0	0.7	0.0	0
b	0.74	1.73	0.7	1.7	0
c	2.33	1.0	2.3	1.0	0
d	2.33	-1.0	2.3	-1.0	0
e	0.74	-1.73	0.7	-1.7	0
f	-0.74	-1.73	-0.7	-1.7	0.0943
g	-2.33	-1.0	-2.3	-1.0	0.0283
h	-2.33	1.0	-2.3	1.0	0.0283
i	-0.74	1.73	-0.7	1.7	0.0943
j	-0.74	0.0	-0.7	0.0	0.3774

* As implemented in JGA program. Includes roundoff.

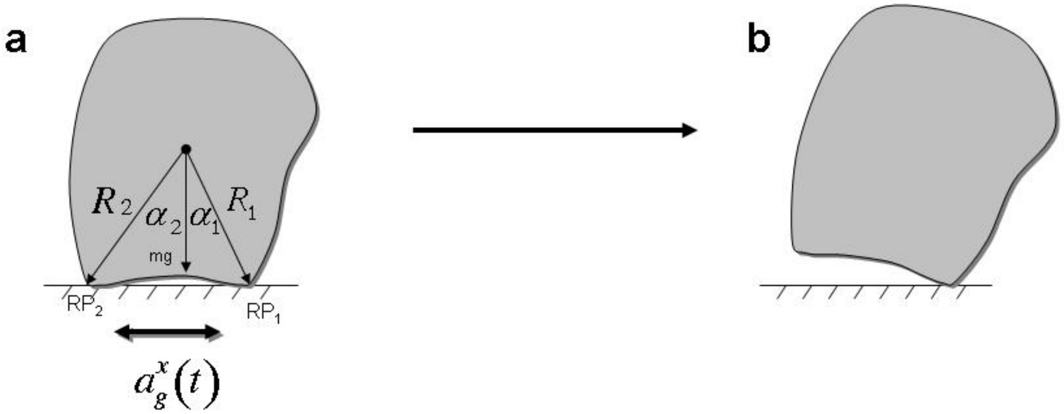

FIGURE 1: An asymmetric rock with weight *W* resting on a pedestal is free to rotate about rocking axes through rocking points *RP_1* and *RP_2*. R_1 and R_2 measure the distances from the center of mass to *RP_1* and *RP_2*, respectively. α_1 and α_2 are the angles between the vertical and R_1 and R_2, respectively.

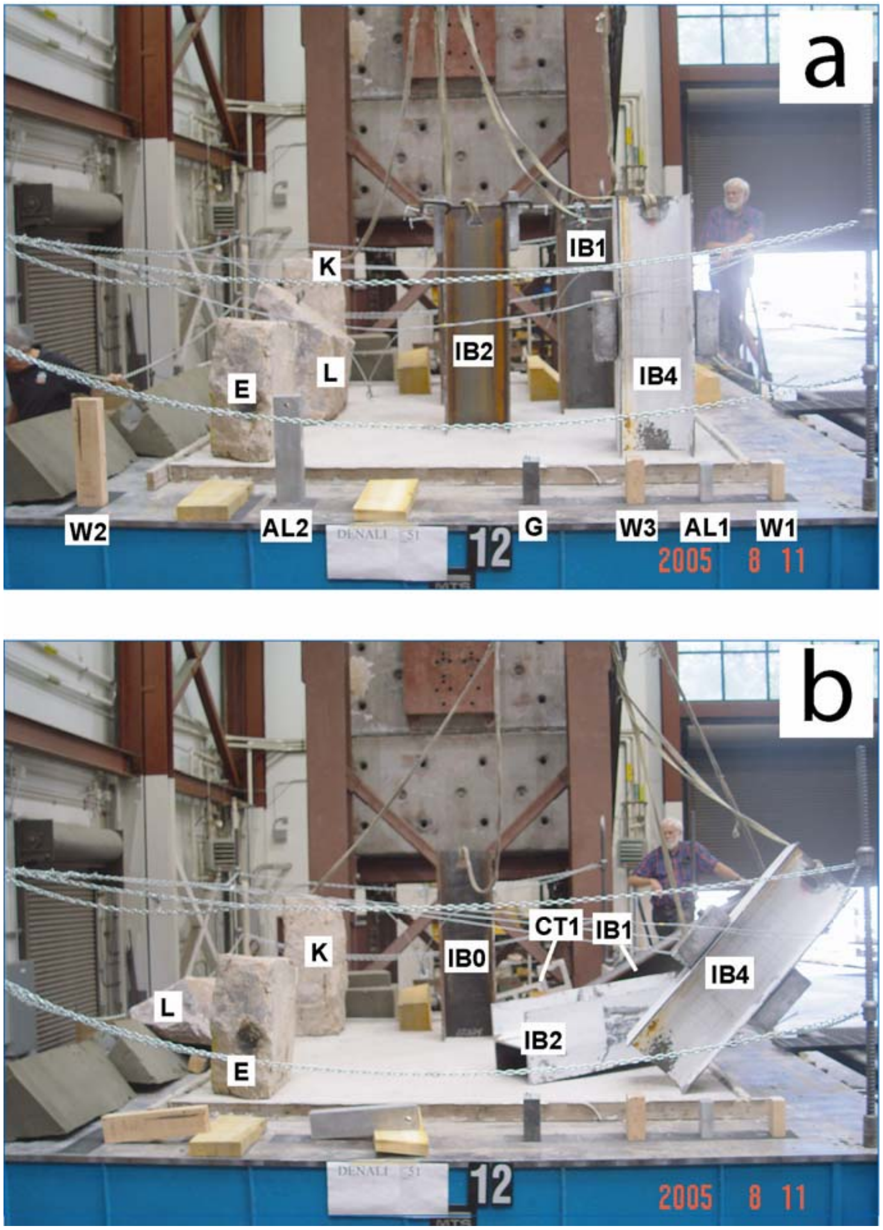

FIGURE 2: Test objects on a shake table are shown before (a) and after (b) an experiment. Notice that the objects are either resting on grip tape or a roughened concrete slab to inhibit sliding. The objects were shaken by the scaled N51E component of the 2002 Denali earthquake recorded at PS10 with PGA ~ 0.3g. Objects AL2, W2, IB1, IB2, IB4, and L overturned. The shake table motions were recorded on a Kinematics K2 accelerometer, located behind object K.

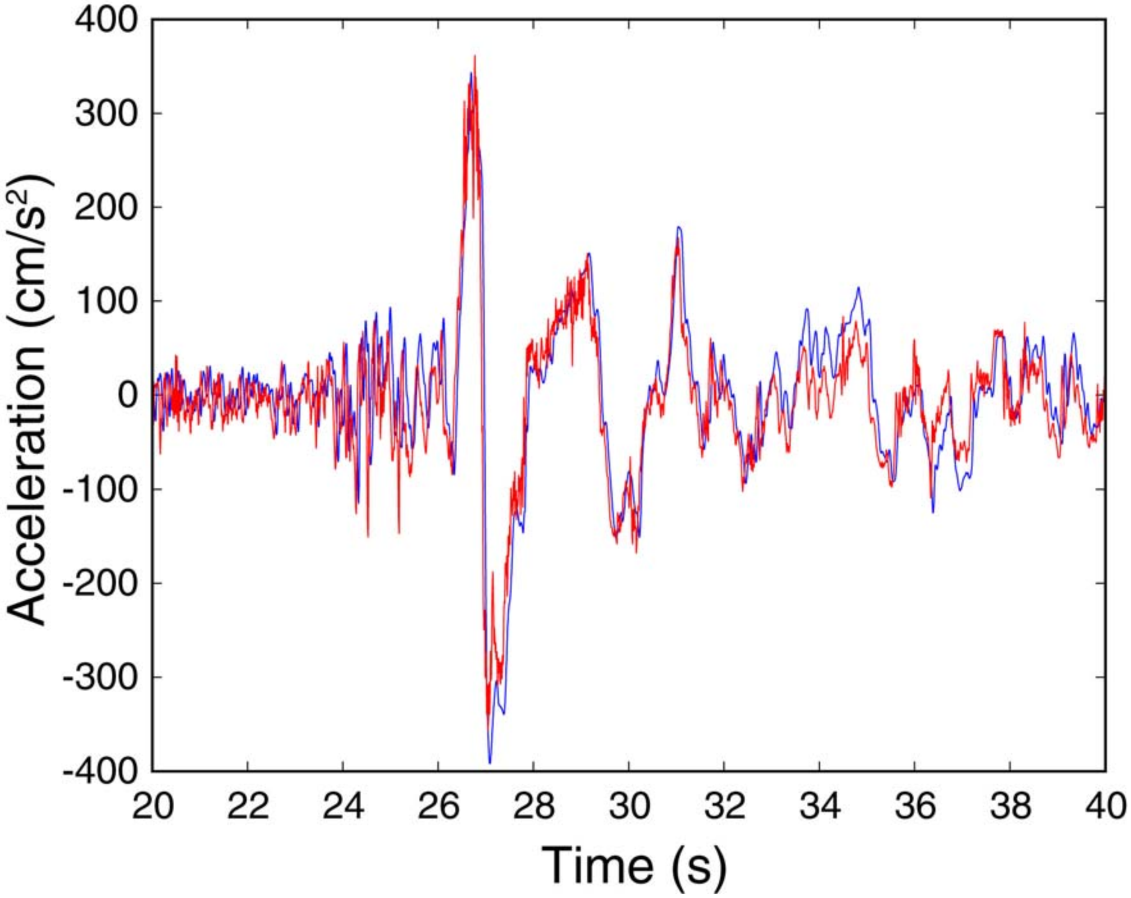

FIGURE 3: Comparison of input (blue) (source: Cosmos Virtual Data Center website http://db.cosmos-eq.org) and measured (red) accelerograms (Source DTN: 020RA.001) corresponding to the N51E component of the 2002 Denali earthquake recorded at pump station 10. The input seismogram has been scaled with PGA ~ 0.41g. This example demonstrates the level of agreement between the input and measured accelerograms. In our analyses only the measured accelerograms on the shake table are used. In this plot the blue curve is non-Q and included for corroboration only (DID 020RA.003, fig-3).

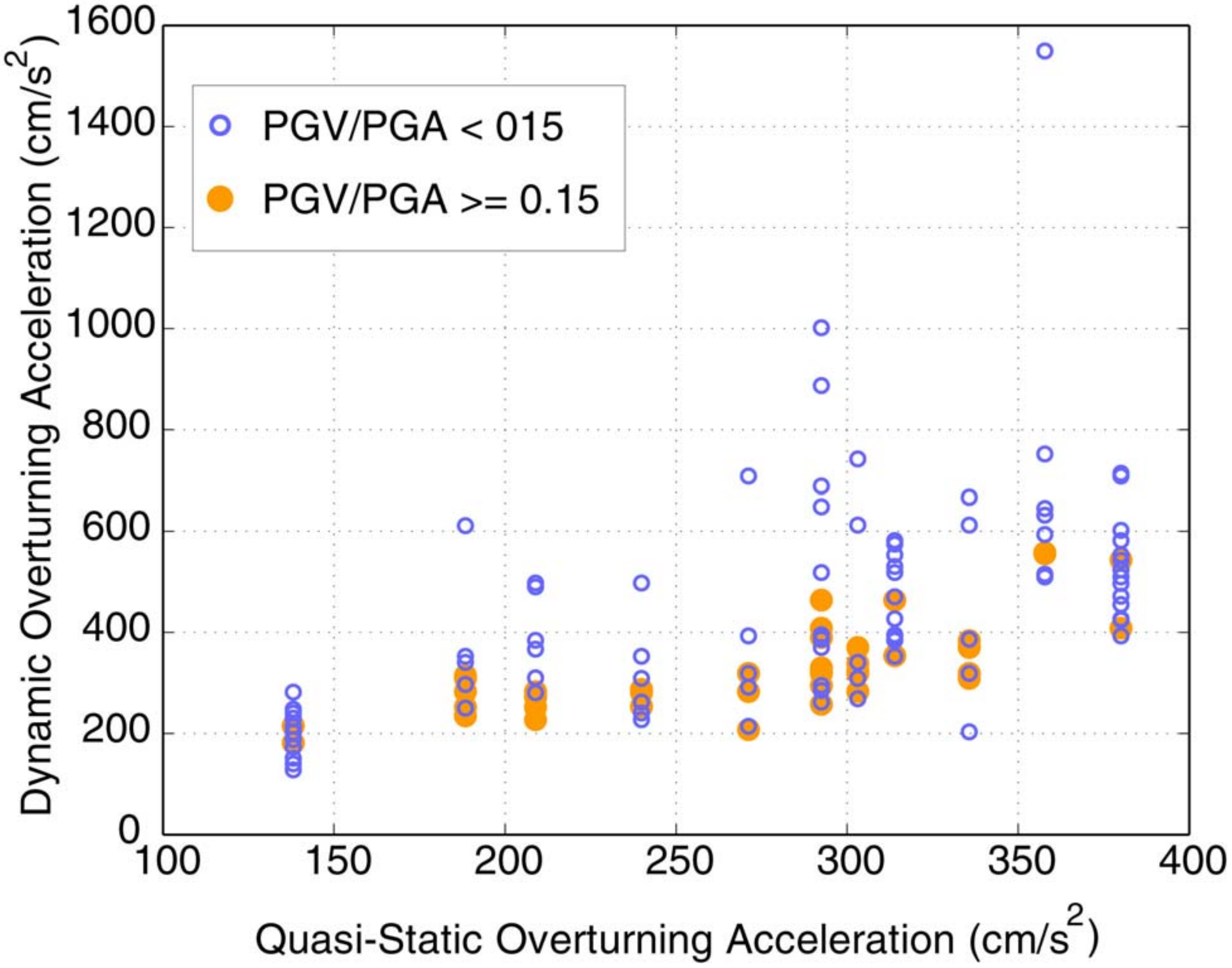

FIGURE 4: Dynamic toppling accelerations (shake-table experiment) versus quasi-static toppling accelerations for the objects listed in Table 1 are plotted here. These objects were subjected to acceleration time histories with the waveforms similar to 10 different earthquakes and synthetic seismograms. We have used two different symbols to distinguish between seismograms for which PGV/PGA values are above or below the *arbitrary* threshold of 0.15. High-frequency seismograms have generally lower PGV/PGA values than low-frequency seismograms. As this plot suggests, there is a lot more scatter in the dynamic toppling acceleration (blue open circles) when high-frequency seismograms were used in the experiment (Source DTN: 020RA.001).

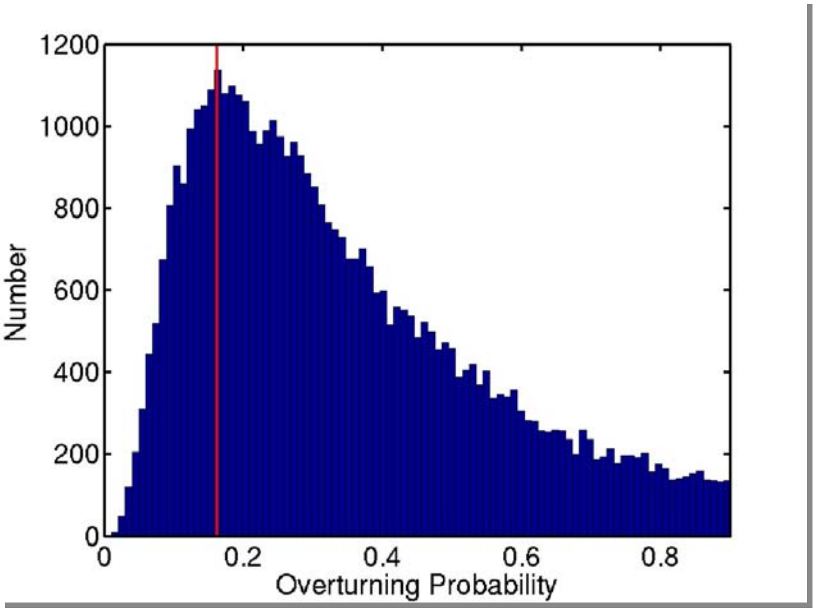

FIGURE 5: Histogram of probabilities corresponding to the first overturning occurrence from the numerical experiment. The modal value (*e.g.*, 16% overturning probability (red line)) is used for comparative purposes. This plot is non-Q and included for corroboration only (DID 020RA.003, fig-5).

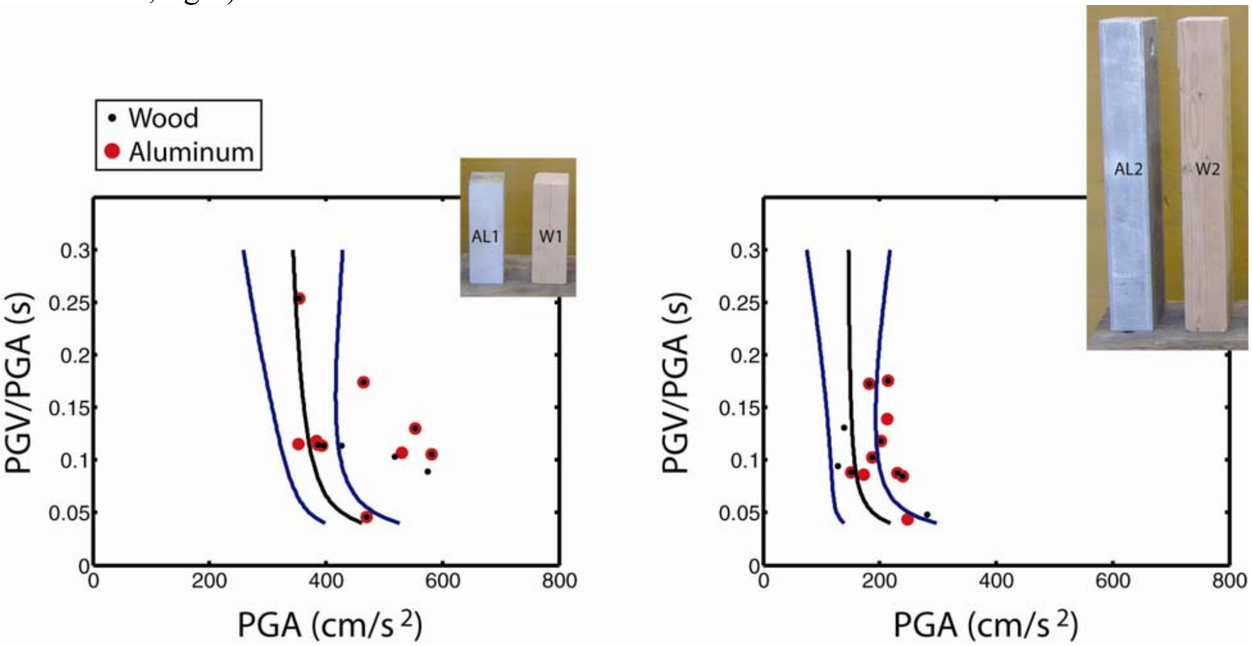

FIGURE 6: Comparison of shake-table data (black symbols, wood; red symbols, aluminum) and the numerical predictions [9] (black lines) along with the 95% prediction intervals (blue curves) for blocks AL1 and W1 (left) and AL1 and W1 (right). Pictures of the objects are inset for reference. In these plots the curves are non-Q and included for corroboration only (DID 020RA.003, fig-6).

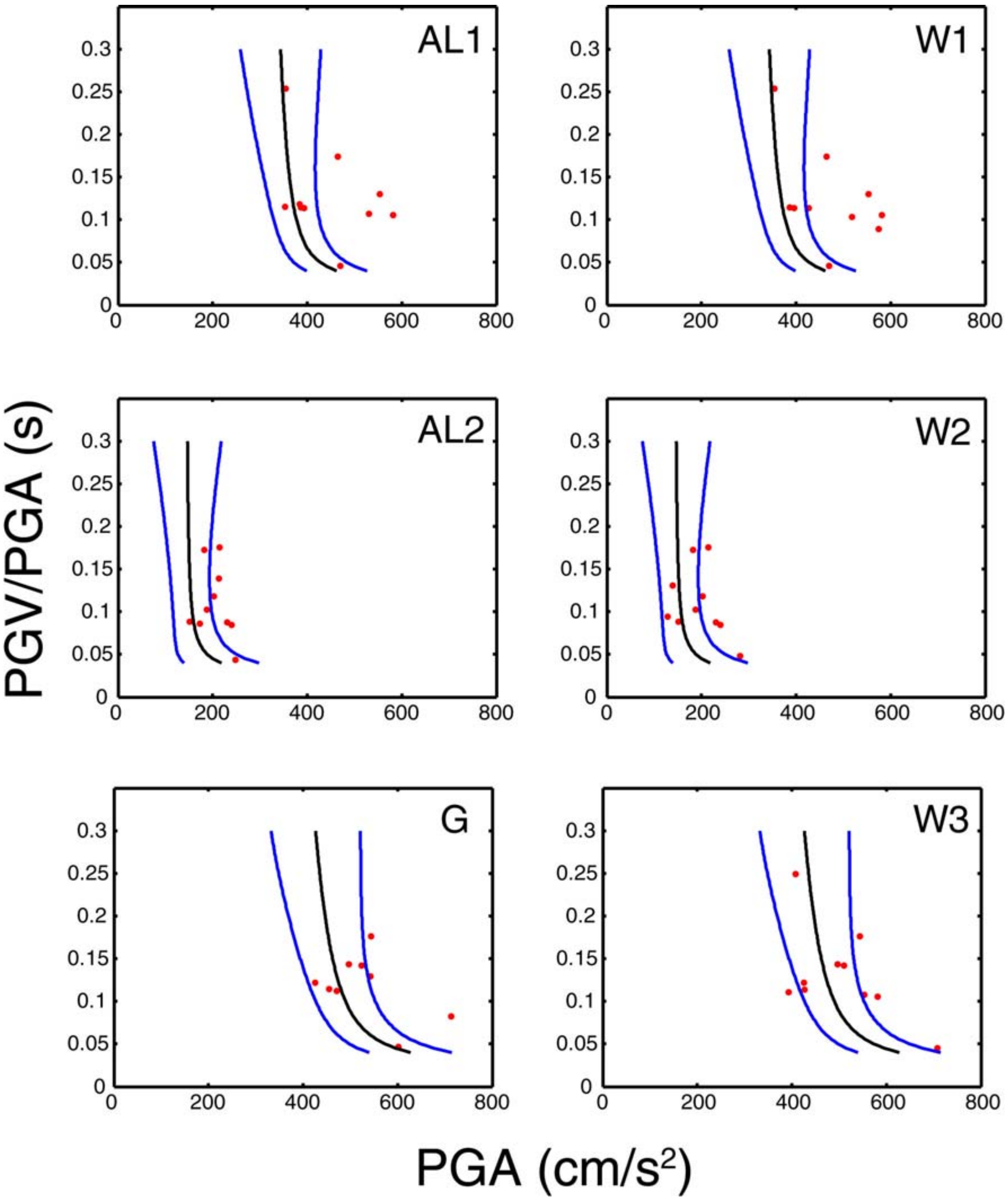

FIGURE 7: Shake table data (red symbols) (Source DTN: 020RA.001) are compared with the formulation of Purvance [9] (black lines) along with the 95% prediction intervals (blue lines) for rectangular blocks AL1, AL2, G, W1, W2 and W3. Blocks W1, W2 and W3 are the exact replicas of AL1, AL2, and G, respectively. In these plots the curves are non-Q and included for corroboration only (DID 020RA.003, fig-7).

.

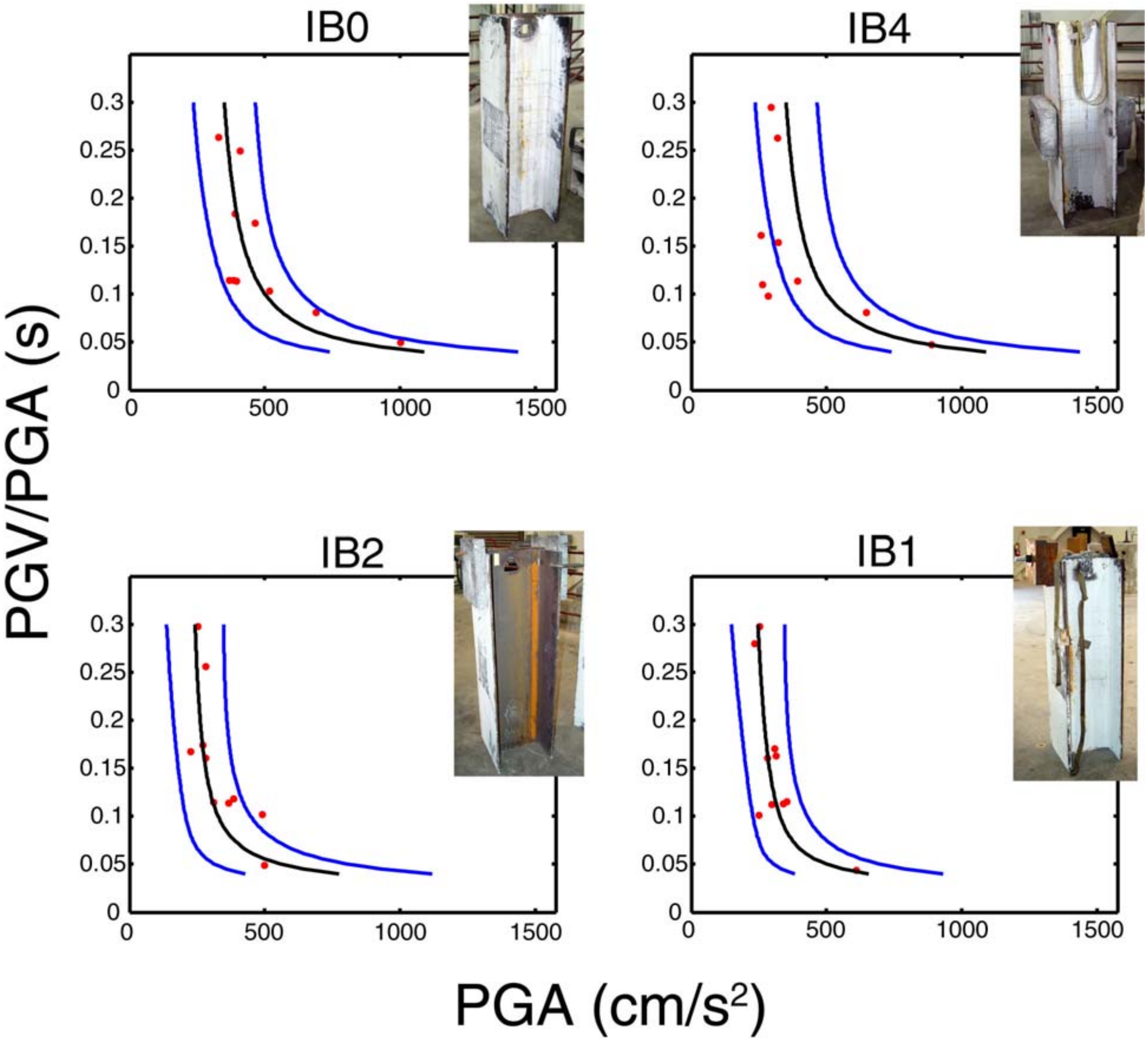

FIGURE 8: Shake table data (red symbols) (Source DTN: 020RA.001) and the formulation of Purvance [9] (black lines) along with the 95% prediction intervals (blue lines) for I-beams IB0, IB1, IB2, and IB4. IB0 and IB4 have identical α and *R*, but different moment of inertia about the rocking points. IB1 is asymmetric. In these plots the curves are non-Q and included for corroboration only (DID 020RA.003, fig-8).

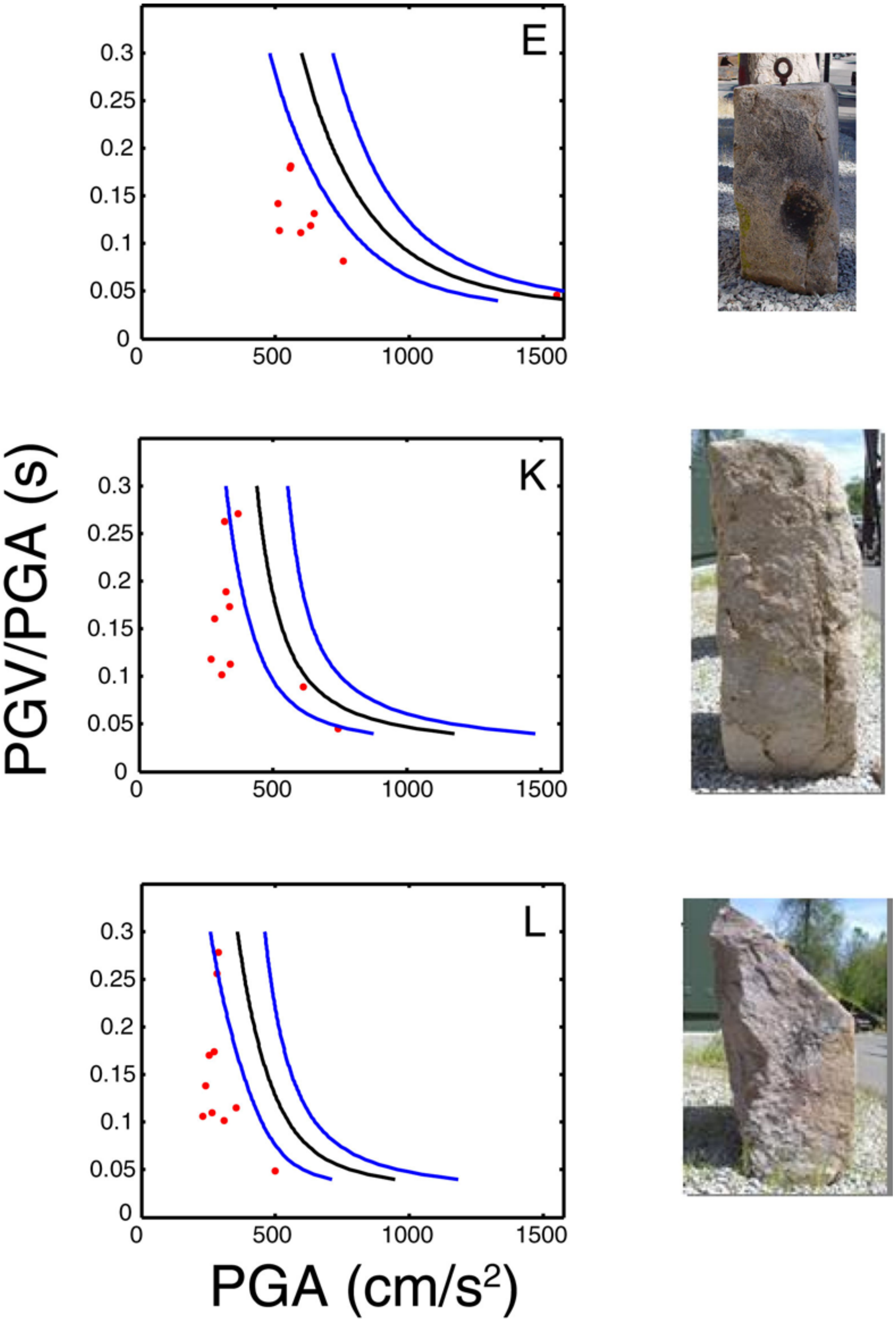

FIGURE 9: Shake table data (black symbols) and the formulation of Purvance [9] (black lines) along with the 95% prediction intervals (blue lines) for boulders L, K, and E. Pictures of the objects are inset for reference. In these plots the curves are non-Q and included for corroboration only (DID 020RA.003, fig-9).

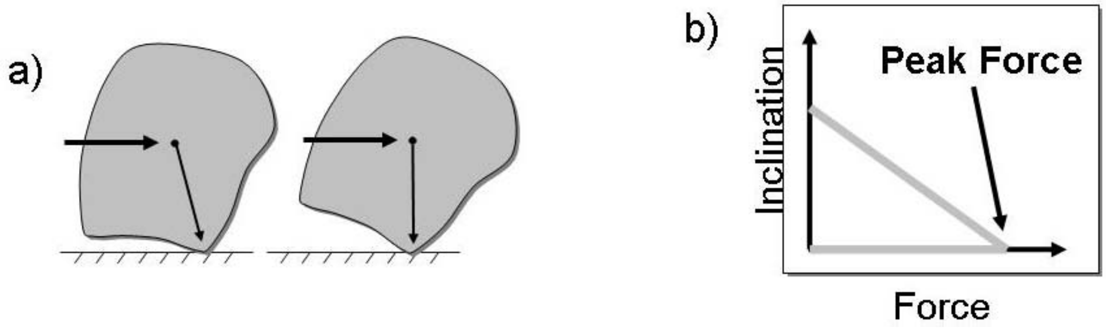

FIGURE 10: (a) Simple rocking model assumed in the numerical formulation of Purvance [9]. (b) Schematic of the restoring force versus angle of inclination.

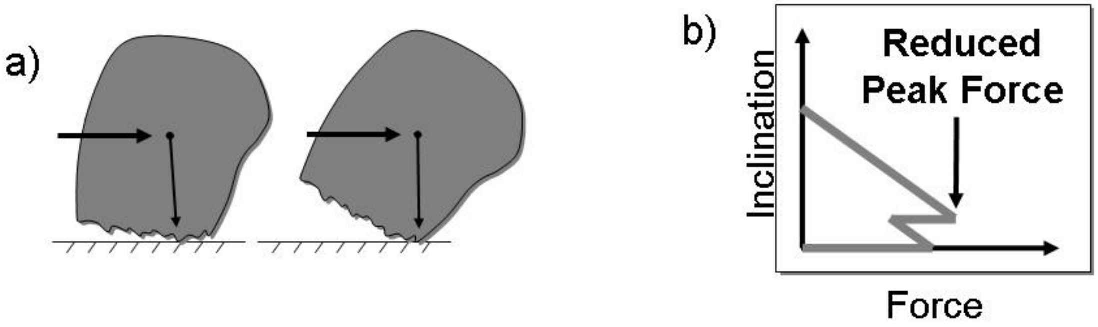

FIGURE 11: (a) Complex rocking model with multiple rocking points. (b) Schematic of the restoring force versus angle of inclination. The arctangent of the peak normalized force is utilized subsequently.

FIGURE 12: Tilt test of one of the stone boulders shaken experimentally.

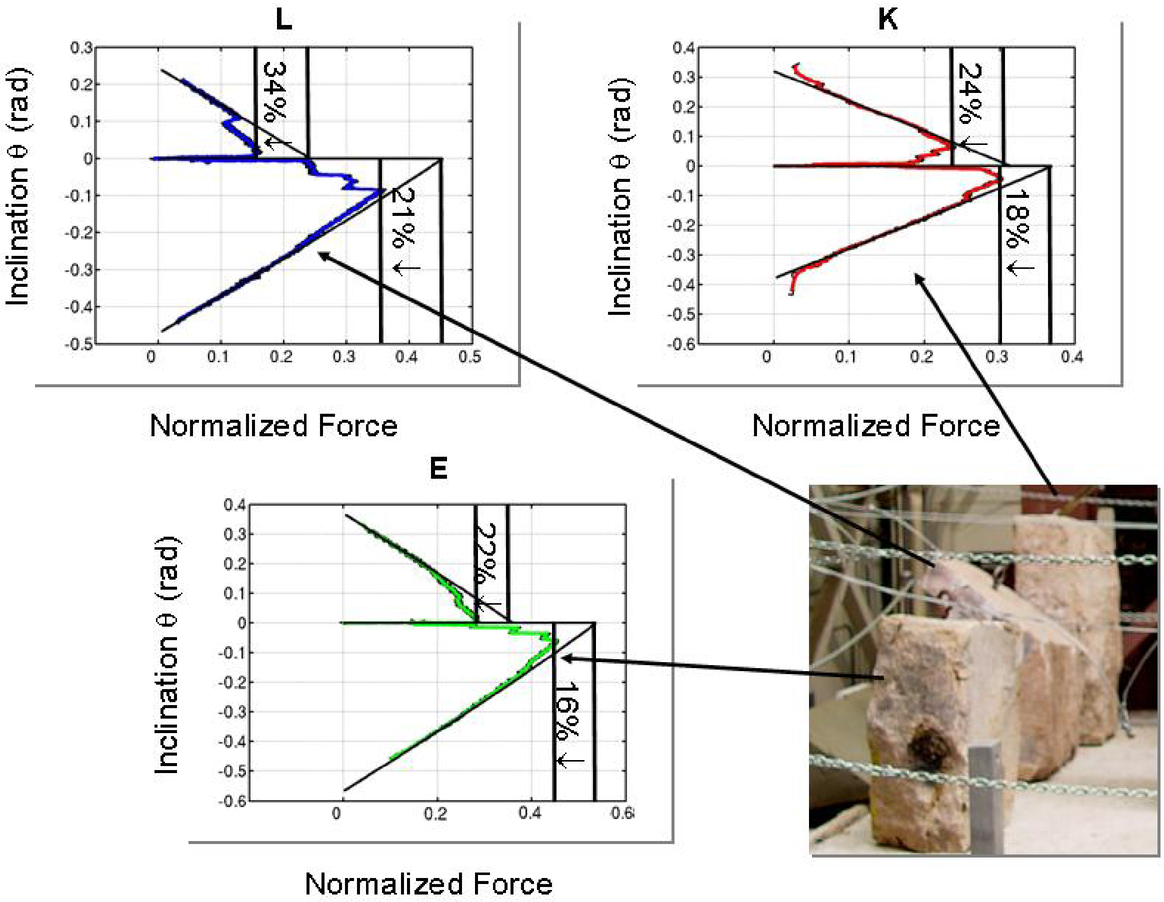

FIGURE 13: Force versus inclination measurements for boulders L, K, and E. The percentages on these figures represent the percent reduction in peak normalized force compared to a rock with a perfectly sharp edge (Source DTN: 020RA.001).

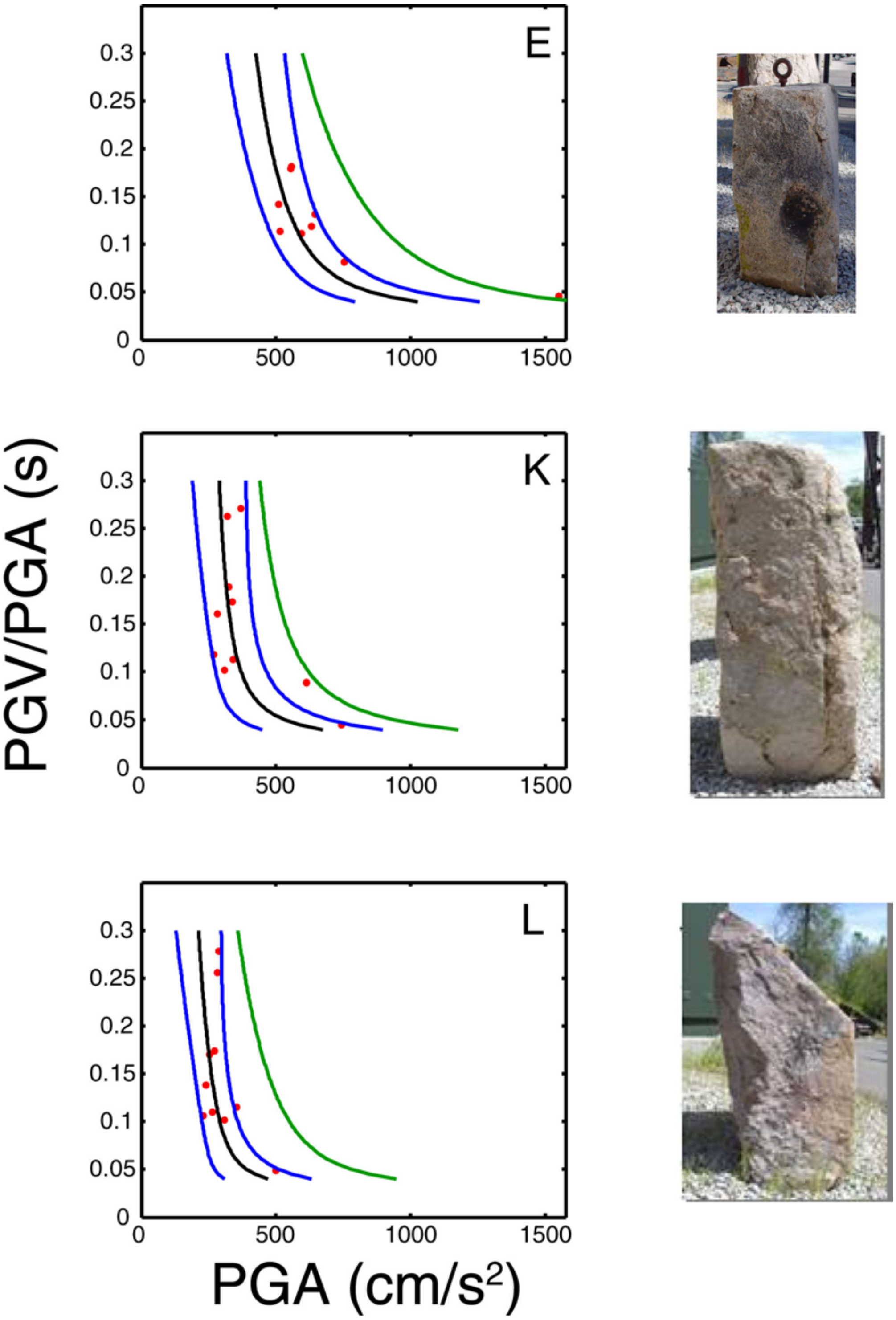

FIGURE 14: Refined overturning predictions based on force versus inclinations measurements and the formulation of Purvance [9] for the boulders L, K, and E. The red dots are from shake-table experiments. The green curves, identical to the black curves in Fig. 9, are plotted for comparison when the basal roughness is not taken into account. In these plots the curves are non-Q and included for corroboration only (DID 020RA.003, fig-14).

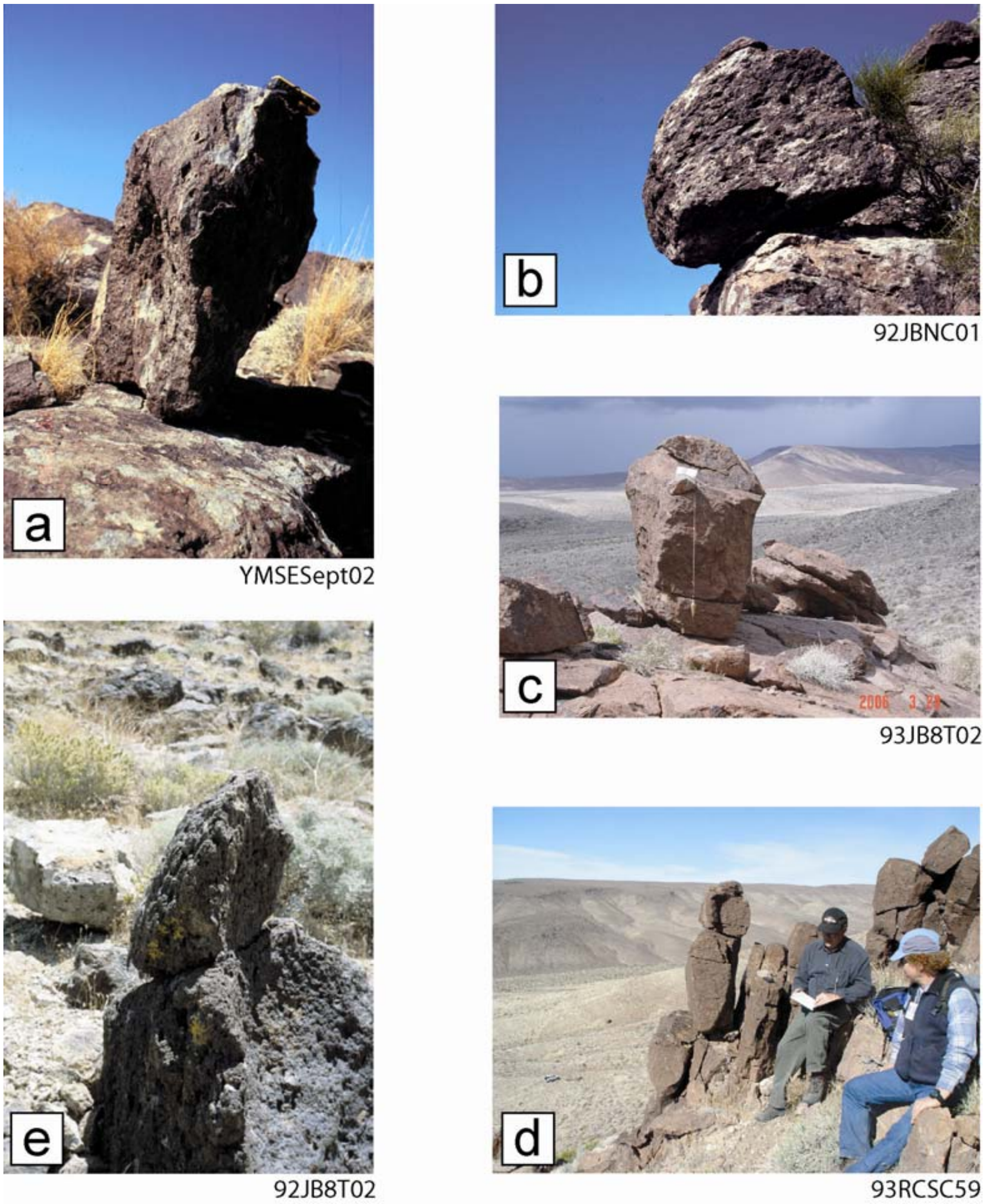

FIGURE 15. Photographs of the five precarious rocks in the Yucca Mountain Area selected for field test. Rocks **a** and **b** are on or near the Yucca Mountain crest. Rocks **c**, **d**, and **e** are on the west side of Yucca Mountain, in Solitario Canyon.

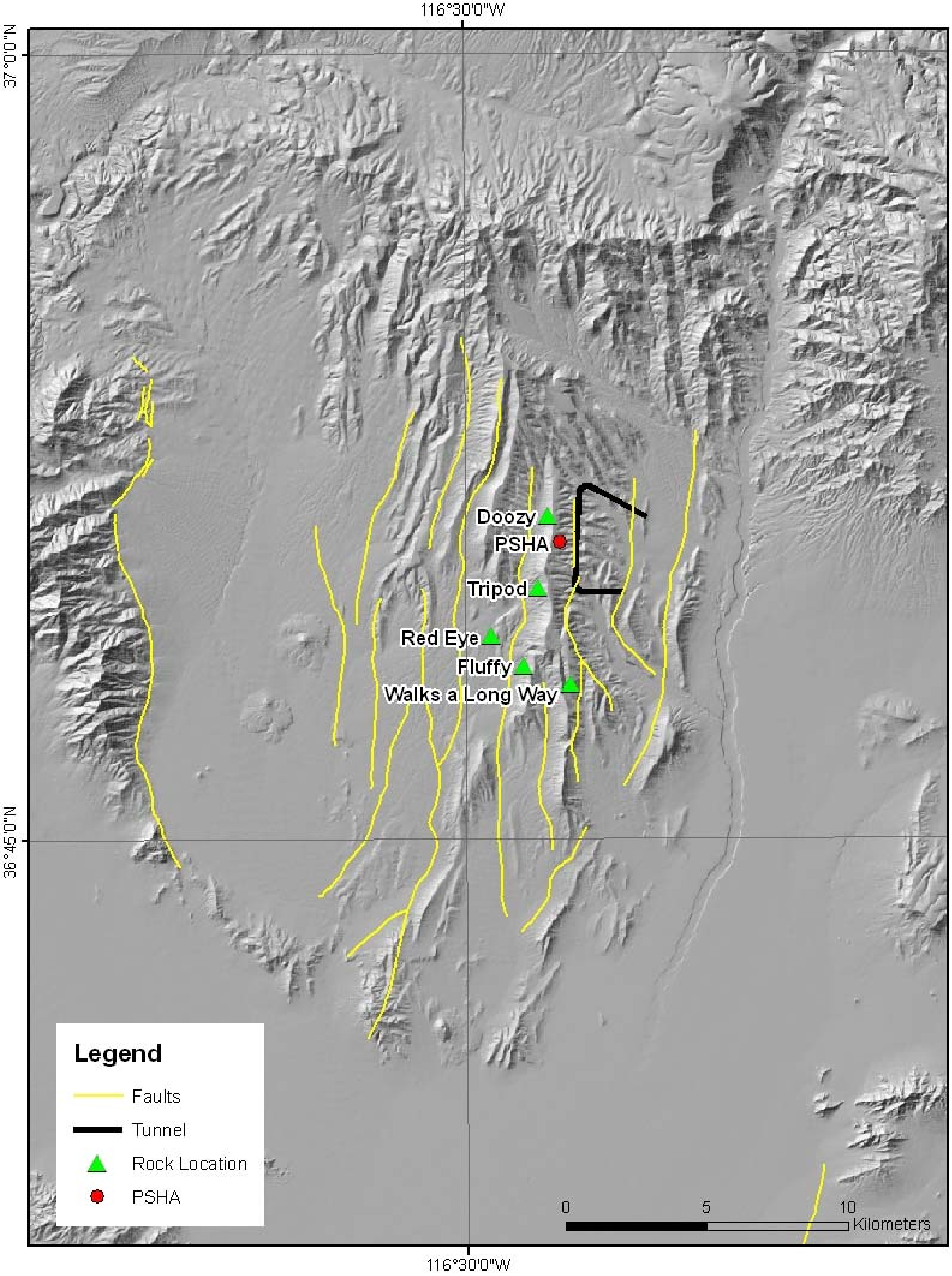

FIGURE 16. Locations of the five rocks shown in Fig. 15 are marked on the map.

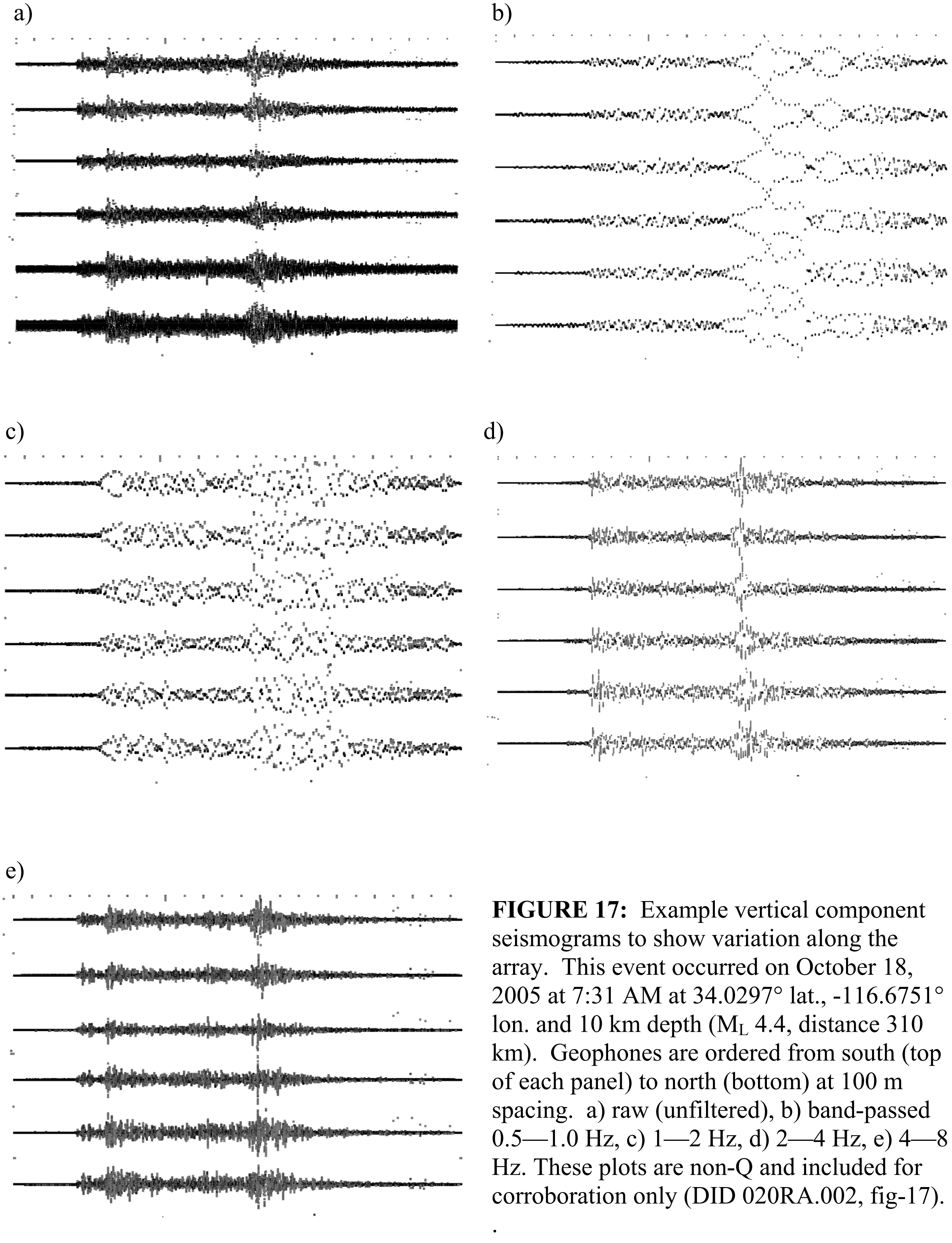

FIGURE 17: Example vertical component seismograms to show variation along the array. This event occurred on October 18, 2005 at 7:31 AM at 34.0297° lat., -116.6751° lon. and 10 km depth (M_L 4.4, distance 310 km). Geophones are ordered from south (top of each panel) to north (bottom) at 100 m spacing. a) raw (unfiltered), b) band-passed 0.5—1.0 Hz, c) 1—2 Hz, d) 2—4 Hz, e) 4—8 Hz. These plots are non-Q and included for corroboration only (DID 020RA.002, fig-17).

.

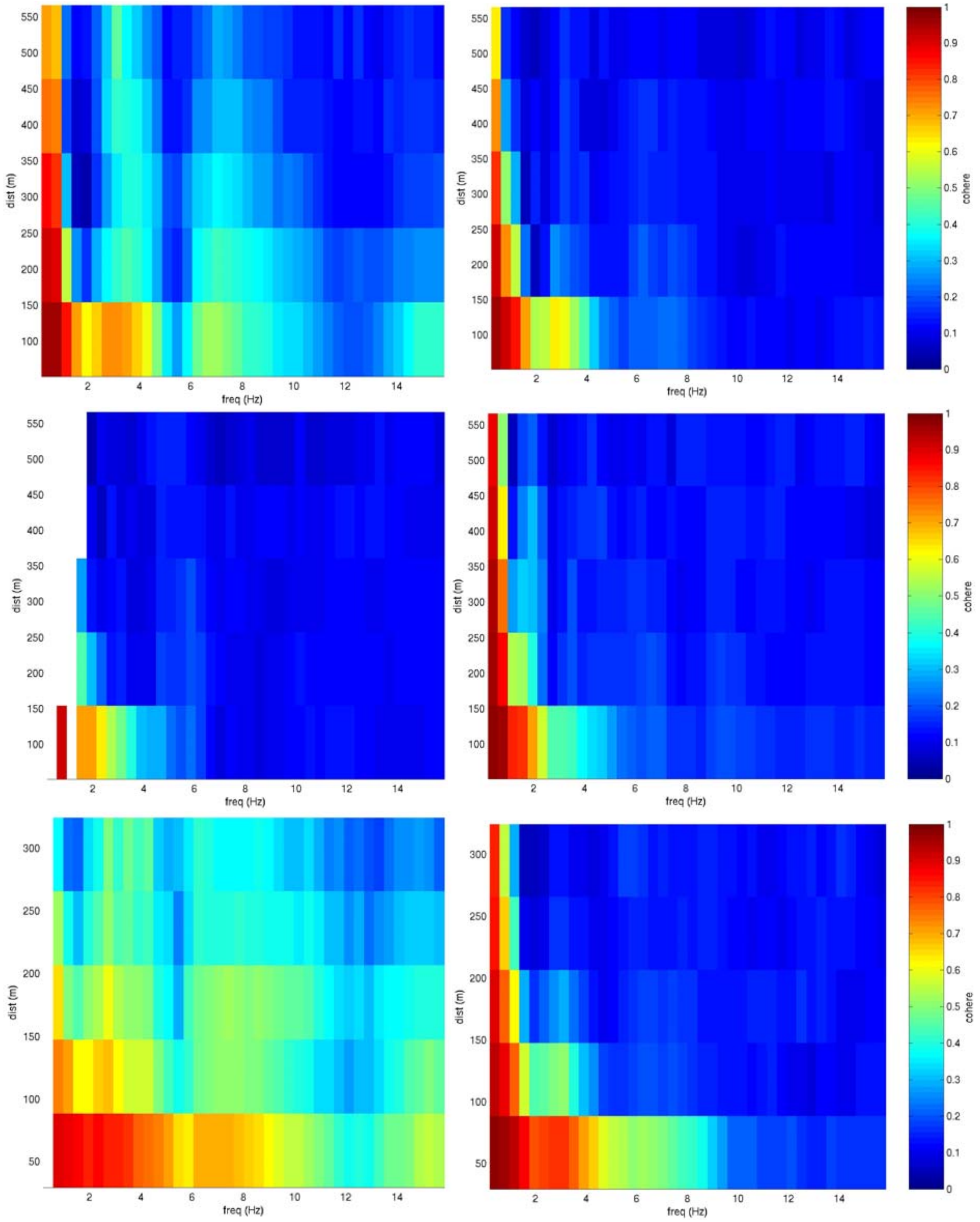

Figure 18: Coherency results as a function of inter-station distance and frequency. The top row is from the 100 m spacing, vertical phase of the study; the middle row is from the 100 m, horizontals; the bottom row from the 60 m, verticals. Left column is for P-wave; right is for S-waves. White areas represent areas with no data. These plots are non-Q and included for corroboration only (DID 020RA.002, fig-18).

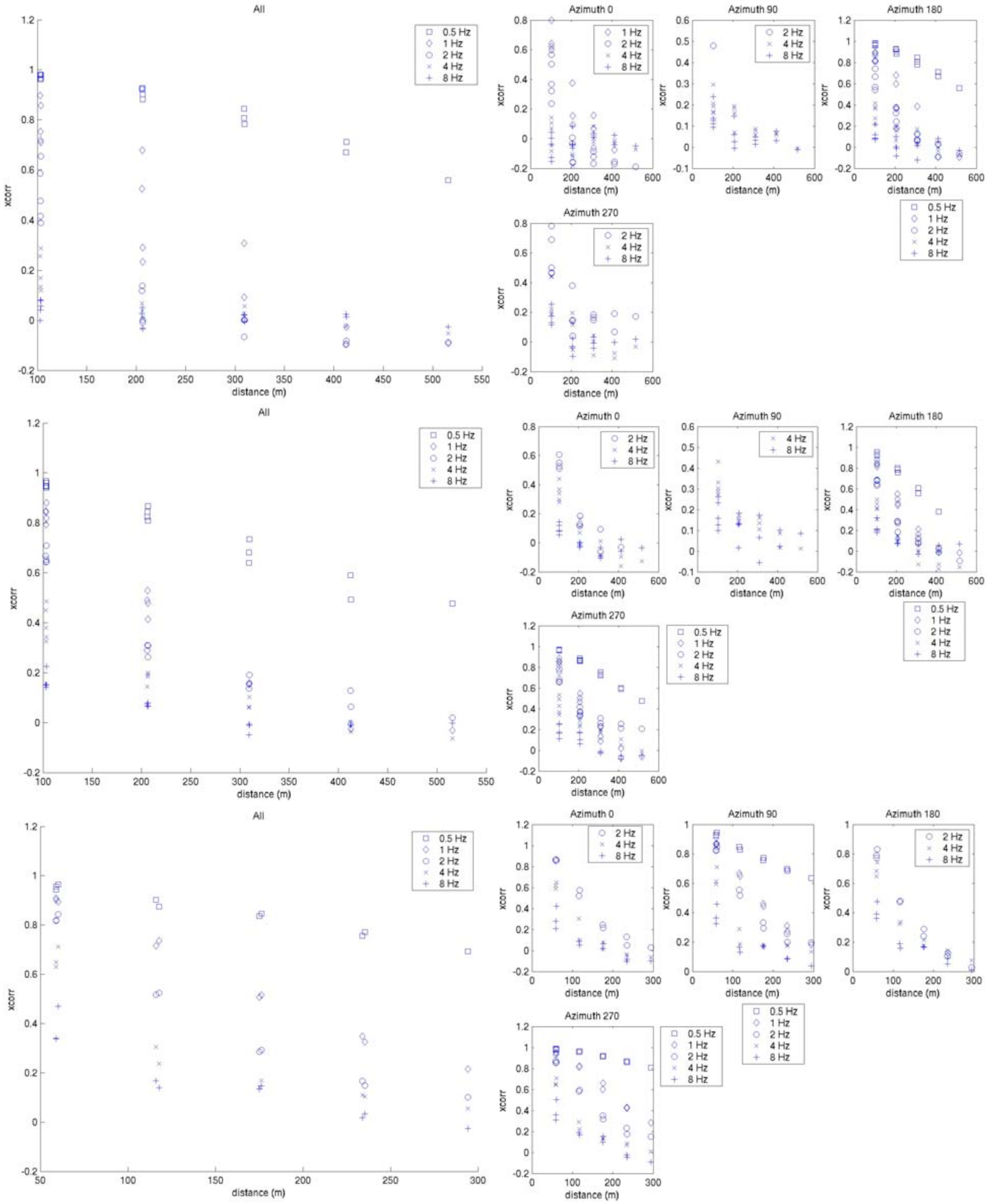

Figure 19: Cross-correlation results. The top row is from the 100 m spacing, vertical phase of the study; the middle row is from the 100 m, horizontals; the bottom row from the 60 m, verticals. Left column shows results for all the data in that phase for each receiver pair; right, is the same except divided into four azimuthal bins. These plots are non-Q and included for corroboration only (DID 020RA.002, fig-19).

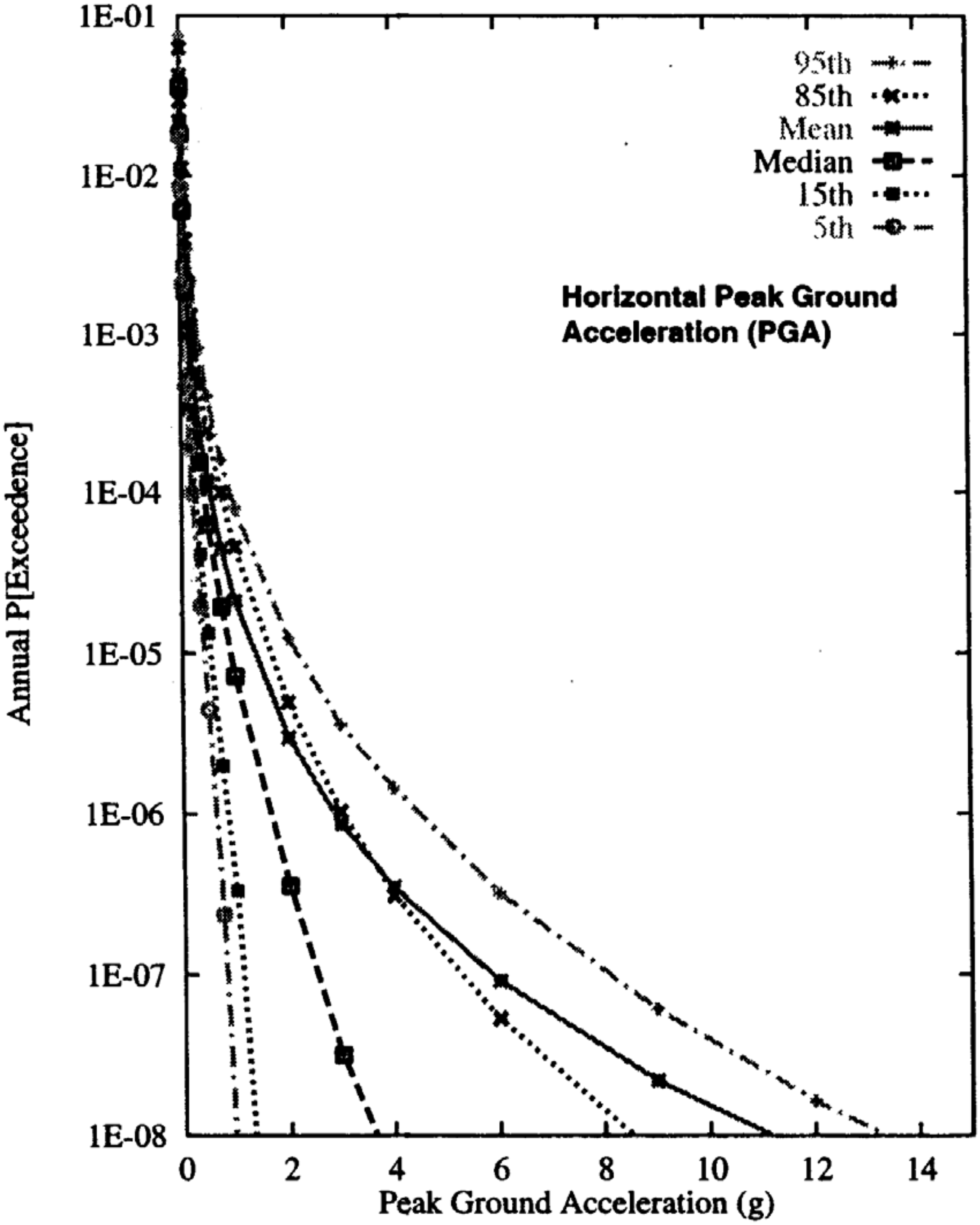

FIGURE 20: Annual probability of exceedance of the mean horizontal peak acceleration calculated from YM PSHA. This figure does not appear in the Stepp *et al* article [10], which was truncated at a higher probability. The probabilistic seismic hazard analysis used numerous "expert opinions" about the input, and calculated hazard curves for each. Ground motions exceeded by various percentiles of the resulting hazard curves are tabulated here. The mean gets higher than the 85^{th} percentile because the mean is taken as the average of annual probability rather than the average of the log of the annual probability. This plot is non-Q and included for corroboration only (Source Accession Number: MOL.19980619.0640).

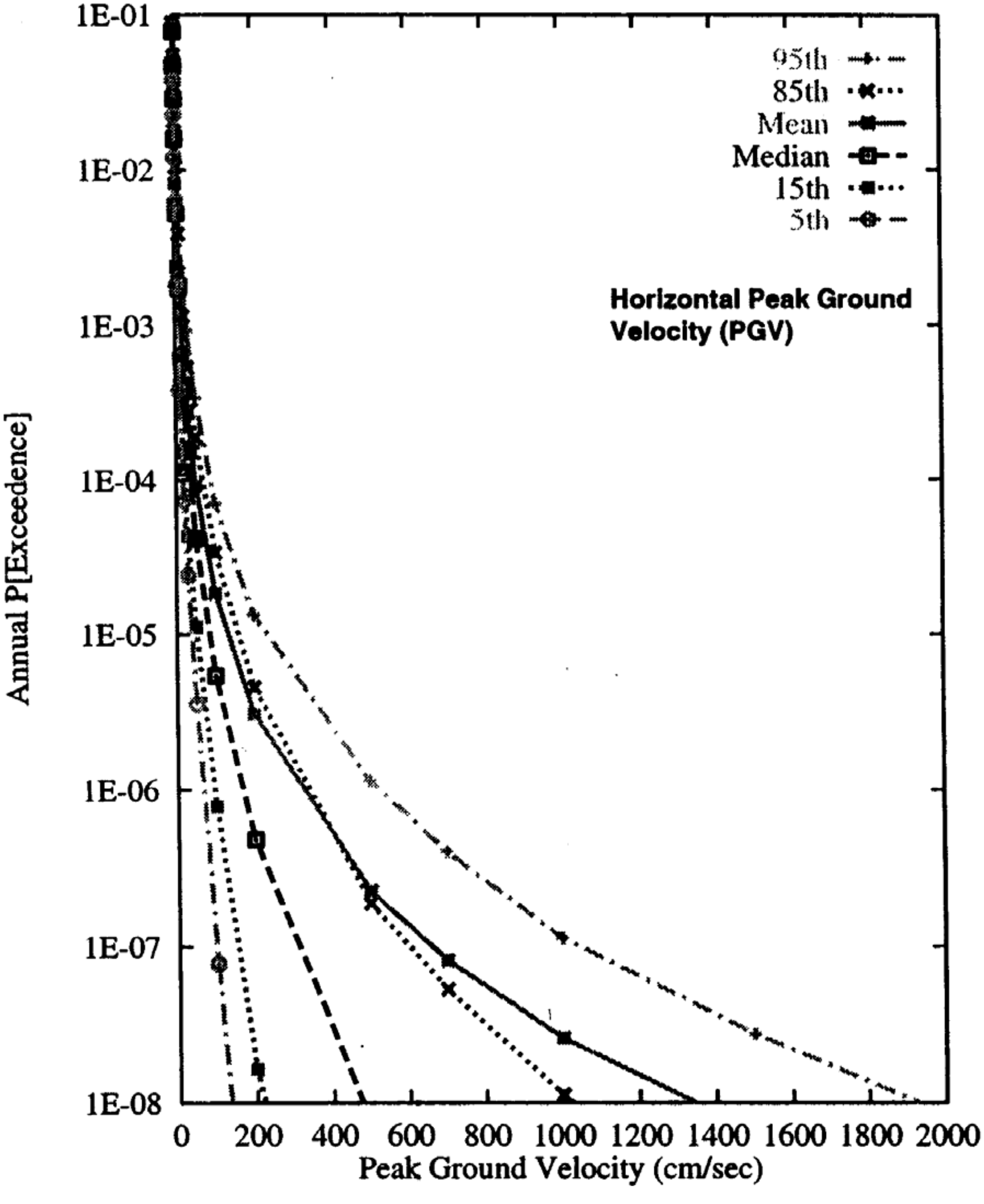

FIGURE 21: Equivalent of Fig. 20, except for the mean of the horizontal peak ground velocity. This plot is non-Q and included for corroboration only (Source Accession Number: MOL.19980619.0640).

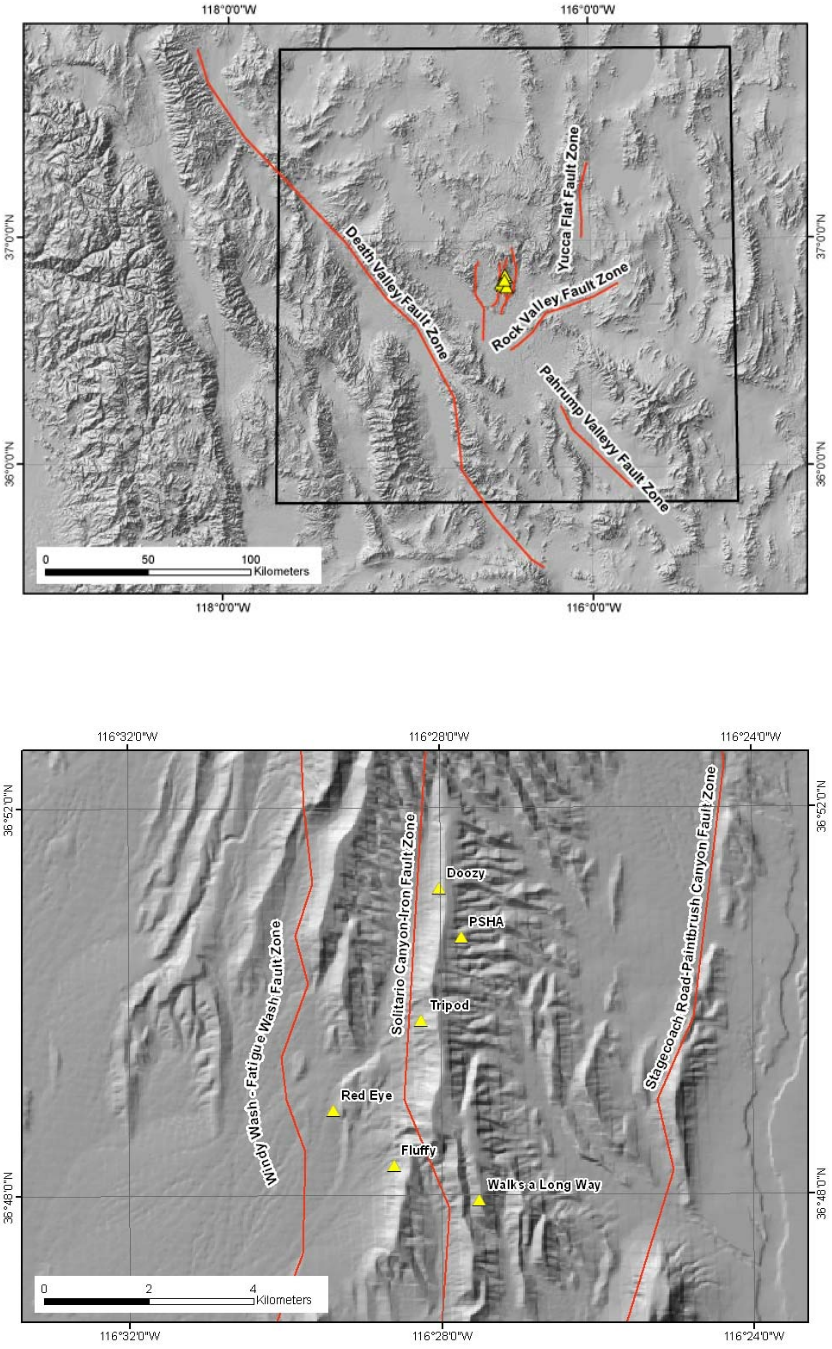

FIGURE 22: (top) Regional map showing the source model used for these calculations, and (bottom) detailed map showing the source model used for these calculations in the vicinity of the precarious rocks and the PSHA site.

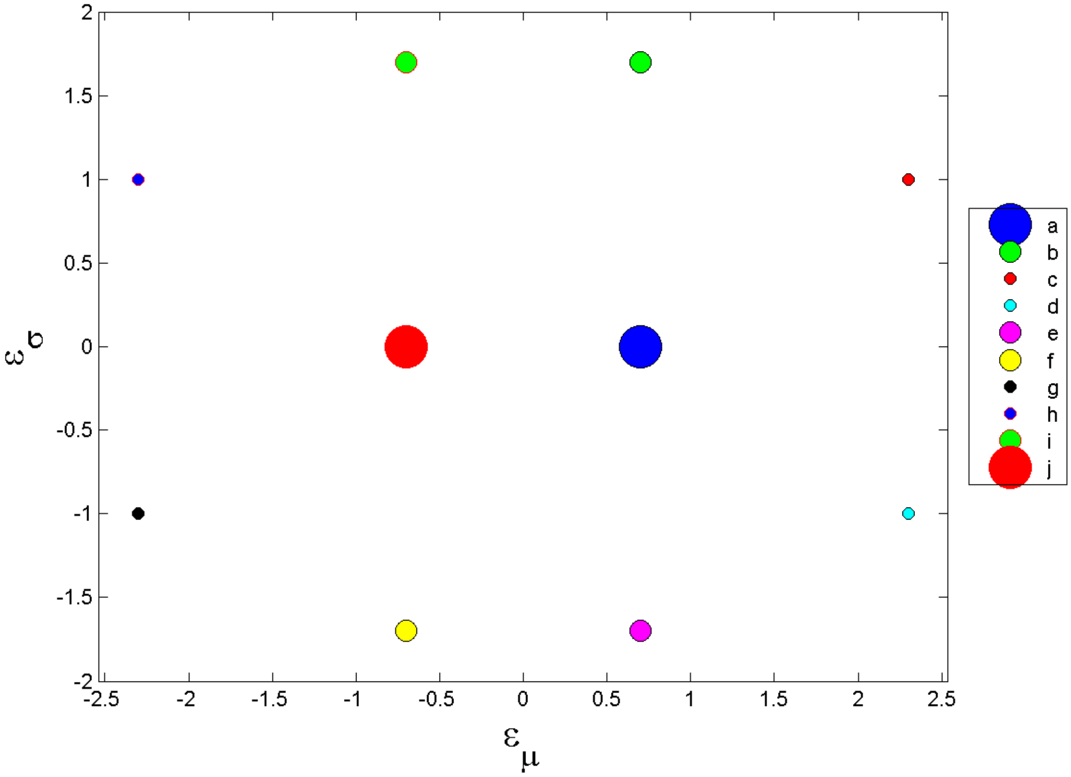

FIGURE 23: Plot showing values of ε_μ and ε_σ for approximating the effect of the epistemic uncertainty. This plot is non-Q and included for corroboration only (DID 020RA.004, fig-23).

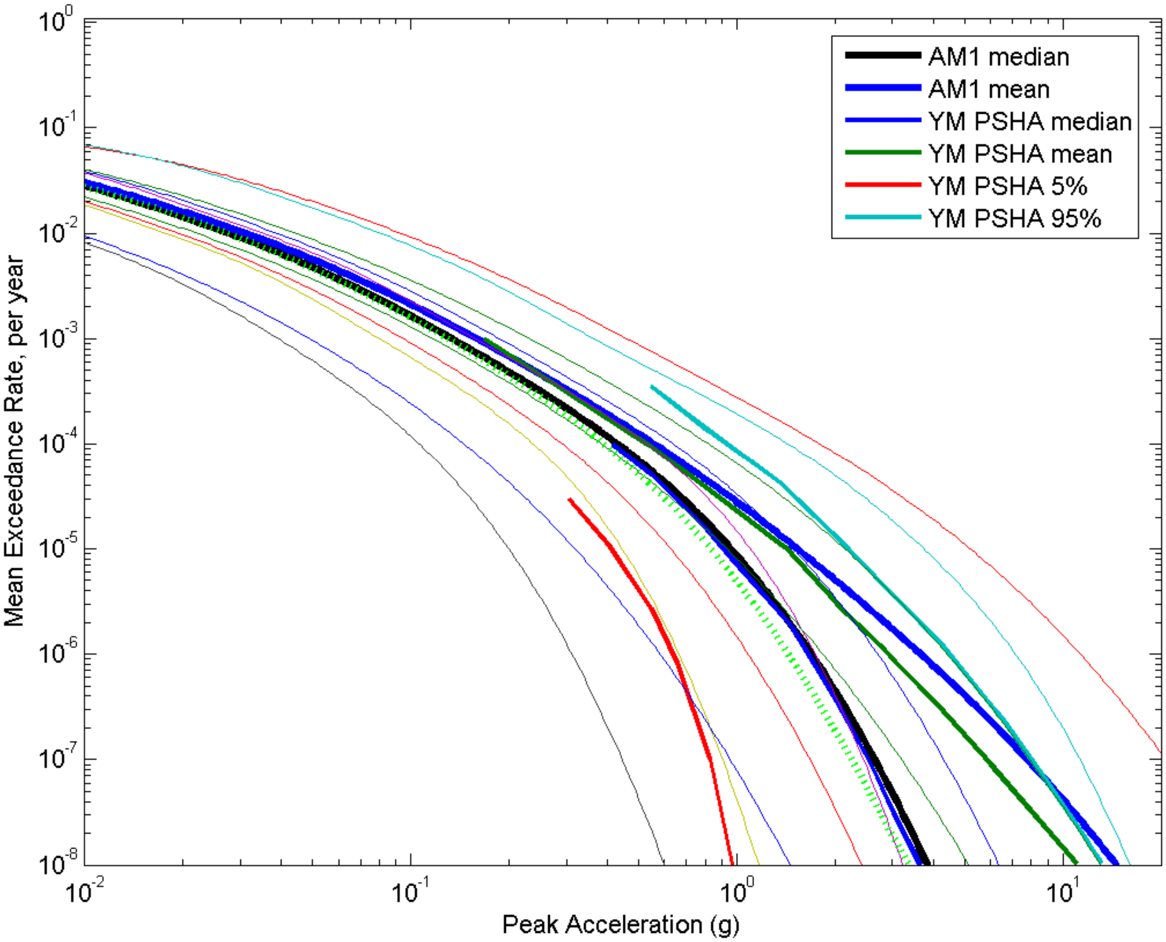

FIGURE 24: Combination of several hazard curves for peak acceleration. The lightest lines are hazard curves for the ten combinations of ε_μ and ε_σ. The colors of these lines match the marker colors in Fig. 23. The mean curve is the weighted mean of these ten curves, with weights given in Table 5; note that the mean is determined from the occurrence rates, and not the log of the occurrence rates, thus explaining why the mean deviates towards the highest curves. The median curve is the curve computed for $\varepsilon_\mu = 0$ and $\varepsilon_\sigma = 0$. The YMP median, mean, 5%, and 95% curves are from Fig. 20. This plot is non-Q and included for corroboration only (DID 020RA.004, fig-24).

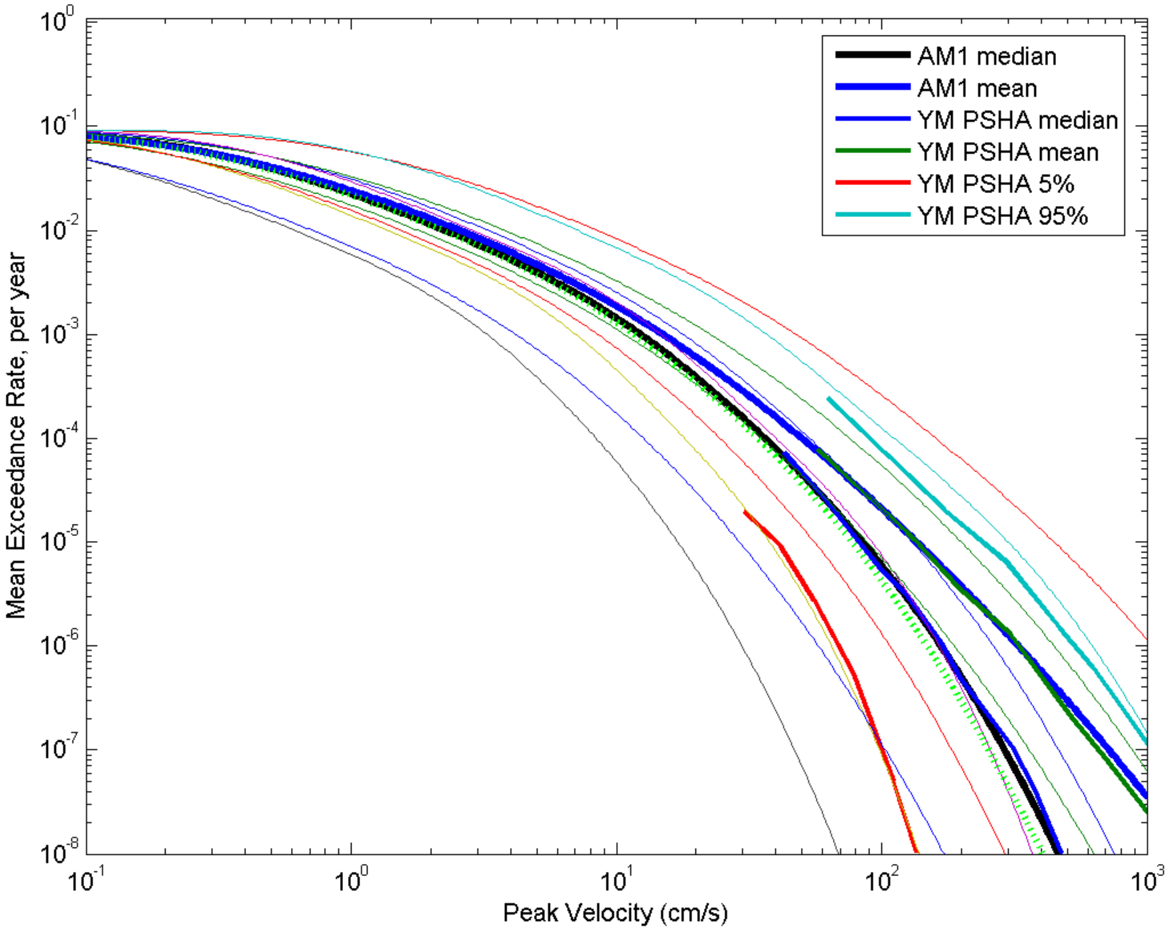

FIGURE 25: Equivalent of Fig. 24 for peak velocity. This plot is non-Q and included for corroboration only (DID 020RA.004, fig-25).

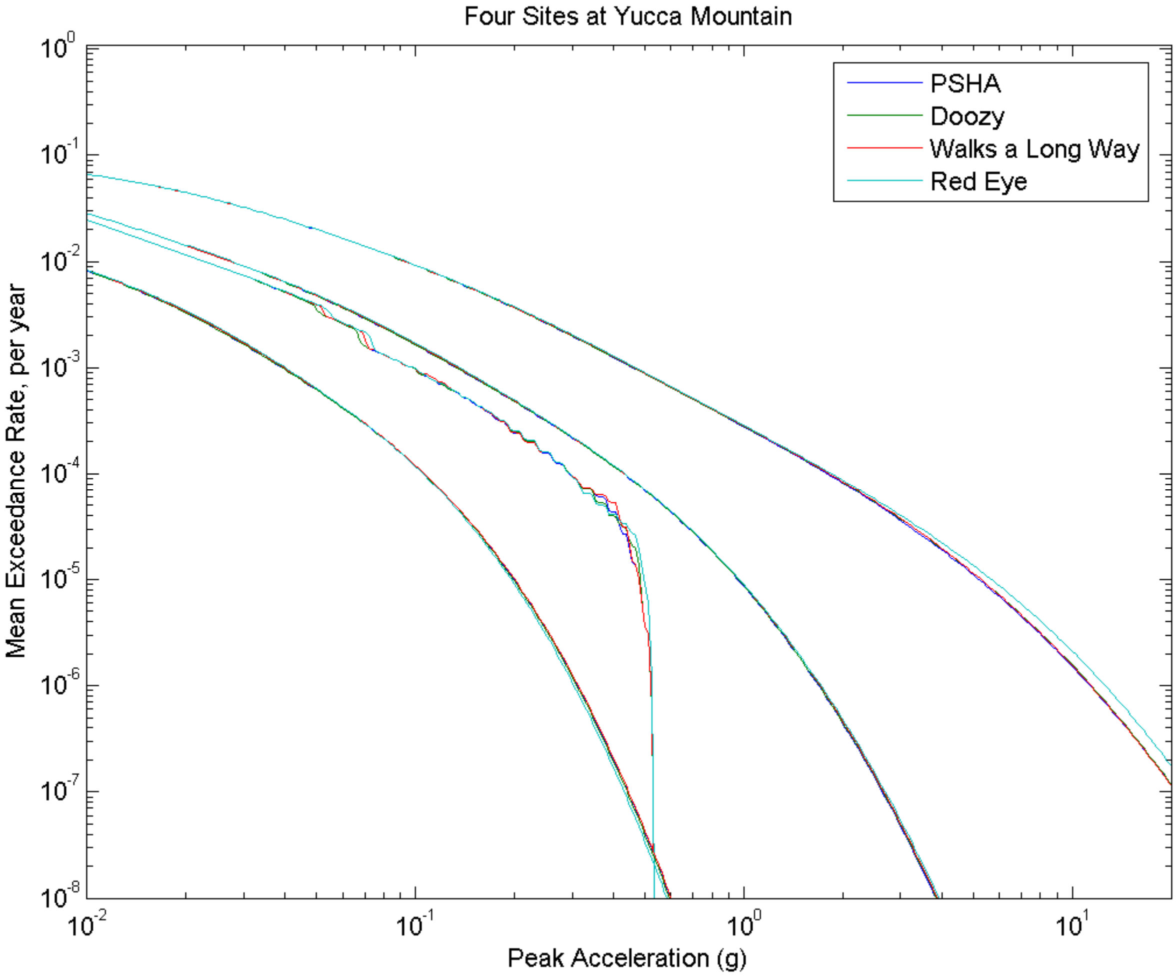

FIGURE 26: Comparison of selected hazard curves for peak acceleration at four sites. The curves are for the four cases, from largest to smallest occurrence rates: case c (defined in Table 5), the median model for the Anderson ground motion prediction equations, a model with $\sigma_A = 0.01$ instead of the value given in the ground-motion model, and case f (defined in Table 5). This plot is non-Q and included for corroboration only (DID 020RA.004, fig-26).

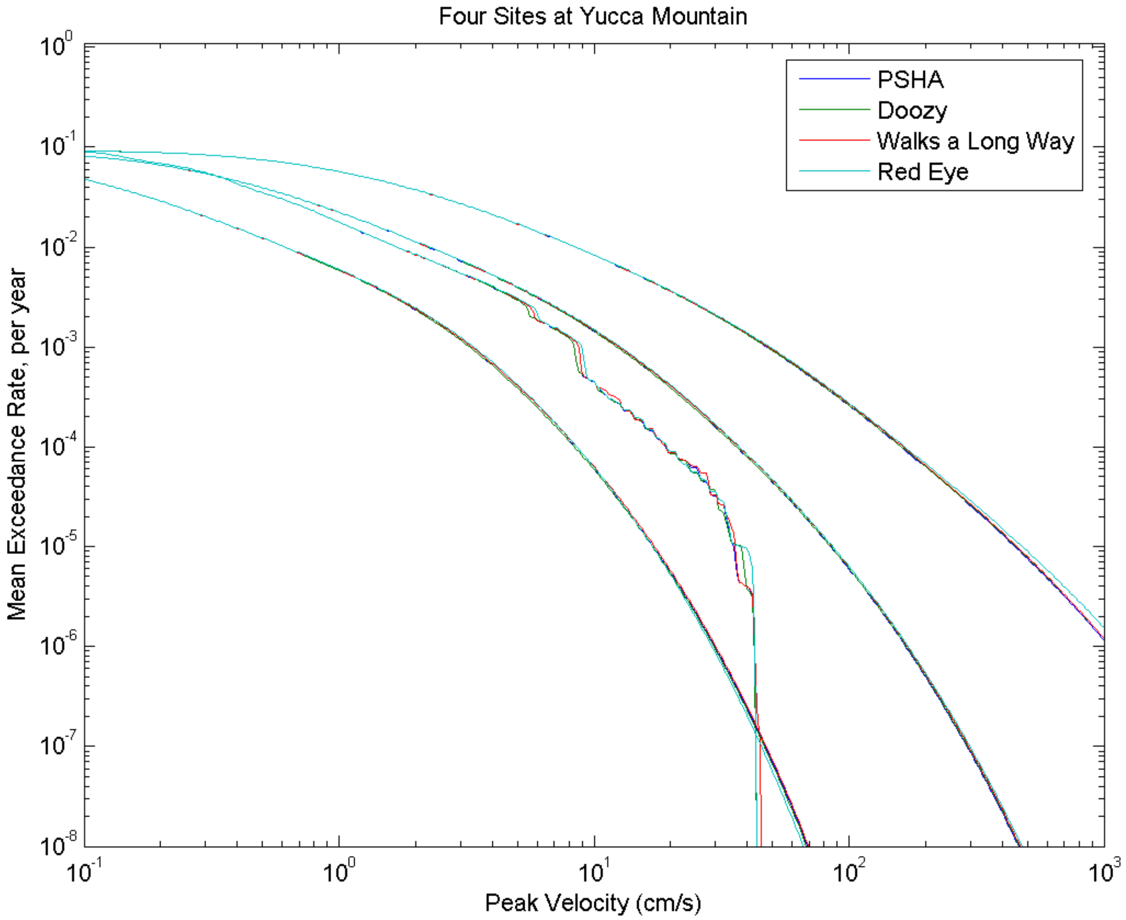

FIGURE 27: Comparison of selected hazard curves for peak velocity at four sites. See caption for Fig. 26 for description of the hazard curves. This plot is non-Q and included for corroboration only (DID 020RA.004, fig-27).

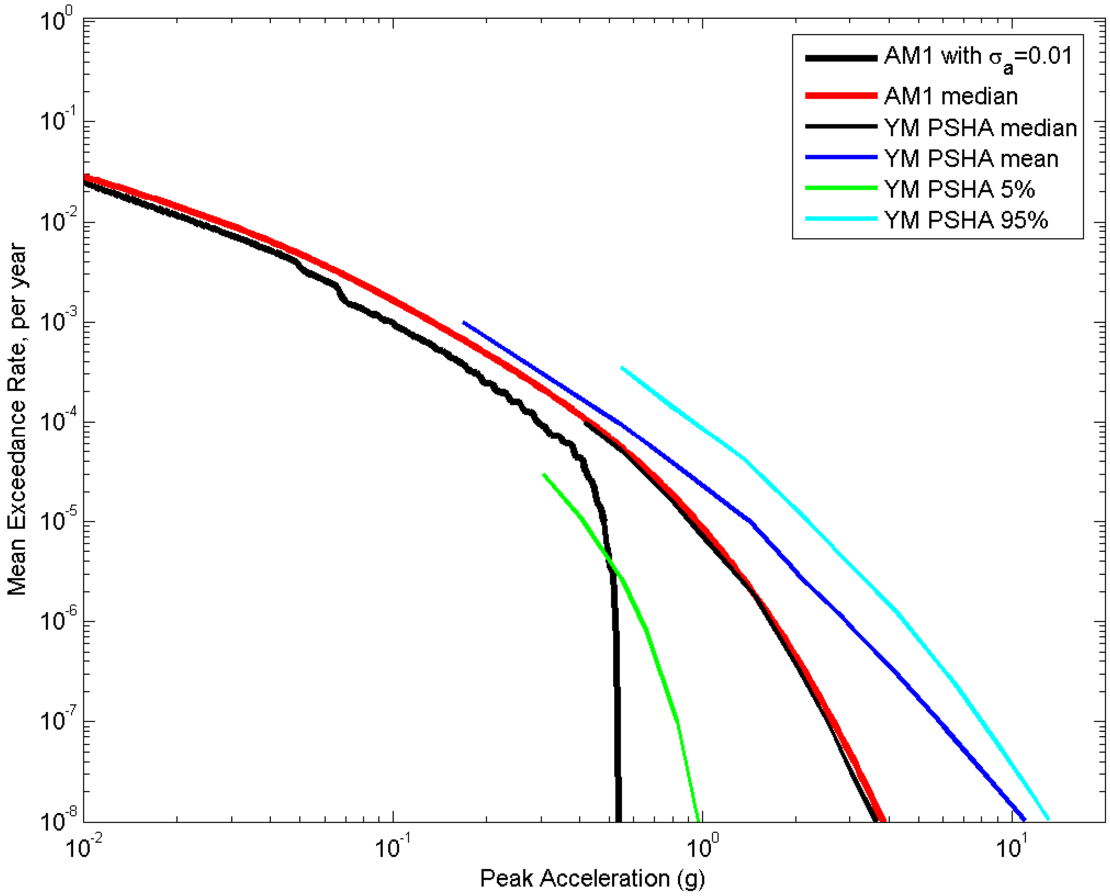

FIGURE 28: Peak acceleration results using $\sigma_A = 0.01$ compared with the YMP median and range of values and compared with the median curve for the JGA model. This plot is non-Q and included for corroboration only (DID 020RA.004, fig-28).

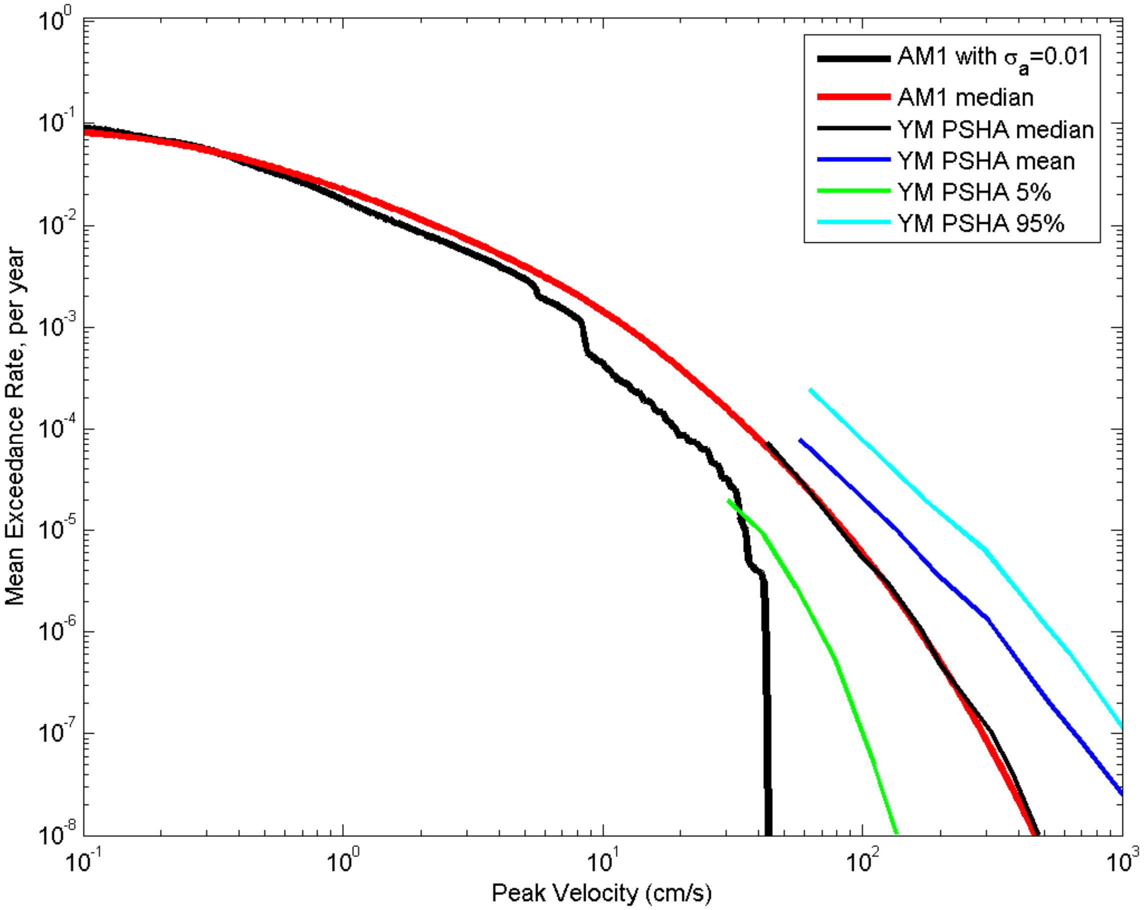

FIGURE 29: Equivalent of Fig. 28 for peak velocity. This plot is non-Q and included for corroboration only (DID 020RA.004, fig-29).

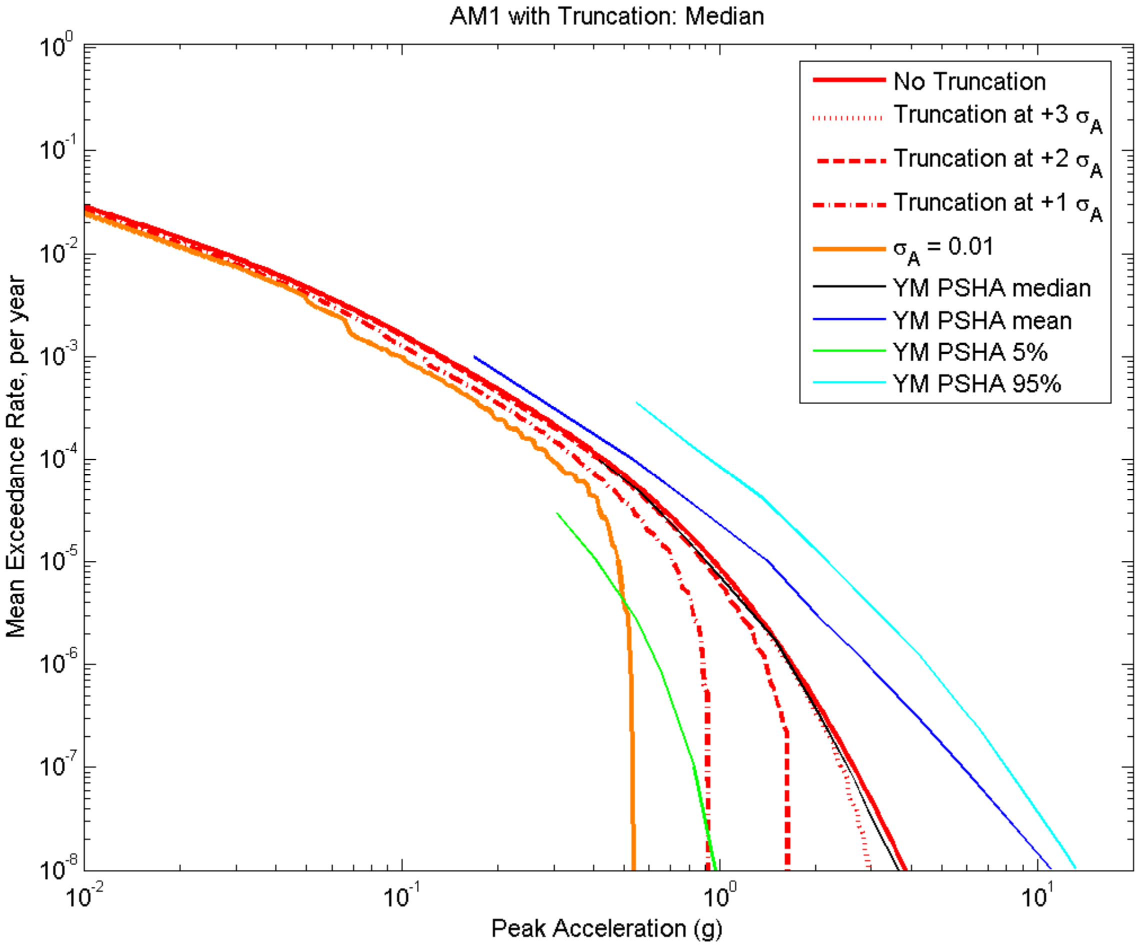

FIGURE 30: Equivalent to Fig. 28, but now also showing the effects of truncation of the distribution of ground motions at selected multiples of σ_A above the median value on the estimated mean exceedance rate of the peak acceleration. This plot is non-Q and included for corroboration only (DID 020RA.004, fig-30).

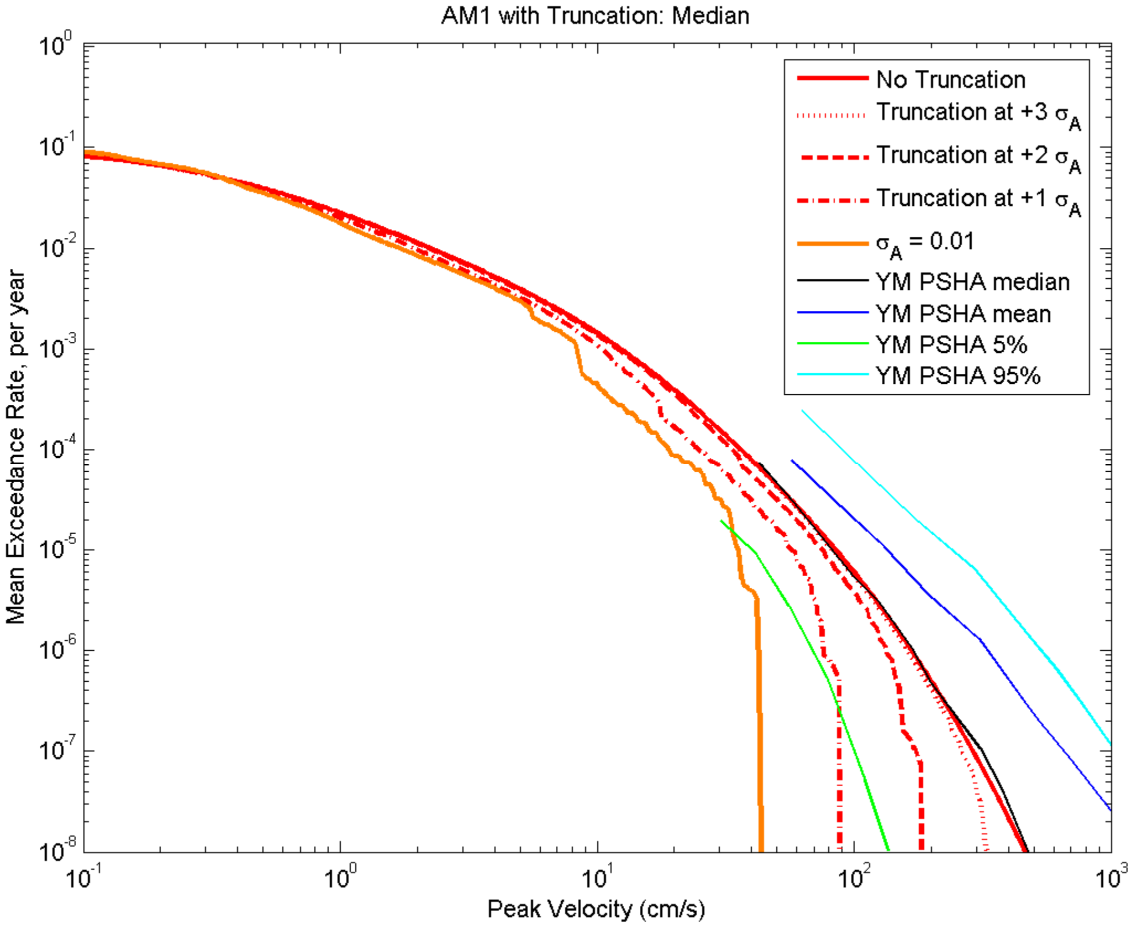

FIGURE 31: Equivalent to Fig. 29, but now also showing the effects of truncation of the distribution of ground motions at selected multiples of σ_A above the median value on the estimated mean exceedance rate of the peak acceleration. This plot is non-Q and included for corroboration only (DID 020RA.004, fig-31).

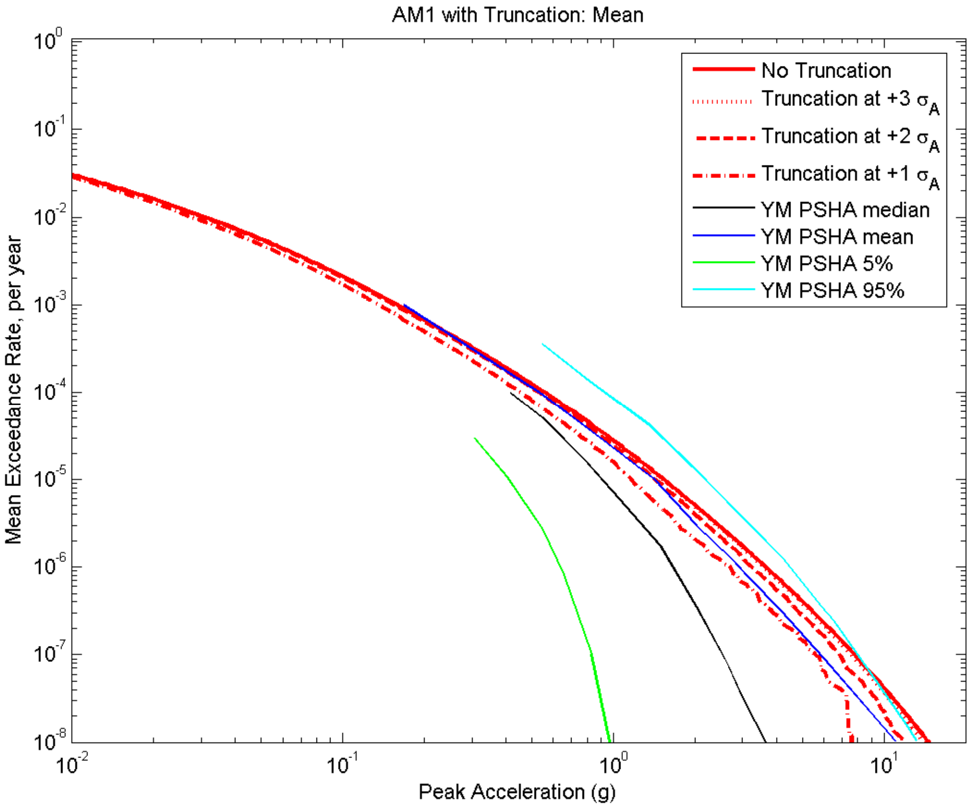

FIGURE 32: Examination of the impact of truncation of the distribution of ground motions at selected multiples of σ_A above the median value on the mean exceedance rate of peak acceleration. The mean curve is estimated by taking the mean of the ten hazard curves defined in Table 5. The case with no truncation is the same as the mean shown in Fig. 24. This plot is non-Q and included for corroboration only (DID 020RA.004, fig-32).

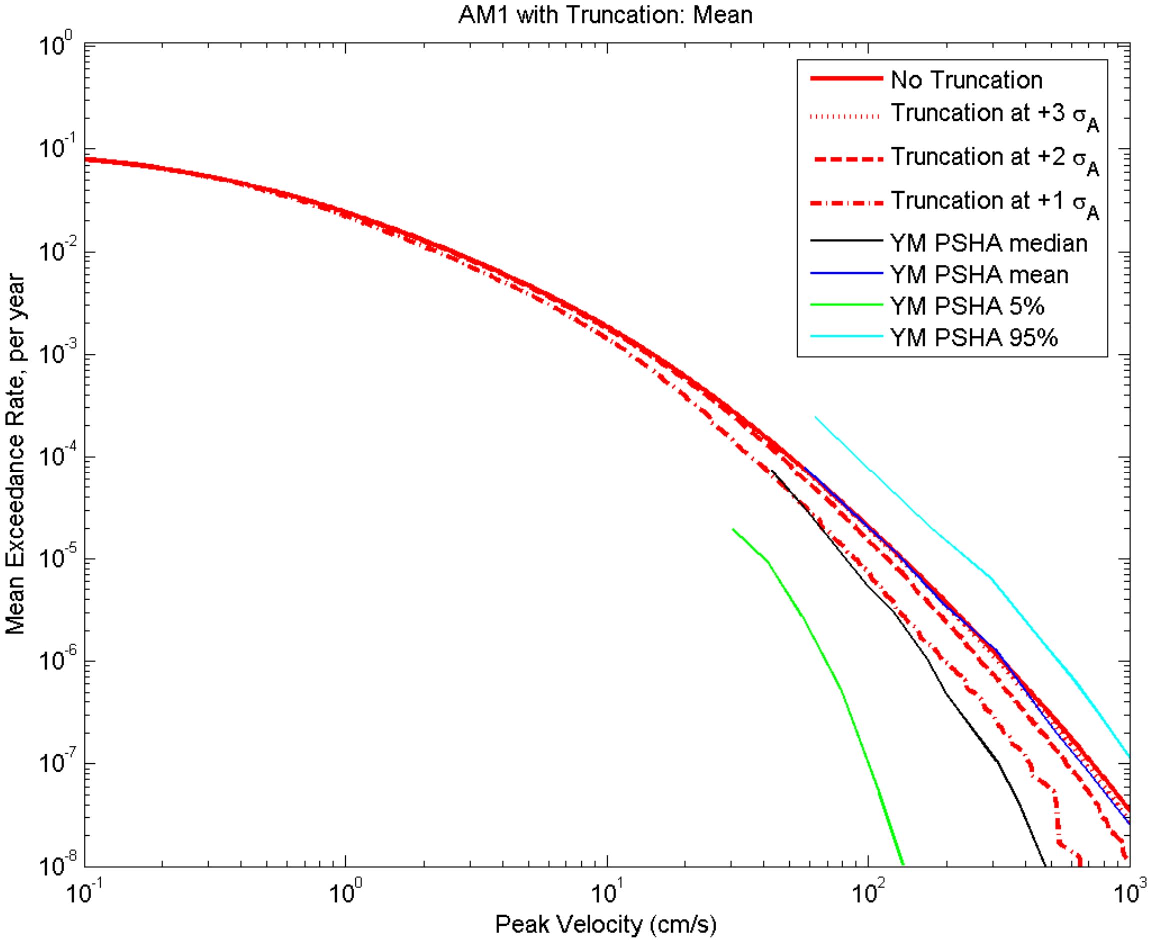

FIGURE 33: Examination of the impact of truncation of the distribution of ground motions at selected multiples of σ_A above the median value on the mean exceedance rate of peak velocity. The mean curve is estimated by taking the mean of the ten hazard curves defined in Table 5. The case with no truncation is the same as the mean shown in Fig. 25. This plot is non-Q and included for corroboration only (DID 020RA.004, fig-33).

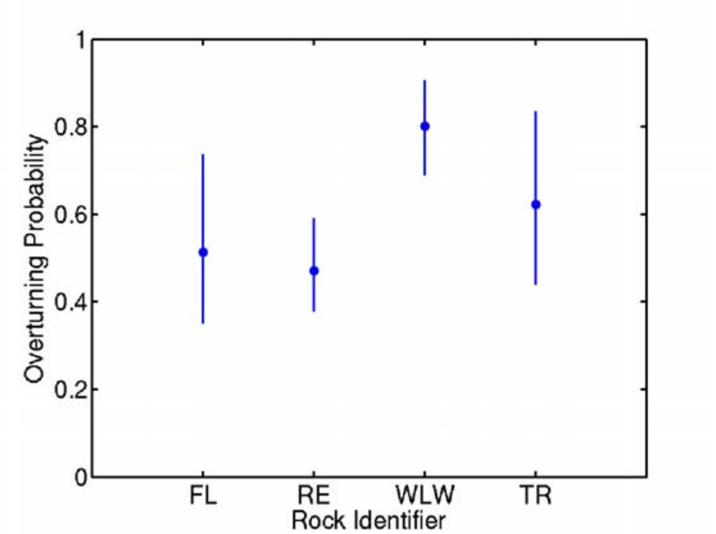

FIGURE 34: Overturning probability of the precarious rocks Fluffy (FL), Red Eye (RE), Walks a Long Way (WLW), and Tripod (TR) exposed to the median ground motion model (*e.g.*, ε_μ and $\varepsilon_\sigma = 0$). The error bars correspond to the 5% and 95% prediction intervals on the overturning probability. These rocks are not consistent with the median ground motion model (*e.g.*, ε_μ and $\varepsilon_\sigma = 0$) as discussed in the text. This plot is non-Q and included for corroboration only (DID 020RA.004, fig-34).

.

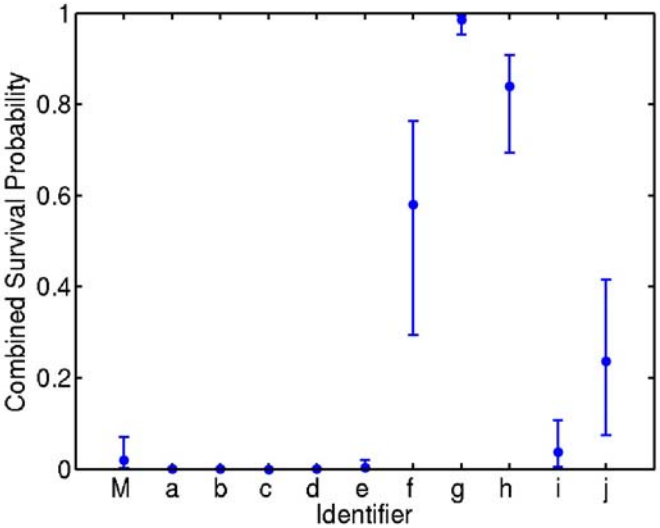

FIGURE 35: Combined survival probability of the ensemble of 4 precarious rocks (*e.g.*, probability that all 4 rocks simultaneously survive the ground motion model) along with the combined survival probabilities corresponding to the 5% and 95% prediction intervals of the overturning model. The identifier M corresponds to the median ground motion model (ε_μ and $\varepsilon_\sigma = 0$) and the identifiers a - j correspond to the cases ($\varepsilon_\mu, \varepsilon_\sigma$) equal to (0.7,0), (0.7,1.7), (2.3,1.0), (2.3,-1.0), (0.7,-1.7), (-0.7,-1.7), (-2.3,-1.0), (-2.3,1.0), (-0.7,1.7), and (-0.7,1.0), respectively. This plot is non-Q and included for corroboration only (DID 020RA.004, fig-35).

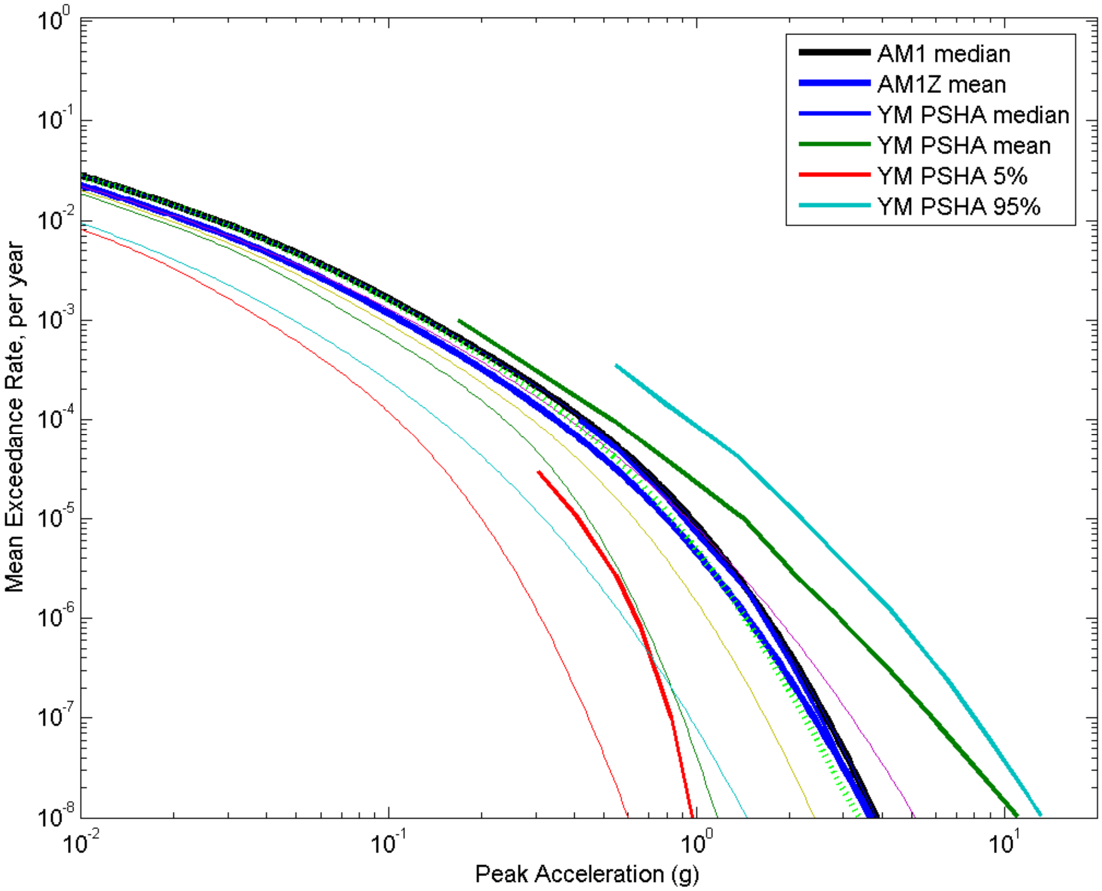

FIGURE 36: Peak acceleration, for the case where only non-positive values of ε_μ are considered, as discussed in the text. This plot is non-Q and included for corroboration only (DID 020RA.004, fig-36).

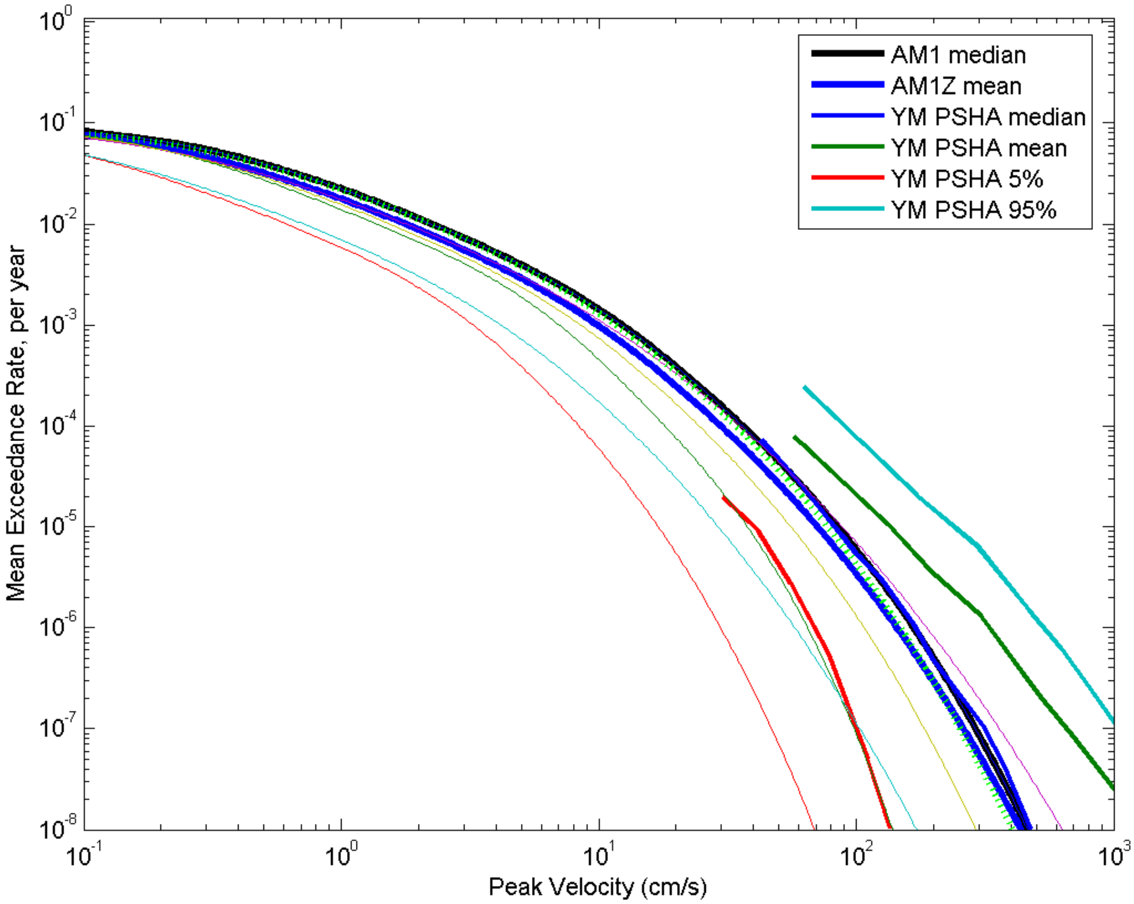

FIGURE 37: Peak velocity, equivalent of Fig. 36. This plot is non-Q and included for corroboration only (DID 020RA.004, fig-37).